Smart organic-inorganic nanohybrids

of functionalized

silsesquioxane nanoparticles

Dissertation

zur Erlangung des akademischen Grades
eines Doktors der Naturwissenschaften (Dr. rer. nat.)
in der Fakultät für Biologie, Chemie und Geowissenschaften
der Universität Bayreuth

vorgelegt von
Manuela Schumacher (geb. Fink)
aus Eichstätt

Bayreuth, November 2008

Zwei Dinge sind zu unserer Arbeit nötig:
Unermüdliche Ausdauer und die Bereitschaft,
etwas, in das man viel Zeit und Arbeit gesteckt hat,
wieder wegzuwerfen.
(Albert Einstein)

für meine Familie…

Die vorliegende Arbeit wurde
in der Zeit von Juli 2004 bis November 2008
in Bayreuth am Lehrstuhl Makromolekulare Chemie II
unter der Betreuung von Herrn Prof. Dr. Axel H. E. Müller angefertigt.

Vollständiger Abdruck der von der Fakultät für Biologie / Chemie / Geowissenschaften der Universität Bayreuth genehmigten Dissertation zur Erlangung des Grades eines Doktors der Naturwissenschaften (Dr. rer. nat.).

Dissertation eingereicht am: 25. November 2008

Zulassung durch die Promotionskommission: 03. Dezember 2008

Wissenschaftliches Kolloquium: 12. März 2009

Amtierender Dekan: Prof. Dr. Axel H. E. Müller

Prüfungsausschuss:

Prof. Dr. Axel H. E. Müller (Erstgutachter)

Prof. Dr. Thomas Hellweg (Zweitgutachter)

Prof. Dr. Karlheinz Seifert

Prof. Dr. Josef Breu (Vorsitz)

Contents

1 Introduction

1.1 Polymer architectures and structures

The synthesis of polymers via controlled radical polymerization techniques offers the possibility to design them with various architectures; examples are linear polymers, brush-like ones or star-like polymers. Structural differences yield to drastic effects on the solution behaviour of polymers. Copolymers offer even more chances to form different architectures and attract due to that great interest. Block copolymers can be synthesized as sequential linear polymers of the AB, ABA or also ABC type with A, B and C as different monomers and can be considered as homogenous polymer fragments (blocks) joined together by covalent bonds. Furthermore, statistical copolymers with randomly inserted monomers exist as well as gradient copolymers, which are built up from an almost homopolymer (A) with an increasing content of the inserted second monomer (B). Another class of block copolymers are grafted ones. Figure 1.1 shows an overview of selected polymer architectures.[1-11]

homopolymer

copolymer

terpolymer

block copolymer

statistical copolymer

alternating copolymer

grafted copolymer
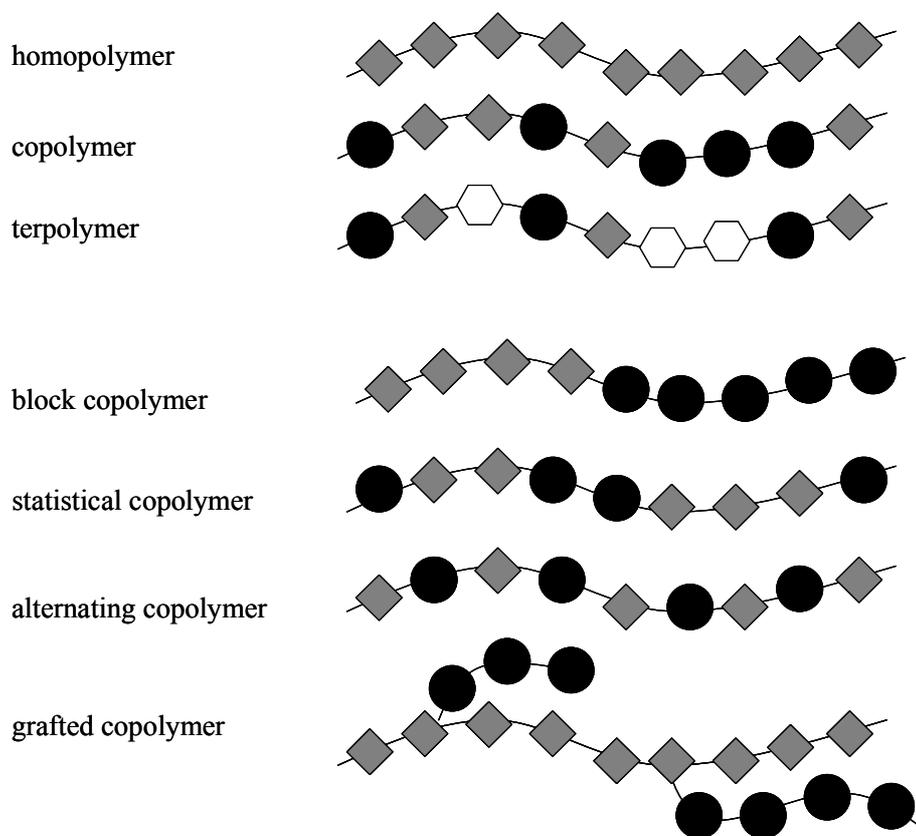
Figure 1.1. Overview of selected polymer architectures.

1.2 Block copolymers

Block copolymers can be alternatively also designed as brush-like block copolymers, star-like ones or as miktoarm stars being composed of the linkage of different block copolymers at one branching point. Additionally, block copolymers with immiscible blocks offer the chance to self-organise in bulk and solution (Figure 1.2).[8,10,12-14] The phase behaviour of such diblock copolymers has been subject of numerous theoretical and experimental studies over recent decades, and is relatively well understood. This self-assembly process is driven by an unfavourable mixing enthalpy and a small mixing entropy, while the blocks connecting covalent bond prevents macroscopic phase separation. The microphase separation of diblock copolymers depends on the total degree of polymerization of both blocks (N), the Flory-Huggins χ-parameter measuring the incompatibility between the two blocks and the volume fraction of the constituent blocks. The segregation product $\chi \cdot N$ determines the degree of microphase separation leading to three different segregation regimes. This are the weak segregation limit for $\chi \cdot N \leq 10$, the intermediate segregation limit for $10 < \chi \cdot N \leq 50$ and the strong segregation limit for $\chi \cdot N \to \infty$.[10,15-18]

In bulk, the minority block is segregated from the majority block forming regularly-shaped and uniformly-spaced nanodomains. The shape of the segregated domains in a diblock is governed by the volume fraction of the minority block fraction and block incompatibility.[10,18,19]
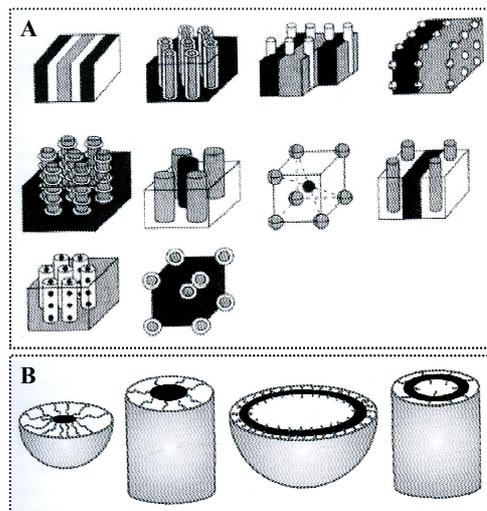
Figure 1.2. Schematic representations of morphologies obtained for ABC triblock terpolymers in bulk (A). B shows cross-sectional views of chain packing in diblock copolymer spherical, cylindrical, vesicular and tubular micelles (from left to right).[10]

In analogy to their bulk behaviour, diblock copolymers are able to self-assemble in selective solvents, meaning solvents which can solubilise one but not the other block. Investigations on self-assembly of block copolymers in selective solvents started with the observations of the formation of a large variety of morphologies of block copolymers by A. Eisenberg around 1995. Star-like, crew-cut, and rod-like micelles as well as vesicles are the most important species (Figure 1.2B). Apart from the nature of the blocks and the solvent, the block length and the block ratio has dramatic effect on the structure of the block copolymer assemblies in solution. If the soluble block is predominant, the insoluble block aggregates to produce spherical micelles. Decreasing the length of the soluble block in relation to the insoluble block, cylindrical micelles (rods) or vesicles are formed. The structure of a given diblock copolymer can sometimes be influenced via usage of a increasingly poor solvent for the insoluble block to form unusual micelles with shapes differing from spheres.[10,20-26]

The major contributions to the thermodynamically favoured self-aggregation of block copolymer micelles are: first the interfacial energy of the core-shell interface, second the energy needed to stretch the block copolymer chains, third the incompatibility of the core building material with the solvent (surface energy) and fourth the hydrophobic interaction between the core forming block.[27-29] Stimuli-responsive polymeric micelles are to some extent comparable to low molecular weight micelles although they are less responsive to external stimuli like pH, ionic strength, temperature or the addition of a chemical agent.[30,31]

In the case of polymeric micelles it generally has to be divided between so called frozen micelles, kinetically frozen - also called kinetically hindered micelles - and dynamic micelles.[29,31] Dynamic micelles are of great interest especially if their water-insoluble block (e.g. polyisobutylene (PIB)[32,33]) has a sufficiently low enough glass transition temperature (T_g) enabling them to form spontaneously micelles at room temperature without the need of any kind of cosolvent. This is required in the case of the polystyrene-*b*-polyelectrolyte systems mainly investigated by A. Eisenberg et al.,[20-23,34,35] which form frozen micelles in pure water. Additionally, dynamic micelles offer the possibility to change their aggregation number, N_{agg}, and thus the size of the core upon external stimuli.[10,27-29,36]

Further research on block copolymer chemistry focussed on water solubility, self-assembly, stimuli responsiveness, building of organic and inorganic blocks as well as the understanding of the driving forces to form specific morphologies. Block copolymers offer a huge variety of potential applications as there are drug delivery, diagnostics, nanocapsules, membranes, catalysis, chemical separation and electronics to mention.[10] Controlled structur-

ing on the nano-scale dimension is the main driving force for the extended investigations on block copolymers as thereby the formation of specific structures is enabled.

The investigations in this work are focussed on linear amphiphilic block copolymers and on amphiphilic star homopolymers in aqueous solution.

1.2.1 Amphiphilic ionic block copolymers

A very important class of block copolymers are amphiphilic diblock copolymers which are of great interest in various research fields.[36] This is due to the existence of a large variety of different monomers for synthesis of the individual blocks allowing the composition of materials with tailored properties like responsiveness to changes in pH, temperature or ionic strength. Of special interest are block copolymers containing ionic hydrophilic and hydrophobic blocks. As already mentioned, they are of huge interest for researchers as they are able to self-assemble in water, leading to the formation of well-defined aggregates like star-like micelles, crew-cut micelles, rods or vesicles (Figure 1.2B).{Rodríguez-Hernández, 2005 #62; Gil, 2004 #61; Förster, 2004 #55; Zhang, 1995 #63; Hales, 2006 #71; Riess, 2003 #70; Garnier, 2003 #72; Lazzari, 2006 #60} In particular, when the ionic block is a weak polyelectrolyte the size and shape of the aggregate may depend on pH and salinity. Ionic amphiphilic block copolymers are of great interest due to a large variety of potential applications in industry (e.g. emulsifing agents, surface modifiers, catalyst supporters, lubricants for oil drilling), ecology, biology, pharmaceutics and medicine (e.g. drug delivery).{Förster, 2004 #55; Hales, 2006 #71; Garnier, 2003 #72; Riess, 2003 #70; Hofs, 2008 #116; Lindhoud, 2007 #117}

It is frequently reported that weak polyelectrolytes like poly(acrylic acid) (PAA), poly(methacrylic acid) (PMAA) or poly(N,N-dimethylaminoethyl methacrylate) (PDMAEMA) can react with changes in structure and solubility on changes in pH, salinity or on addition of multivalent counterions.[10,20-24,27,29,34,36-41] A deeper insight in polyelectrolyte systems and their behaviour in aqueous solution follows below (page 8ff.).

Amphiphilic block copolymers possess the ability to be dissolved in water as is already indicated by their nomenclature. According to their physical and chemical behaviour they can be compared to low molecular surfactants which are built up by a hydrophobic, aliphatic chain and a hydrophilic head group. In low molecular surfactant chemistry the most widely used ionic surfactants are anionic sodium dodecylsulfate (SDS) and cationic cetyl-trimethyl ammonium bromide (CTAB). Nevertheless, also non-ionic surfactants exist, e.g. ethylenegly-

col based esters like propylene glycol monostearate or sugar based surfactants. Another class of low molecular surfactants are build up from zwitterionic molecules.

In block copolymer chemistry comparable structures can be synthesized leading to polyanionic blocks, polycationic ones or also neutral blocks of the block copolymer. Uncharged block copolymers are mostly based on ethylene oxide (PEO), especially Pluronics® (PEO-*b*-PPO-*b*-PEO) are due to their importance for industrial applications (e.g. defoaming during sugar production, usage as lubricants in metal industry)[42] to mention. Basic research (e.g. phase behaviour in oil-water-mixtures[43], carrier for gold nanoparticles[44]) focuses on them due to their easy availability.

Charged block copolymers possess also a hydrophobic block and a polyelectrolyte block as the ionic part. They combine the properties of electrolytes and surfactants with the structure of block copolymers. They are able to react on external stimuli like changes of the pH, ionic strength or temperature offering different possibilities to influence single parameters to control the physico-chemical properties of their aqueous solutions.

1.2.2 *Poly(*n-*butyl acrylate)*-block-*poly(acrylic acid) block copolymers*

Within the framework of our investigations the aqueous behaviour of poly(*n*-butyl acrylate)-*block*-poly(acrylic acid) (P*n*BA-*b*-PAA) micelles is of interest, which is still discussed contradictory in literature. Colombani et al.[45,46] reported about the synthesis of P*n*BA$_x$-*b*-PAA$_y$ (x = 90, 100 and y = 100, 150, 300 as the degree of polymerization) block copolymers by atom transfer radical polymerization (ATRP) (Figure 2.1). Those amphiphilic block copolymers were used for this work (Figure 2.5). According to fluorescence correlation spectroscopy (FCS) measurements a critical micelle concentration (cmc) existed showing the dynamic character of the spontaneously formed micelles with monomodal size distribution. The detected changes of the P*n*BA-*b*-PAA micellar systems upon pH and salinity changes were not significant. This and the observed dependence of the aggregates on the preparation method led to the conclusion that the micelles are kinetically frozen.

Eghbali et al.[47] used this system to show that no surface activity exists and that the surface tension at ionization degree (α) of roughly 0.1 is not lowered. This is in agreement with non dynamic micelles as they can not exclude unimers to reduce the surface tension. Above α ≈ 0.1 and at high concentrations the solutions showed an abrupt transition in the surface activity. This could be explained by the surface activity of the whole micelles themselves comparable to the well-known pickering effect.

Claverie et al.[48] reported about the synthesis of PnBA-b-PAA block copolymers by the reversible addition-fragmentation chain transfer polymerization (RAFT) and concluded that due to the low T_g (-55 °C) of PnBA these micelles can not be frozen. According to their dynamic light scattering (DLS) experiments the hydrodynamic radius (R_h) was constant in the pH range from 6.75 to 9. Furthermore, a change in salinity had no or just very little effect on R_h. According to their size exclusion chromatography (SEC) experiments, showing independent species of the unimer and of the micelle, they concluded that their micelles are kinetically frozen as the unimer-micelle exchange seemed to be very slow.

Laschewsky at al.[49,50] showed by a series of block copolymers with PnBA as the hydrophobic block and a number of hydrophilic blocks that the formed micelles were not frozen, as aggregates with defined size are formed upon direct dissolution of the block copolymer in water. Nevertheless, in addition to the formed micelles their DLS results showed larger aggregates which mostly dissolved within three month. This confirmed that unimer expulsion of the aggregates occurred. Nevertheless, this is in good agreement that micelles with PnBA core form rather kinetically frozen micelles than real thermodynamical dynamic micelles. Furthermore, they confirmed that the preparation history of the formation of the micelles was one of the controlling factors for the aggregation behaviour. This should have no effect for real - in thermodynamical aspects - dynamic micelles. Nevertheless, they showed mixing experiments of micelles with PnBA cores with different aggregate sizes which formed within three days aggregates with monomodal size distribution. They concluded that unimer exchange occurred and the micelles had to be dynamic therefore. Furthermore, they showed that those micelles had a low surface activity at the air/water surface. According to them this was also the reason for the absence of any foam formation for the ionic block copolymers. Nevertheless, real dynamic micelles should show surface activity. So this points again more to the direction of the formation of kinetically frozen micelles.

Jacquin et al.[51-53] described the synthesis of PnBA-b-PAA block copolymers with the macromolecular design via inter-exchange of xanthate (MADIX) polymerization process, a RAFT polymerization process using xanthates as control agents. They concluded that this system is not in thermodynamic equilibrium as the topology depended on the preparation method, as the micellar aggregation number did not depend on the concentration and on the salinity and as the critical micelle concentration (cmc) could not be detected. Time-evolution small angle neutron scattering (SANS) experiments over several months proved that no unimer exchange occurred with the micelles as the high PnBA/water interfacial tension prohibited this. This analysis method was previously used by Lund et al.[54] to prove the kinetically

frozen character of poly(ethylene-propylene)-*block*-poly(ethylene oxide) (PEP-*b*-PEO) micelles. Nevertheless, Jacquin et al.[51-53] showed that their P*n*BA-*b*-PAA system formed kinetically frozen micelles. Mixing these kinetically frozen micelles with non-ionic and ionic surfactants led to melting of the kinetically frozen micelles as the surfactants reduced the P*n*BA/water interfacial energy. The shown mechanism of disintegration of the kinetically frozen micelles incorporated a gradual fractionation, also called polydisperse dispersion mechanism.

Bendejacq et al.[55-57] reported about block copolymers - polystyrene-*block*-poly(acrylic acid) (PS-*b*-PAA) - forming frozen aggregates that could be dispersed into defined aggregates in water without the need of any cosolvent. Those defined aggregates could be annealed and undergo cylinder-to-sphere transitions due to reduction of the interface curvature. This showed that the formation of aggregates with monomodal size distribution in a selective solvent for a specific block copolymer does not automatically induce the formation of dynamic micelles. The same was valid for the cmc and the observation of unimers and micelles in a solution of a block copolymer in a selective solvent.

In literature[58,59] are two different ways discussed how a micelle can rearrange. One way includes the exchange of unimers - similar to surfactants. This mechanism depends on fully dynamic micelles as the exchange of unimers is completly reversible and leads to a system in thermodynamic equilibrium. On the other hand micelles can also rearrange through expulsion of unimers. This is a non reversible process - as the unimer can not re-enter the micelle anymore - and leads to the formation of smaller micelles out of larger ones. Nevertheless, those micelles are not dynamic in a thermodynamic point of view. This explains why a cmc can be detected for the P*n*BA-*b*-PAA[46] system upon dilution - as the larger micelles expulse unimers during dilution till just unimers are present in the solution. Nevertheless, it does not mean that a diluted solution of P*n*BA-*b*-PAA unimers forms micelles upon concentrating the solution. Concluding all the various reported literature upon the P*n*BA-*b*-PAA system, the most reasonable explanation for the behaviour of the P*n*BA-*b*-PAA block copolymer system in water is the formation of kinetically frozen micelles.

1.3   *Star-shaped polymers*

Star-shaped polymers, also called star polymers, can be classified as non-linear or branched polymers. Ideally, star polymers possess only one branching point, from where the arms are grown. In real star polymers usually more than one branching point exists, as the size of the

core of the star has to be taken into account. As long as the core is small compared to the dimensions of the star (e.g. one order of magnitude smaller), the core is regarded as not to influence the behaviour of the stars. Spherical polymer brushes do have a core with a size in the order of the magnitude of the chains or even larger, in contrast to star polymers. Polymers possessing a core with much larger dimensions than the surrounding polymer chains are denoted as planar brushes, as the curvature is small compared to the dimensions of the chains.[60-64]

The most important parameters for the characterization of star polymers are the length of the arms of the star (the degree of polymerization per arm) and the total number of arms per star. Ideally, the number of arms per star molecule would be constant for all star molecules of the same polymerization batch and the arm length would be the same for all arms. Synthetically, this ideal case is almost not possible to achieve for star-shaped systems with a high arm number. Practically, star-shaped polymers possess a distribution in arm length and/or in the arm number, which needs to be determined for the correct characterization of star polymers.[63,64]

Synthesis of star-shaped polymers can be conducted via two strategies, namely the core-first approach and the arm-first method. The core-first method uses multifunctional initiators which are rather tedious to synthesize well-defined. The maximum of the arm number is determined through the number of initiator sites of the core. The initiation site efficiency and the homogeneity of initiation sites per initiator molecule strongly influence the polydispersity of the obtained star polymer. For the arm-first approach linear polymers are required which are crosslinked via small organic or inorganic molecules to a multifunctional termination agent forming the core. Theoretically high average arm numbers can be obtained easily. Practically the obtained star polymers possess a rather broad distribution in arm number.[61,65]

1.4   Polyelectrolytes

Polyelectrolytes are charged polymers combining the features of polymers and of electrolytes. Usually every repeating unit bears an either positively or negatively charged ionisable group. Consequently, polyelectrolytes are classified to belong either to the group of cationic or anionic polyelectrolytes. Polyelectrolytes with mixed architectures possessing both negatively and positively charged monomeric units are denoted as polyampholytes. Synthetic polyelectrolytes have been and continue to be a very active area of scientific research and commercial growth. The fact that polyelectrolyte conformation and their interactions can be controlled by

a number of parameters makes them not only an interesting and rich area for the exploration of novel phenomena but also an area of research which leads to new applications in a extended variety of fields. In industry polyelectrolytes are used as surface-active agents for water treatment, oil-spill treatment, personal care products, cosmetics, pharmaceuticals, ion and gas selective membranes (e.g. for fuel cells), biosensors, surfactants, absorbents, ion exchange resins, stabilizers, flocculants, adhesives, paints, papers and a lot more. Applications in medicine and biomedical engineering are enormously tracked. Complexes of polyelectrolytes and conjugated polymers (e.g. polythiophenes, polyanilines) are commercially used as conducting coatings.[66-68]

Polyelectrolytes are additionally distinguished in strong (quenched) or weak (annealed) polyelectrolytes. The number of charges is fixed for strong polyelectrolytes. They acquire spontaneously full charge after dissolving. Additionally, the amount of charges is independent of changes in pH. They are usually synthesized of monomers being strong acids or bases or the corresponding salts of strong acids or bases. In the case of weak polyelectrolytes the effective amount of charges per molecule is influenced by changes in pH as they are just partially charged when dissolved in pure solvent. Furthermore, solubility of weak polyelectrolytes is affected in basic and acidic media. The most investigated weak polyelectrolytes are poly(acrylic acid) (PAA) and poly(methacrylic acid) (PMAA). Polyelectrolytes are omnipresent in nature e.g. proteins, polysaccharides and ribonucleic acid (RNA) and desoxyribonucleic acid (DNA). Some common synthetic polyelectrolytes are shown in Figure 1.3.[66-68]
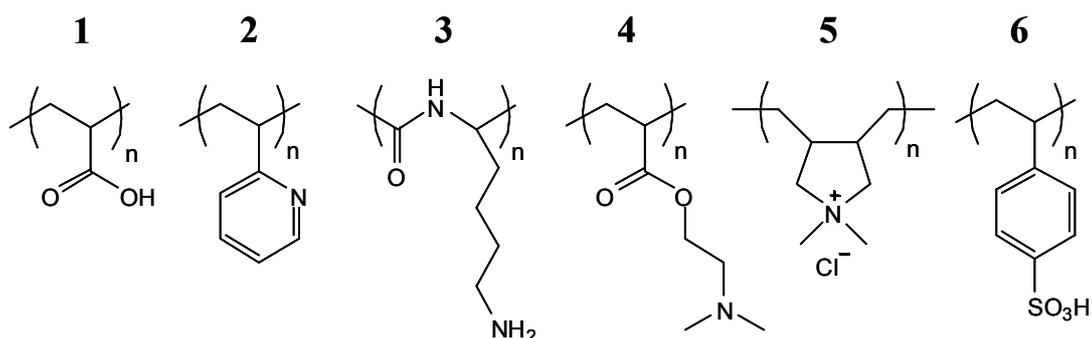
Figure 1.3. Some common synthetic polyelectrolytes: **1** = poly(acrylic acid), **2** = poly(2-vinylpyridine), **3** = poly(lysine), **4** = poly(diethylaminoethyl acrylate), **5** = poly(diallyldiethyl-amino chloride), **6** = poly(styrenesulfonic acid).

The physical properties of polyelectrolytes differ quite strongly from those of uncharged polymers with comparable structure as they exhibit properties related to their macromolecular nature as well as to their electrolytic nature. Uncharged polyelectrolytes behave like usual

macromolecules. Upon charging of polyelectrolytes - even at low extend - things change significantly what was shown experimentally. The properties of polyelectrolytes in solution depend on the fraction of dissociated ionic groups, electrostatic interaction between charges, temperature, the molecular weight of the macromolecule, the nature of the ions, solvent quality for the polymer backbone, solution dielectric constant, and salt concentration. The polyelectrolyte conformation in dilute solution depends on the fraction of charged groups on the polymer, the presence of multivalent counterions and the ionic strength of the solution. For weakly charged polyelectrolytes the interplay between non-Coulombic interactions such as van der Waals interaction, hydrogen bonding and other molecular interactions plays a very important role in determining the conformation of the macromolecule.[66-68]

Ionized polyelectrolytes are accompanied by an equivalent amount of differently charged low molecular mass ions, the counterions. The distribution of the counterions and their strong relation to the ions of the polyelectrolyte (so-called counterion condensation) leads to dramatic effects on the physical properties of polyelectrolytes. The term counterion condensation describes the fact that a huge part of the counterions is not free active in the solution as they are more or less strong bound to the backbone of the polyelectrolyte influencing the osmotic pressure of the polyelectrolyte solution and its electrophoretic mobility. Counterion distribution for stiff linear polymers is well understood. Flexible polyelectrolytes are a lot more difficult to understand due to their strongly coupled behaviour as changes in counterion distribution lead to changes in conformation and vice versa. This behaviour of polyelectrolytes was well described by "the chain tells the ions where to move; the ions tell the chain how to curve"[69].[66-68]

To understand the behaviour of polyelectrolyte solution various theoretical models with different limitations were developed within the last decades. Starting in the 1950s when Fuoss, Katchalsky and Lifson applied the Debye-Hückel theory of strong electrolytes to the system of polyion-counterions and described the effect of charged groups at the polyion and its solution behaviour theoretically. Oosawa and Imai et al. used a simple two-phase model and an analytical solution of the Poisson-Boltzmann equation for charged rods to develop their theories. The theory of counterion condensation, published by Manning[70-73], was a further approach to explain the interactions between polyions and counterions. End of the 1970s Odijk proposed a model for highly charged polyelectrolytes on the basis of a wormlike chain model introducing the total persistence length as the sum of the intrinsic stiffness of the polymer chain and an electrostatic contribution. Based on this model, de Gennes proposed a modified "blob" model for weakly charged polyelectrolytes. Still not all phenomena of polye-

lectrolytes behaviour are understood requiring refinement and improvement of existing polyelectrolyte models.[67,68]

Understanding the different theoretical models requires some definitions. The Debye-Hückel screening length, l_D, is the geometrical dimension of the potential around a point charge screening the electrostatic interactions,

$$l_D = \left(\frac{\varepsilon \varepsilon_0 kT}{2 N_A e^2 I}\right)^{\frac{1}{2}} \qquad \qquad \textbf{1.1}$$

with e as the elementary charge, ε as the relative permittivity of the solvent, ε_0 as the dielectric permittivity of the vacuum, k as the Boltzmann constant, T as the temperature, N_A as Avogadro´s number and I as the ionic strength. l_D can also be seen as a measure for the range of the Debye-Hückel potential. The Debye-Hückel screening length is applied to polyelectrolyte solutions as it is a measure for the extension of the ionic atmosphere around the polyelectrolyte molecule. It depends on the concentration of the polyelectrolyte and the ionic strength created by addition of any low molecular mass electrolyte, e.g. salts. It has to be mentioned that the Debye-Hückel theory is already critical for multivalent low molecular mass ions.[67,68]

A further characteristic length scale, the so called Bjerrum length, l_B, equals the distance of two elementary charges e, where their electrostatic energy is compensated by the thermal energy, kT, of the medium.

$$l_B = \frac{e^2}{4\pi\varepsilon_0\varepsilon kT} \qquad \qquad \textbf{1.2}$$

It is a constant for a given temperature and a given solvent. For example, the electrostatic interaction energy between two charges in water and at room temperature is compensated by the thermal energy at $l_B = 0.714$ nm. Combining both equations leads to

$$l_D = \left(8\pi l_B N_A I\right)^{-\frac{1}{2}}. \qquad \qquad \textbf{1.3}$$

Addition of salt to a polyelectrolyte solution decreases the electrostatic interaction exponentially at length scales larger than the Debye screening length, l_D, due to screening of charges and can be also expressed by,

$$l_D = \left(4\pi l_B \sum_s c_s q_s^2\right)^{-\frac{1}{2}} \qquad \qquad \textbf{1.4}$$

with c_s as the concentration of ions of type s with the valency q_s. In a dilute salt free solution, the concentration of the counterions is very low (the Debye screening length is larger than the chain size) and therefore ionized groups on a chain interact with each other through the unscreened Coulomb potential.[67]

To describe the physical properties of a distinct polyelectrolyte, another dimensionless parameter exists, the so called charge density, ζ, which combines the Bjerrum length with the axial spacing, b, between two charges.[68]

$$\zeta = \frac{l_B}{b} = \frac{e^2}{4\pi\varepsilon_0\varepsilon kT \cdot b} \qquad \textbf{1.5}$$

The electrostatic interactions of polyelectrolyte solutions formed of the polyion, the added salt and the solvent can be described with the Poisson-Boltzmann equation via a diffuse counterion cloud. As the solution of the full nonlinear Poisson-Boltzmann equation is quite difficult to accomplish their linearized version, the Debye-Hückel equation, allows an easier analysis. Nevertheless, both equations are based on the approximation of thermally equilibrated ions, which does not take into account their spatial correlations.[68]

For electroneutrality in a polyelectrolyte solution, counterions have to be present, as already mentioned. It can be energetically favoured under certain conditions that a definite fraction of the counterions is located close to the surface of the polyelectrolyte to reduce the polyions charge. To determine conditions under which it is thermodynamically advantageous for a finite amount of counterions to "condense" close to the polyelectrolyte, the concept of counterion association/condensation was introduced. The concept quantifies the polyion-counterion interaction. The fundamental contributions came from Fuoss, Katchalsky, Lifson, Oosawa and Manning.[70-81]

The "two-state" model of Manning[70-73] in its original state is frequently used and is based on (1) replacement of the polyion charge density by a line charge density, (2), neglecting the polyion-polyion interactions, (3) application of the dielectric constant of the solvent, (4) condensation of counterions until the Manning parameter, ζ, is ≤ 1 and (5) treatment of uncondensed counterions by the Debye-Hückel approach. According to Manning´s theory the space around an ideally stiff, linear polyelectrolyte is divided in two cylinders with the ions that are differently strong bound (Figure 1.4). The counterions within a cylinder with radius r_c are condensed and only able to move near the polyelectrolyte backbone whereas uncondensed ions are able to move freely in a cylinder with radius r_f.
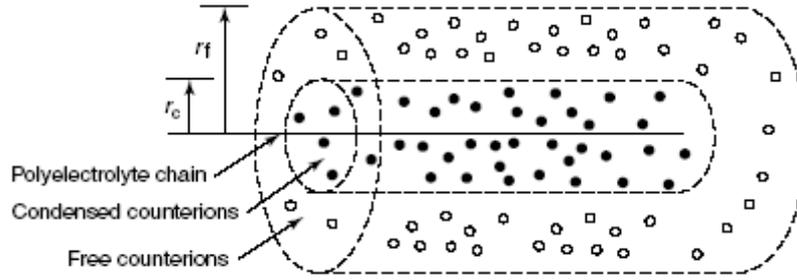
Figure 1.4. Two-state model for stiff, linear polyelectrolytes describing two regions of counterions according to Manning.

As already mentioned, the thermodynamic properties of polyelectrolyte solutions are strongly influenced by the interaction between the polyion and counterions. According to the counterion condensation theory, counterions are thought to be condensated on a polyion for $\zeta = \dfrac{l_B}{b} > 1$ until the apparent charge density parameter, ζ, is reduced to unity, whereas the counterions are not condensed for $\zeta < 1$ when the valence of the counterion and the charged group of the polyion is unity. The meaning of the parameter ζ is that if $\zeta > 1$, then the average spacing b is reduced by counterion condensation until $\zeta = 1$. The minimum accessible charge spacing is equal to the Bjerrum length. The onset of counterion condensation is experimentally observed through the reduction in the effective polyion charge. However, this polyion charge can in practice be adjusted within the limits of counterion condensation by changing the pH of the solution. For $\zeta > 1$ the electrostatic effect dominates. Counterion condensation occurs, whereas for $\zeta < 1$ the entropy dominates and the counterions can move freely in the solution.[67,68]

Summing up, counterion condensation appears to be a fine interplay between the electrostatic attraction of a counterion to a polymer chain and the loss of the translational entropy by counterions due to their localization in the vicinity of the polymer chain. In a very dilute polyelectrolyte solution the entropic penalty for counterion condensation is very high and almost all counterions leave the polymer chains and stay "free" in solution. However, as the polymer concentration increases, the entropic penalty for counterion localization decreases resulting in a gradual increase in the number of condensed counterions. For polyelectrolyte solutions in a good or theta solvent for the polymer backbone the fraction of free counterions decreases logarithmically with increasing polymer concentration.[67,68]

The theoretical models for linear polyelectrolytes have to be expanded to describe the behaviour of star-like polyelectrolytes. Beside counterions, which are directly condensed at

the backbone of the polymer, there are also uncondensed counterions to be encountered within the star-like polyelectrolyte. Those counterions do not contribute to the free counterions in bulk solution, which are supposed to be responsible for e.g. the osmotic pressure of such systems.[82-84]

1.5 Polyelectrolyte complexes

Polyelectrolyte surfactant complexes (PESCs) are obtained via the complexation of charged homopolymers with oppositely charged surfactants.[85] Babak et al. reported about an electrostatic complex formed by chitosan as a semi-rigid positively charged polyelectrolyte and sodium dodecyl sulphate (SDS) as anionic surfactant.[86] Another attempt is to form complexes between oppositely charged polyelectrolytes being called interpolyelectrolyte complexes (IPECs). They have been intensively studied over the last decades.[85] Polyelectrolyte complexes formed on a solid substrate via the commonly known layer-by-layer technique[87] from aqueous solutions of homopolymers and micelles offer another interesting form of polyelectrolyte complexes. Multilayers of oppositely charged polymers are obtained which are connected via electrostatic interactions. They can be described similar to IPECs. The formation of complexes of amphiphilic block copolymers and homo polyelectrolytes as well as block copolymers has attracted increasing attention. Especially the complexation of linear amphiphilic block copolymers with oppositely charged polymers is interesting for drug delivery, drug release and biological carrier systems. An important field of interest is the IPEC formation between polyelectrolytes and biological building blocks like proteins or DNA representing natural polyelectrolytes.

IPEC formation results in the formation of interpolymer salt bonds between the oppositely charged polyelectrolytes due to strong electrostatic interactions. Additionally, complexation between polyelectrolytes leads to release of low molecular counterions from the system. For complexation of homopolymers, it is already reported that water-soluble complexes can be obtained by mixing weak polyelectrolytes as polyacids or their salts with polybases.[85] The driving force for the complex formation is the release of counterions resulting in an increase in entropy.

The composition and molecular characteristics of the polyelectrolyte components strongly influence the resulting IPEC. Other parameters like ionic strength and pH of the surrounding medium also have an impact on the properties and structure of the formed com-

14

plexes. The charge ratio, $Z = \dfrac{[+]}{[-]}$, of the polyanion compared to the added polycation has a huge effect on the IPEC. It is defined as the ratio of positive and negative charges within the polymer chain and has to be hold beneath a certain threshold. The explanation lies in the reduced polarity of the formed IPEC compared to the original polyelectrolyte chains. Consequently, IPECs with $Z \neq 1$ are stabilized by the overall charge of the component in excess. For the case of $Z \approx 1$, the so called stoichometric regime, with an overall net charge of the IPEC of zero the absence of stabilizing charges leads to precipitation and therefore to macroscopic phase separation in aqueous solutions. To overcome the problem of precipitation it was reported on complexation of polyelectrolytes with diblock copolymers possessing an oppositely charged block which needs to be water soluble to avoid precipitation of the formed complex. Also polyelectrolytes with hydrophilic non-ionic blocks like poly(ethylene oxide) are reported to stabilize the formed aggregates and thus prevent precipitation in the stoichometric regime.[88] Such systems are often regarded as block ionomer complexes due to the fact that one component is rather an ionomer than an ideal polyelectrolyte. The obtained aggregates are often well defined micelles consisting of a dense IPEC core surrounded by a corona of a water soluble polymer.

Pergushov et al. as well as Burkhardt et al. showed that micelles of polyisobutylene-*block*-poly(sodium methacrylate) (PIB-*b*-PMANa) by interacting with the polycation poly(N-ethyl-4-vinylpyridinium bromide) in alkaline media form complex co-assemblies which are considered as water-soluble micellar IPECs.[89-91] The stoichiometry of such complex co-assemblies has to be well below the charge equality. The complex particle as a whole is kept in solution through the remaining polyelectrolyte blocks (or their fragments) in the micellar corona. A multilayer model was proposed for the formed water-soluble IPEC species, i.e. an onion-like micelle consisting of a PIB core surrounded by an IPEC shell and an ionic corona of PMANa blocks (or their fragments) that are not involved in the interpolyelectrolyte interaction.

Pergushov et al. also studied the complex formation of star-shaped poly(acrylic acid) (PAA) with various arm numbers (5, 8 and 21 arms) and a strong cationic polyelectrolyte.[92] Mixing of these polyelectrolytes resulted in the formation of two coexisting populations of complex species considerably differing in their size. The formed complex solutions remain transparent until their base-molar ratio exceeds a specific value depending on the arm number of the used star polymer and the ionic strength of the solution. The small complex species forming the major fraction of the mixture are assumed to represent the water-soluble IPECs.

The minor fraction of a large complex species is considered to be aggregates of complexes build through crosslinking of stars through the cationic polyelectrolyte.

1.6   Nanohybrids

Commonly the term "nanomaterials" denotes materials with dimensions in the range from 100 nm down to the atomic level of 0.2 nm. This research field is of steadily increasing interest as with the decrease in size the relative surface area of the nanoobjects increases drastically leading to an extremely high chemical reactivity. The combination of such nanoscaled materials with common polymeric compounds offers the possibility to generate novel materials with outstanding properties. Frequently, those materials are of inorganic nature resulting in so called organic-inorganic nanohybrids possessing improved mechanical, thermal, electrical or flame retardancy properties, depending on their composition. Organic-inorganic hybrid materials have found huge interest, in particular in the areas of biomaterials, optical and mechanical applications. These hybrids combine both organic and inorganic material properties, leading to new materials with unique properties.{Kickelbick, 2007 #59; Rodríguez-Hernández, 2005 #62; Riess, 2003 #70; Garnier, 2003 #72; Hoffmann, 2006 #105}

An advantage over pure inorganic materials is their easier processing. An important class of hybrid materials contains silica or silsesquioxanes as the inorganic component. The organic and inorganic components can be simply mixed, e.g. in nanocomposites[93-102], they can be attached in a covalent way[94,97,98,103-110] or they can form defined complexes [97,98,111-113]. For example the incorporation of silsesquioxanes into standard polymers like poly(methacrylate) leads to increased decomposition temperatures and reduced flammability.[114] Magnetic nanoparticles can be used for the construction of multifunctional hybrid nanosystems, where the magnetic properties can additionally be combined with polymer properties like LCST or pH dependent solubility to obtain nanohybrids that are responsive to several external stimuli.[115]

The preparation of polymer-nanoparticle assemblies is not a straightforward task. Due to entropic depletion associated with chain stretching nanoparticles are commonly not readily miscible with polymers.[116,117] Only strong enthalpic interactions may overcome the entropic penalty and may promote the mixing of nanoparticles with polymers. One important driving force is ionic interaction.

Different routes to obtain nanohybrid materials exist. First of all, the direct mixing of inorganic compounds to polymers is to mention, where the nanoparticles has to be functional-

ized to prevent aggregation and to obtain a homogeneous distribution. For silica nanoparticle this can be directly achieved through functionalizing the silica surface with triethoxysilanes, which possess adequate compatible organic groups.[118] Another method is to use the nanoparticles after adequate modification as initiator for surface initiated polymerizations and to grow the polymer directly from the inorganic substrate via a "grafting from" approach.[119] Copolymerization of a monomer bearing inorganic residues, e.g. allyl functionalized triethoxysilanes, and a common monomer offers after polymerization of well defined structures a new route to nanohybrids.[110] In a completely different synthetic approach the polymer itself is used as a template for growing nanosized objects.[120] The formation of self-assembled nanohybrids can be obtained through complexation of previously synthesized nanoparticles and polymers. Via external stimuli the strength of interaction and amount of incorporated nanoparticles may be controllable.

A lot of research has been conducted in the promising field of smart materials, i.e., materials that possess the possibility to react on external stimuli like pH, salinity, or temperature. These materials offer new applications, for example in electroactive materials, electrochromic materials, sensors, membranes, drug delivery, emulsifiers, foam stabilizers, detergents, nanocontainers, catalysis and biohybrid materials.{Garnier, 2003 #72; Riess, 2003 #70; Hales, 2006 #71; Rodríguez-Hernández, 2005 #62; Gil, 2004 #61} In particular, weak polyelectrolytes like poly(acrylic acid) (PAA) or poly(N,N-dimethylaminoethyl methacrylate) (PDMAEMA) can react with changes in structure and solubility on changes in pH, salinity or on addition of multivalent counterions.[10,20-24,27,29,34,36-41] Their combination with inorganic materials offers the chance to develop new nanosized smart organic-inorganic materials.[27,28,121]

Mori et al.[112,113] described the interaction of *tert*-amino- and hydroxyfunctional silsesquioxane nanoparticles (Figure 1.5) with linear PAA in aqueous and methanolic solutions. These nanoparticles were made from diglycidylaminopropyltriethoxysilane in an acid-catalyzed condensation and have about 14.2 Si atoms and diglycidylamino functions on average. They have irregular, cage-like structures.[122] They observed pH-dependent turbidity changes during the pH titration of an aqueous mixture of silsesquioxane nanoparticle and linear PAA with a degree of polymerization (DP) of 100. The strongest turbidity was found between pH 2.5 and 5.7. They proposed a pH-dependent complexation mechanism between the acid functions of PAA and the hydroxyl- as well as the amino functions of the nanoparticles. Furthermore they investigated the dependence of these complexes upon salinity in water and methanol.
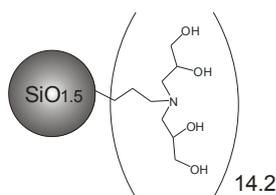
Figure 1.5. Structure of the highly functionalized silsesquioxane nanoparticles used.

Retsch et al.[123] reported also on the pH-dependent interaction of these silsesquioxane nanoparticles with planar PAA brushes grafted onto a gold surface. The strongest interaction was found at pH = 5.3. Thus, these silsesquioxane nanoparticles penetrate into the PAA brush at pH 5.3 but can be liberated at higher or lower pH.

Such interactions resemble the well-known complexation between complementary polymers resulting in the formation of inter-macromolecular complexes stabilized via multisite interactions, either hydrogen bonding[124,125] or ionic interactions[124,126-128] of complementary units of the coupled polymers. Complexes formed by oppositely charged polyelectrolytes, (IPECs) precipitate once a certain charge ratio is exceeded.[30,39,85,88-92,129-137] In contrast to most IPECs reported in the literature we deal here with two weak polyelectrolytes and the number of ionizable groups in the nanoparticle is rather low (14 tertiary nitrogens).

The interest of this thesis is to show in how star-like polyelectrolytes (stars and micelles) - representing an increase of the degree of organization compared to linear PAA - would interact with the highly functional silsesquioxane particles. Our system presented here follows the same simple mixing procedure of two transparent aqueous solutions to yield a nanohybrid system through the complexation of the PAA arms of the organic amphiphilic star-like polymer with the inorganic silsesquioxane nanoparticles. Upon complexation various morphological changes may occur. The dimensions of the polyelectrolyte star-like polymer may be altered by external stimuli like salinity or pH. The silsesquioxane nanoparticles may act as crosslinkers for the polyelectrolyte star-like polymer, leading to larger aggregates e.g. through coupling or crosslinking. They may also interact with the PAA chains inside a single star-like polymer, resulting in a new class of hybrid materials. Furthermore, they may give a deeper insight into the complexation mechanism of IPECs and organic-inorganic nanohybrids. The potential effects on the dimension of the polyelectrolyte shell on the organic-inorganic nanohybrids are investigated as a function of salinity and pH. This system may act as a model system for the investigation of water-soluble and stimuli-responsive organic-

inorganic nanohybrid star-like polymers based on silsesquioxane nanoparticles as complexation is easily achieved by a simple solution mixing technique in aqueous media.

1.7   Objective of the thesis

In this work the interaction of weak polyelectrolytes and highly functionalized *N,N*-di(2,3-dihydroxypropyl)3-aminopropylfunctional silsesquioxane nanoparticles (diameter $\approx$ 3 nm) is investigated. For the polyelectrolyte part poly(acrylic acid) (PAA) with star-like structure was chosen. Two different PAA star systems [(PAA$_{100}$)$_{21}$ and (PAA$_{200}$)$_{24}$] with different arm length but comparable arm numbers were investigated. They possess a hydrodynamic radius in the range of 10 nm. Net polyelectrolyte stars were chosen as they can serve as a model system for frozen star-like micelles.

Poly(*n*-butyl acrylate)-*block*-poly(acrylic acid) (P*n*BA$_x$-*b*-PAA$_y$ with x = 90, 100 and y = 100, 150, 300 as DP) are known to form kinetically frozen micelles upon dilution in basic media. They were used as pH- and salinity-tunable star-like micelles. Stars and star-like micelles represent an increase of order compared to linear PAA which has been used by Mori et al.[112,113] to investigate the interaction of weak polyelectrolytes and silsesquioxane nanoparticles (page 16ff.).

The aim of this thesis is to investigate the interaction of the star-like weak polyelectrolyte systems on PAA basis with the silsesquioxane nanoparticles. The formation of organic-inorganic nanohybrids should be shown. Furthermore, the structure of the newly formed nanohybrids was of interest. The interaction could lead to single, individual and separated nanohybrids or to larger aggregates of via the silsesquioxane nanoparticles crosslinked stars or micelles, respectively. In this work the proof of the formation of the organic-inorganic nanohybrids and investigations upon their shape were performed via dynamic light scattering (DLS), cryogenic transmission electron microscopy (cryo-TEM), static light scattering (SLS), asymmetric flow field-flow fractionation (AFFFF), small angle neutron scattering (SANS), dialysis experiments with fluorescently-labelled silsesquioxane and Fourier-transform infrared spectroscopy (FT-IR) measurements.

Special focus was put on the behaviour of the organic-inorganic nanohybrids upon external stimuli like changes in pH and salinity to demonstrate if they show responsiveness to those external stimuli. They might undergo structural changes as well as the amount of incorporated silsesquioxane nanoparticles per acid functionality might be influenced.

This question requires analysis methods that enable quantification of the amount of interacting silsesquioxane nanoparticles. There are light scattering (LS) experiments, especially

LS titration measurements and SLS experiments to mention. AFFFF with SLS detection offers the possibility to quantify the amount of interacting nanoparticles and also to determine the size of the formed organic-inorganic nanohybrids. Thermogravimetric analysis (TGA), isothermal titration calorimetry (ITC) measurements and SANS experiments also offer quantitative data. SANS experiments and the fitting of the experimental data via an appropriate fitting model can also provide information about the size and radial profile, which is used to obtain insight to the inner structure of the formed organic-inorganic nanohybrids. Furthermore, influences of treatments required prior to the performed measurement (e.g. dialysis) were investigated especially to prove if responsiveness of the system exists and to show the influence on the amount of incorporated silsesquioxane nanoparticles.

2 Experimental Part and Methods

2.1 Materials

Millipore (Milli-Q, deionized water) water was freshly taken from the Millipore+ apparatus, equipped with filtration packs QPAK2E (0.5 μm prefilter, macroreticular activated carbon, high purity mixed bed ion exchange resin, Organex polisher). The resistance of the Millipore water was always around 18.2 MΩ, ensuring that ions were sufficiently removed. NaCl (Riedel de Haën, p.a.), CsCl monohydrate (Fluka, ≥ 95 %), CsOH (Acros, p.a.) and NaOH platelets (Merck, p.a.) were used as received. HCl (0.1 N) and NaOH (0.1 N) stock solutions were prepared with Millipore water and Titrisol (Merck) stock solutions. *Tert*-butyl acrylate (*t*BA), acetone, ethylacetate, *N,N,N',N'',N''*-pentamethyldiethylenetriamine (PMDETA), CuBr, $CuBr_2$, CaH_2 and CH_2Cl_2 were bought from Aldrich in highest available purity. Rhodamine B base (Sigma-Aldrich, dye content 97 %), phosphorus oxychloride ($POCl_3$, Sigma-Aldrich, 99 %), 1,2-dichloromethane (Sigma-Aldrich, p.a.), methanol (MeOH, Sigma-Aldrich, p.a.), dimethylformamide (DMF, Merck, p.a.) and 4-*N,N*-dimethylamino-pyridine (DMAP, Sigma-Aldrich, ≥ 99%) were used as received. Sephadex SG-25 (Sigma-Aldrich) was swollen with Millipore water at 90 °C for 3 hours before using.

2.1.1 Amphiphilic block copolymers

The synthesis of the amphiphilic block copolymers poly(*n*-butyl acrylate)-*block*-poly(acrylic acid) ($PnBA_x$-*b*-PAA_y with x = 90, 100 and y = 100, 150, 300 as the degree of polymerization) with narrow molecular weight distribution (PDI ≤ 1.07) included the sequential atom transfer radical polymerization (ATRP) of the monomers *n*-butyl acrylate (*n*BA) and *t*-butyl acrylate (*t*BA). The *t*BA group was selectively acidolyzed with excess trifluoroacetic acid in dichloromethane at room temperature to get poly(acrylic acid) (PAA) without acidolysis of the P*n*BA part of the block copolymer (Figure 2.1). The details have been published.[46]

1. CuBr, PMDETA,
   Methyl-2-bromopropionate,
   acetone, 60 °C

2. work up

1. CuBr, CuBr$_2$,
   PMDETA, tBA
   acetone, 60 °C

2. work up

nBu

R x Br

O O

nBu

1. CH$_2$Cl$_2$, F$_3$C-COOH,
   48 h, RT

2. work up

R x y Br

O O   O O

nBu   H

R x y Br

O O   O O

nBu   tBu

x = 90, 100
y = 100, 150, 300
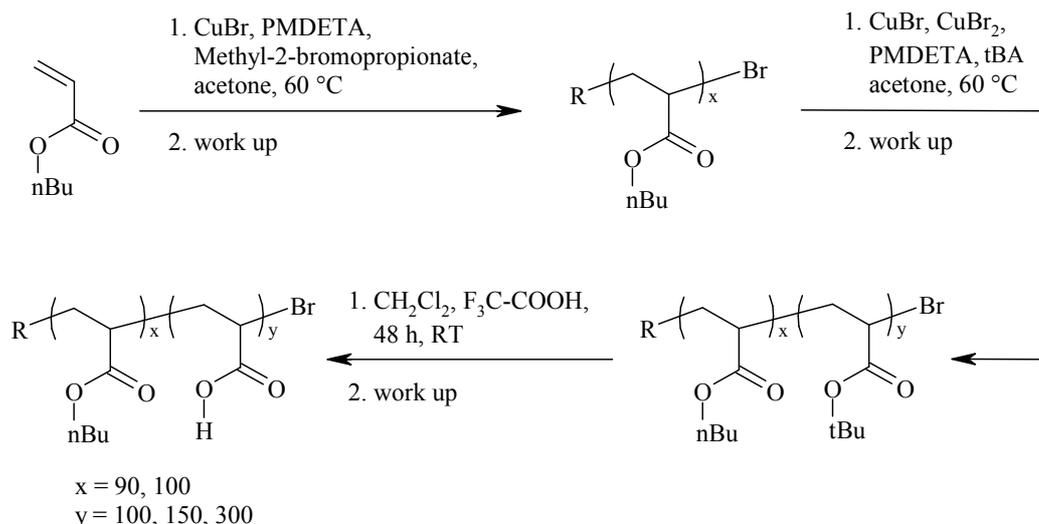
Figure 2.1. Synthesis of the amphiphilic block copolymers used.

2.1.2 Poly(acrylic acid) stars

The synthesis and characterization of the star-shaped poly(acrylic acid) (PAA) with 21 arms and a degree of polymerization (DP) of 100 per arm (denoted as (PAA$_{100}$)$_{21}$) via atom transfer radical polymerization (ATRP) of *tert*-butyl acrylate (*t*BA) as a core-first approach using cyclodextrin-based initiator with subsequent acid treatment of the P*t*BA groups to PAA was reported.[138]

(PAA$_{200}$)$_{24}$ stars were synthesized via a comparable route as the (PAA$_{100}$)$_{21}$ stars. The published synthesis[139] of the macroinitiator included the above mentioned silsesquioxane nanoparticles that were functionalized with 2-bromo-2-methylpropionyl bromide. According to NMR, FT-IR spectroscopy, elemental analysis (EA) and MALDI-Tof MS analysis those macroinitiators possessed an average of 58 initiation sites per molecule. The star synthesis was performed by ATRP of *t*BA with subsequent acid treatment of the P*t*BA to PAA via a similar synthesis method as was used for the (PAA$_{100}$)$_{21}$ star. Therefore silsesquioxane nanoparticle macroinitiator (0.758 g, 3.55*10^{-3} mol initiation sites), CuBr (0.57 g, 4.0*10^{-3} mol), *t*BA (150.8 g, 1.17 mol; monomer dried over CaH$_2$ and filtrated over basic alumina) and the solvent acetone (157 g) were weighed into a septum-sealed flask. Under ice cooling, this mixture was degassed by purging nitrogen through the mixture for 30 min, followed by heating the mixture up to 55 °C. After 5 min a predetermined amount (2.61 g) of a mixture of PMDETA (0.62 g, 3.6*10^{-3} mol), ethylacetate (1.31 g), acetone (0.66 g) and CuBr$_2$ (17 mg, only partly dissolved after 1 h; only the soluble part was added to the polymerization mixture) was introduced into the monomer mixture. After 50 % conversion (determined by NMR, 8805

min) the reaction was stopped by opening the septum and dilution with acetone (~150 g). The crude mixture was concentrated and afterwards dissolved in CH_2Cl_2 for subsequent filtration over silica to retain copper compounds. Further concentration and dissolution in dioxane was used for freeze drying to yield 55 g of P*t*BA star product. The molecular weight (M_n) and the molecular weight distribution were determined by gel permeation chromatography (GPC) with viscosity detection. It could be shown for the star-shaped product that M_n(GPC-visco) = $1.0*10^6$ g/mol (PDI = 1.4) coincides with the theoretical molecular weight obtained by conversion ($M_{n,}$(theo)= $1.1*10^6$ g/mol).
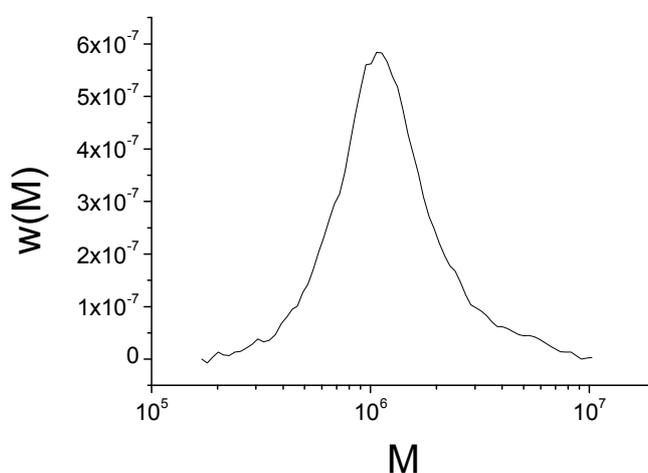
Figure 2.2. THF-GPC trace of the P*t*BA star product.

A mixture of 25g P*t*BA star polymer (dissolved in 300 g dichloromethane) and 112 g trifluoroacetic acid was stirred over night. The solvents were decanted the following day. The precipitate was washed with 50 mL dichloromethane, followed by 50 mL acetone afterwards, yielding to 15 g star polymer. Further purification was obtained by dialysis (MWCO 12000) against water for 24 h and subsequent freeze drying. The P*t*BA stars possessed an arm number of 40, which was derived through determination of the initiation site efficiency using cleavage of the arms by NaOH. This was done after transformation to PAA via the same method as already published for the $(PAA_{100})_{21}$ stars.[138] The observed initiation site efficiency was 0.7 and originated from the congestion caused by the high density of initiation sites around the macroinitiator. However, consecutive transformation of P*t*BA to PAA was always accompanied with partial destruction of the inorganic silsesquioxane macroinitiator residue, yielding to fragments with up to four arms (Figure 2.3). This was irrespective to the acid catalyst used for isobutylene elimination (trifluoroacetic acid, toluenesulfonic acid).
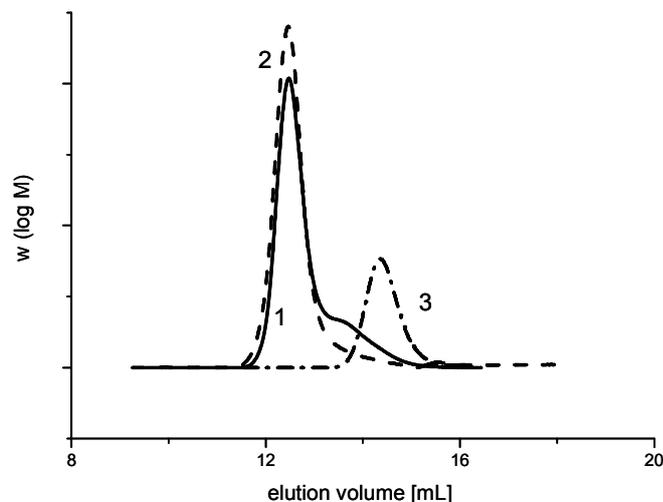
Figure 2.3. Comparison of the elugrams of the GPC analysis in aqueous medium of the crude transformed PAA star (1 ━), the purified PAA star polymer (2, ━ ━) and the detached PAA arms (3, ━··━) of the star polymer.

The stars could be separated from the low molecular weight stars by fractionated precipitation (Figure 2.3). Therefore 3 g were dissolved in approximately 400 mL isopropanol. Diethylether was added close to the point the star polymer starts to precipitate. The beaker was placed in a bigger beaker containing diethylether. At closed conditions and under stirring at room temperature further diethylether condensed slowly and gave different fractions of high molecular weight products which were separated by centrifugation. GPC analysis in aqueous medium helped to find the best fraction (~ 0.3 g, Figure 2.3). The arm number was determined after methylation of the PAA star to poly(methyl acrylate) PMA according to the published procedure[138] for the $(PAA_{100})_{21}$ stars. The molecular weight (M_n) and the molecular weight distribution of PMA stars were determined by Gel Permeation Chromatography (GPC) with viscosity detection ($M_n = 3.911 * 10^5$, $M_w = 4.202 *10^5$; PDI = 1.07) showing that there is still a small trace of 22 % of the low molecular weight star within the fractionated star polymer. The main product is the $(PAA_{200})_{24}$ star.

2.1.3 Silsesquioxane nanoparticles

The synthesis of the silsesquioxane nanoparticles was a straightforward two-step synthesis (Figure 2.4). The addition reaction between 2 molecules of glycidol and (3-aminopropyl)triethoxysilane to *N,N*-di(2,3-dihydroxypropyl)(3-aminopropyl)triethoxysilane

was followed by an hydrofluoric acid catalyzed hydrolytic condensation reaction.[112,113,122] This led to well-defined silsesquioxane nanoparticles with an average diameter of 3 nm and a calculated cage-like structure of $(R\text{-}SiO_{1.5})_n$ with n = 12 to 18 (number-average n = 14.2). The inner structure of the silsesquioxane nanoparticles as well as their size was confirmed by various analytical methods including elemental analysis (EA), transmission electron microscopy (TEM), atomic force microscopy (AFM), scanning force microscopy (SFM), Fourier-transform infrared spectroscopy (FT-IR), nuclear magnetic resonance spectroscopy (NMR) and matrix assisted laser desorption and ionization time-of-flight mass spectroscopy (MALDI-ToF MS).[122] The silsesquioxane nanoparticles were well soluble in polar protic solvents like water or methanol and insoluble in less polar solvents. The cage-like structure provided the high functionality of the silsesquioxane nanoparticles. The amino functionalities as well as the hydroxyl functionalities offered the possibility to interact with polyelectrolytes via ionic or hydrogen bonds.[112,113,122]
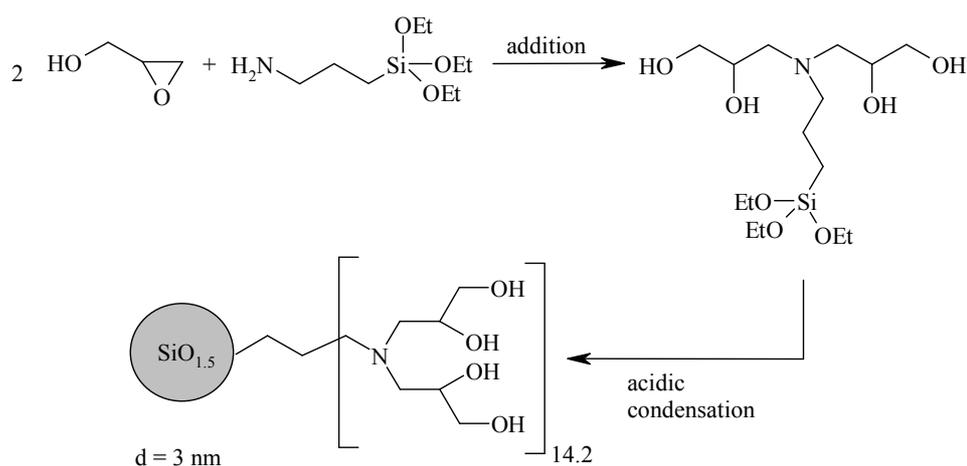
Figure 2.4. Synthesis of the silsesquioxane nanoparticles used.

The synthesis of the fluorescently-labelled silsesquioxane nanoparticles was performed in a two-step procedure. First Rhodamine B acid chloride was synthesized according to a modified literature procedure.[140] A solution of Rhodamine B base (2.5 g, 5.6 mmol) in 1,2-dichloromethane (20 mL) - dried over molecular sieve (3 Å) over night - was stirred under nitrogen, and phosphorus oxychloride (0.98 mL, 10.6 mmol) was slowly added drop wise over a period of 5 min. The solution was refluxed for 5 h at 90 °C. The colour turned from dark red to dark purple. TLC in pure MeOH indicated full conversion after 4 hours. After filtering the dark purple solution using syringe filters (PTFE 0.45 μm) and evaporation of the solvent the dark purple oily product was dried under vacuum (4.5 mbar) at 45 °C over night

resulting in a dark-bronze coloured solid. The crude product was used without further purification.

In a second step the silsesquioxane nanoparticles and 4-*N,N*-dimethylamino-pyridine (DMAP) were dissolved in anhydrous DMF under nitrogen atmosphere. After complete dissolution 2.5 mL of a 0.2 M Rhodamine B acid chloride solution - prepared in anhydrous DMF under nitrogen - was added. The reaction was monitored for three days by TLC while stirring at 40 °C under nitrogen. The solvent was evaporated (reduced pressure at 70 °C) yielding a dark violet high viscous oil that was further dried under vacuum at 45 °C for two days. The crude product was dissolved in alkine Millipore water (0.1 M NaOH) and extracted three times with small amounts of dichloromethane. The aqueous phase was freeze-dried and further purified applying a Sephadex size exclusion filtration with SG-25.

2.2 Preparation of Solutions

2.2.1 Preparation of micellar solutions

All micellar stock solutions ($c_{polymer, max}$ = 5 g/L) were obtained by the following procedure. The amphiphilic block copolymer was dissolved in NaOH solution over night at room temperature under stirring. The amount of sodium hydroxide was calculated as 10 % excess with respect to the COOH groups of the weighed block copolymer to ensure complete deprotonation of the PAA blocks.
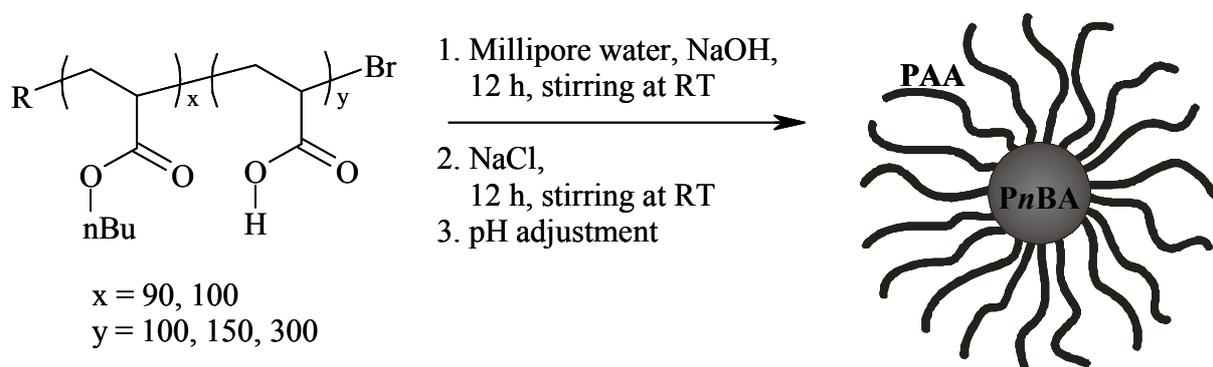

Figure 2.5. Formation of star-like micelles from amphiphilic P*n*BA$_x$-*b*-PAA$_y$ block copolymers.

After addition of the desired amount of NaCl the polymer solution was stirred again for at least 12 hours (Figure 2.5). Adjustments of pH were performed by slow addition of 0.1 M

HCl solution under stirring. Micellar stock solutions were diluted by addition of Millipore water with the same salt content and pH compared to that of the initial solution. All micellar solutions were transparent and showed low viscosity after addition of NaCl. Micellar solutions without added NaCl showed higher viscosity due to electrostatic repulsion between the micelles.

2.2.2 Preparation of silsesquioxane nanoparticle solutions

The transparent silsesquioxane nanoparticle stock solutions were prepared by dissolving the glassy nanoparticles in Millipore water under stirring at room temperature. The required amount of solid NaCl was added after one hour.

2.2.3 Preparation of PAA star solutions

All star stock solutions ($c_{polymer, \, max}$ = 5 g/L) were obtained by an analogues procedure like the preparation of the micellar solutions. The amphiphilic star polymer was dissolved in NaOH solution over night at room temperature under stirring. The amount of sodium hydroxide was calculated as 10 % excess with respect to the COOH groups of the weighed star polymer to ensure complete deprotonation of the PAA. After addition of the desired amount of NaCl the polymer solution was stirred for at least 12 hours. Adjustments of the pH were performed by slow addition of 0.1 M HCl solution under stirring. The stock solutions were diluted by addition of Millipore water with the same salt content and pH as the initial stock solution. All solutions of the PAA stars were transparent and exhibited low viscosity.

2.2.4 Preparation of organic-inorganic nanohybrids

Micelles

Complexation was achieved by slow addition of the nanoparticle stock solution to the micellar solution with the same ionic strength under stirring (Figure 2.6). When required, the aqueous organic-inorganic nanohybrid solutions were dialyzed against Millipore water at equal pH and salinity to remove excess silsesquioxane nanoparticles (Serva Electrophoresis GmbH, Servapore: MWCO 12000-14000). Dialysis cells were used to avoid dilution effects. All solutions were equilibrated by stirring for at least 12 hours at room temperature before measure-

ments were performed. All organic-inorganic nanohybrid solutions were transparent and had low viscosity.
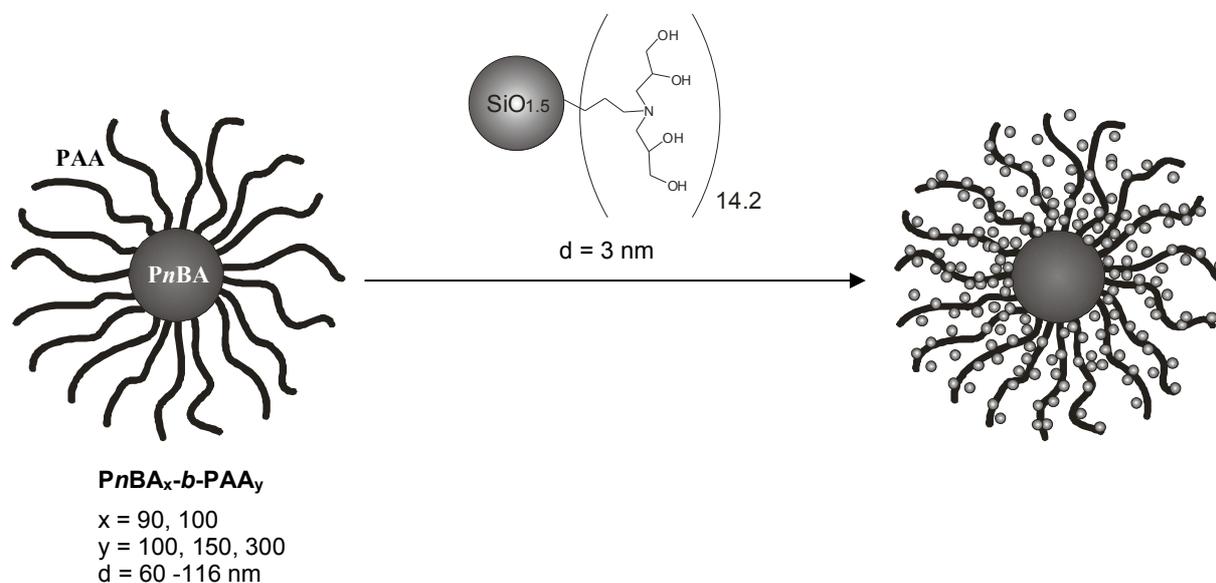
Figure 2.6. Formation of organic-inorganic nanohybrids composed of $PnBA_x$-b-PAA_y micelles and silsesquioxane nanoparticles.

Stars

Complexation was achieved by slow addition of the silsesquioxane nanoparticle stock solution to the star solution with the same ionic strength under stirring. All solutions were equilibrated by stirring for at least 12 hours at room temperature prior to the measurements. All nanohybrid star solutions were transparent and showed low viscosity.

2.3 Light scattering

Light scattering is an easy accessible, fast and powerful tool for structure determination of soluble systems. Scattering is one way of interaction of light with particles. The other ways are absorption and transmittance. The combination of all contributions leads to

$$I_0 = I_S + I_{tr} + I_{abs} \qquad\qquad \textbf{2.1}$$

with I_0 as the incident intensity, I_S as the scattered intensity, I_{tr} the transmitted intensity and I_{abs} the absorbed intensity. Light scattered from particles scatters in all directions (Rayleigh scattering) as long as the particles are small compared to the wavelength (< 250 nm). If absorption can be neglected, scattering is the process that is used in static light scattering (SLS) and dynamic light scattering (DLS). The determination of the hydrodynamic radius, R_h, via

the diffusion coefficients, D, can be done via DLS measurements. SLS measurements lead to the determination of the radius of gyration, R_g, the molecular weight, M_w, and the second virial coefficient, A_2, giving information about the interactions of the polymer with the solvent or other polymer molecules.[4,5]

In DLS fluctuations of intensity are recorded, being a measure of the diffusion of the particles through the scattering volume. In contrast to that, in SLS the total scattering intensity of a species is measured at different concentrations and angles, leading to a so called Zimm- or Berry-plot, where the slopes and the intercept allow the calculation of the mentioned parameters.[4,5]

For all light scattering experiments it is necessary to know the refractive index of the solvent and to determine the refractive index increment dn/dc (page 38). Furthermore, dust needs to be avoided through filtration of the solutions prior to the measurement. Large particles like dust would lead to wrong results as the scattering intensity depends on the 6th power of the radius. A typical setup for light scattering experiments is shown in Figure 2.7.
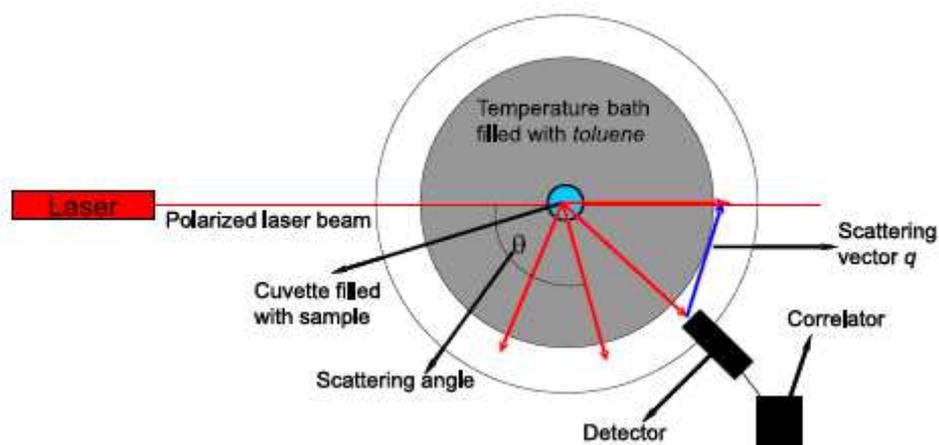
**Figure 2.7.** Schematic setup for a light scattering experiment consisting of a laser, a scattering sample, a movable photon detector and a photon correlator (DLS).

Polarized laser light is scattered by a sample placed in a scattering cell in a toluene refractive index matching bath. The scattered light can be detected by a photon multiplier at different angles. A photon correlator enables DLS measurements.[4,5,141,142]

2.3.1 Static light scattering (SLS)

The total intensity of the scattered light of a dilute polymer solution is proportional to the polymer concentration and the molecular weight. In the case of polymer solutions, Rayleigh and Debye scattering play the most important role.

When an isolated scattering particle (polymer molecule) is small compared to the wavelength of the incident light, λ (generally, diameter of molecule $< \lambda/20$), the polymer molecule can be regarded as a single scattering center and in this case the scattering intensity can be calculated from Rayleigh scattering theory according to

$$\frac{Kc}{R_\Theta} = \frac{1}{M_w} + 2A_2c + \dots \qquad \textbf{2.2}$$

with

$$K = \frac{4\pi^2 n^2 (dn/dc)^2}{\lambda^4 N_A} \qquad \textbf{2.3}$$

and

$$R_\Theta = \frac{I_S}{I_0} \cdot \frac{r^2}{1+\cos^2\Theta} \qquad \textbf{2.4}$$

with K as the optical constant of the apparatus, c the polymer concentration, R_Θ as the so called Rayleigh ratio, which is defined as the relative scattering intensity measured at an angle Θ and a distance r from the scattering center to the detector. M_w is the molecular weight (for a polydisperse polymer: the weight-average molecular weight); A_2 is the second virial coefficient of the osmotic pressure; n is the solvent refractive index; and I_S is the scattering intensity depending on the angle Θ and distance r. To obtain angular independent scattering it is necessary to use polarized light. As lasers emit polarized light no further polarization is required and R_Θ is constant ($1+\cos^2\Theta = 2$) for small particles. After SLS measurements of several different polymer concentrations the extrapolation to zero concentration gives M_w and A_2.[4,5,141,142]

In the cases of macromolecules (diameter $> \lambda/20$) Debye scattering occurs and the scattering intensity is angular dependent. This means that the requirement of isolated, non interacting scattering centers is not fulfilled anymore and intramolecular interferences (constructive and destructive) between various scattering centers in the same polymer particle become important. To describe these internal interferences of the polymer particle the so called particle scattering factor or form factor $P(\Theta)$ is introduced

$$\frac{Kc}{R_\Theta} = \frac{1}{M_w P(\Theta)} + 2A_2c + \dots \qquad \textbf{2.5}$$

with
$$P(\Theta) = \frac{R_\Theta(experimental)}{R_\Theta(without\ interference)}$$
2.6

The form factor, $P(\Theta)$, depends on the wavelength, the size of the macromolecule and is defined as

$$\frac{1}{P(\Theta)} = 1 + \frac{16\pi^2 \langle R_g^2 \rangle}{3\lambda'^2} \sin^2 \frac{\Theta}{2}$$
2.7

with
$$\lambda' = \frac{\lambda}{n}$$

and λ as the wavelength, n as the refractive index of the solvent and $\langle R_g^2 \rangle$ as the square of the averaged radius of gyration. For $\Theta = 0$ the particle scattering factor $P(\Theta)$ has the value of one, for $\Theta > 0$ the value of $P(\Theta)$ gets continuously smaller with increasing Θ. That means that large particles act like small particles, if the condition $\Theta = 0$ is fulfilled.

The size of the molecule can be derived from the angular dependence of the scattered intensity via the so called Zimm-equation. [4,5,141,142]

$$\frac{Kc}{R_\Theta} = \left(\frac{1}{M_w} + 2A_2c \right)\left(1 + \frac{q^2}{3}\langle R_g^2 \rangle_z \right)$$
2.8

with
$$q = \frac{4\pi}{\lambda} \sin\left(\frac{\Theta}{2} \right)$$
2.9

It combines all the experimental variables and molecular parameters of a SLS experiment. The so called Zimm plot (Figure 2.8) can be generated by measuring the scattering intensity of diluted solutions with different concentrations at various angles and plotting of $\frac{Kc}{R_\Theta}$

versus $\sin^2\left(\frac{\Theta}{2} \right) + Kc$. [4,5,141,142]

The Zimm equation shows various molecular parameters that can be determined via different extrapolations.

$c \to 0$ and $\Theta \to 0$
$$\frac{Kc}{R_\Theta} = \frac{1}{M_w}$$
2.10

$c \to 0$
$$\frac{Kc}{R_\Theta} = \frac{1}{M_w}\left(1 + \left(\frac{q^2}{3} \right)\langle R_g^2 \rangle_z \right)$$
2.11

$\Theta \to 0$
$$\frac{Kc}{R_\Theta} = \frac{1}{M_w} + 2A_2$$
2.12
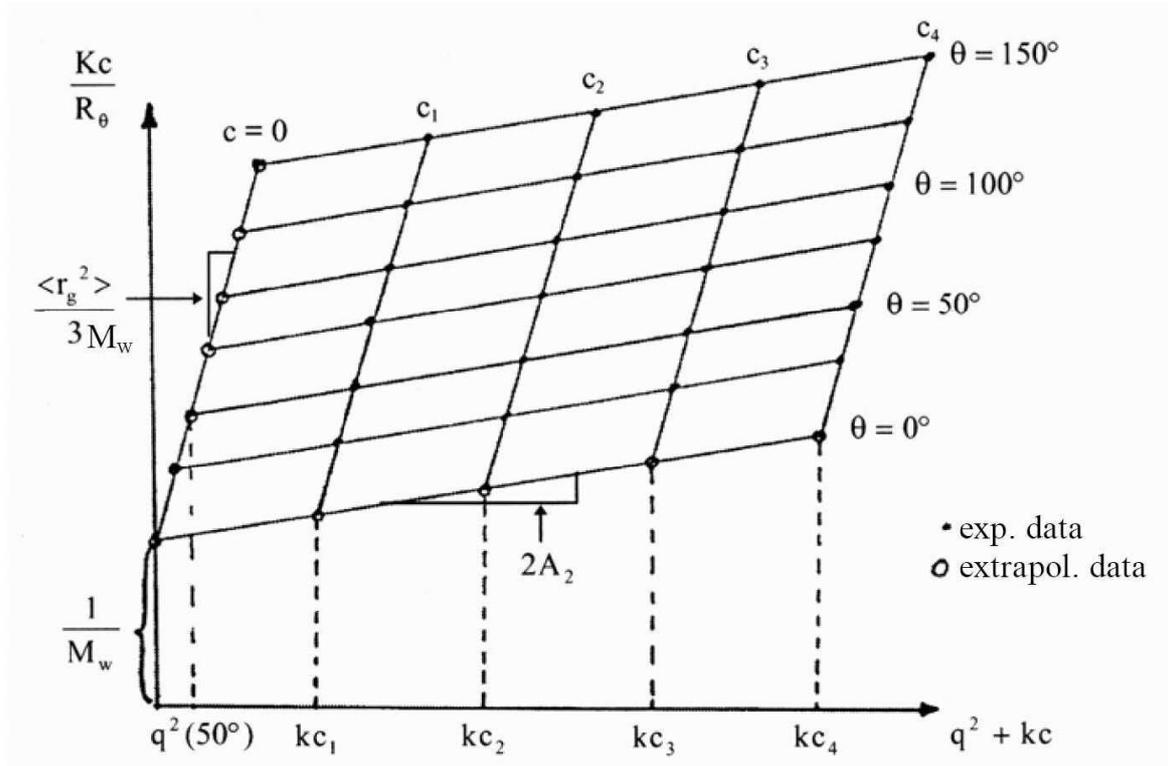
Figure 2.8. Representative Zimm plot.

Some larger aggregates show a moderately curved dependence of $\dfrac{Kc}{R_\Theta}$ on q^2. This leads

to less accurate values through the extrapolation to zero. Berry proposed plotting the square

root of $\dfrac{Kc}{R_\Theta}$ against q and c, respectively, because these plots show less curvature. As a rea-

son for this it was presumed that the contribution of the third virial coeffcient A_3 gets a sig-

nificant influence. Furthermore that the third virial coefficient is related to the second virial

coefficient as $A_3 \propto A_2^2$. So the extrapolation to zero angle leads to

$$\left(\frac{c}{R_\Theta}\right)_{\Theta\to0}^{\!\!1/2} = \left(\frac{1}{M_wK}\right)^{\!1/2}\left(1+M_wA_2c\right)$$ **2.13**

And the extrapolation to zero concentration leads to

$$\left(\frac{c}{R_\Theta}\right)_{c\to0}^{\!\!1/2} = \left(\frac{1}{M_wK}\right)^{\!1/2}\left(1-\frac{8\pi}{3\lambda^2}\left\langle R_g^2\right\rangle_z \sin\!\left(\frac{\Theta}{2}\right)\right)$$ **2.14**

The following table (Table 2.1) shows an overview and comparison of the various pa-

rameters that can be determined from the linear regression of

$$y = a + bx + cx^2$$ **2.15**

according to Zimm and Berry from the measured data.[143]

32

Table 2.1. Coefficients from linear regression used for evaluation of light scattering data according to Zimm and Berry.

	M_w	$\left\langle R_g \right\rangle^2$	A_2
Zimm	$\dfrac{1}{a}$	$\dfrac{3b}{a}$	$\dfrac{b}{2}$
Berry	$\left(\dfrac{1}{a}\right)^2$	$\dfrac{6b}{a}$	ba

The sample preparation of the micelles ($c_{polymer} \sim 0.1$ g/L up to 1.0 g/L) was performed as mentioned above to get a stock solution. The micellar solutions were oversaturated with the solution of silsesquioxane nanoparticles to ensure complete nanohybrid formation. Those micellar or the corresponding nanohybrid stock solutions were dialysed (Serva Electrophoresis GmbH, Servapore: MWCO 12000-14000) against Millipore water with the same salinity and pH as the micellar/nanohybrid solution for 48 h without exchange of the dialysate. This procedure guarantied equilibrium of the micellar or the corresponding nanohybrid solutions with the surrounding solution. The various measured solutions were prepared through dilution of the stock solution with the dialysate followed by an additional stirring time of 12 h. The dialysate was used as the background measurement. The samples were filtered through nylon filters (13-HV, Millipore, 0.45 µm pore size) into cylindrical quartz scattering cuvettes (diameter = 1 cm). The samples were allowed to equilibrate for at least 12 hours after filtering prior to the SLS titration experiments. SLS measurements were carried out on a Sofica goniometer equipped with a He-Ne laser ($\lambda = 632.8$ nm) at room temperature after calibration with filtered toluene. The SLS measurements were performed at angles between 30° and 150° with 5° steps with five measurements per step. Zimm plots were used for the evaluation of the molecular weight, M_w, the radius of gyration, R_g, and the second virial coefficient, A_2.

2.3.2 Dynamic light scattering (DLS)

Dynamic light scattering is a technique to investigate the scattering intensity fluctuation and to obtain size information of the molecules. The basis of DLS is Brownian motion of dissolved molecules. Scattered light undergoes either constructive or destructive interference by the scattered light of surrounding particles, leading to fluctuations in the detected scattering intensity containing information about the time scale of the movement of the light scattering

particles. Dissolved molecules possess the same probability to move in each direction. Furthermore, they have a continuous rate distribution.

The Doppler effect explains frequency changes of the scattered light recorded by the detector depending on the velocity and the moving direction of the scattering molecules. A broadening of the spectrum is observed with respect to the frequency line of the incident light I_0. Therefore, light scattering is rather quasi-elastic than elastic. The spectral broadening is too small to be detected by conventional spectrometers working in the frequency domain. For this reason, measurements are performed in the time domain and fluctuations of the scattered light are measured.

Generally, this is done according to the Homodyn method, i.e. the scattered light is directed to the photon detector. The output signal is proportional to the intensity I(t) of the light and also proportional to the mean square of the electric field $|E(t)|^2$. The output signal of the detector is auto-correlated with time according to[144-146]

$$g_2(t) = \frac{\langle I(0) \cdot I(t) \rangle}{\langle I(0) \rangle^2}$$

2.16

with $g_2(t)$ as the normalized intensity autocorrelation function. The field autocorrelation function, $g_1(t)$, describes the fluctuations of the electric field of the scattered light. It can be obtained from $g_2(t)$ using the Siegert relation[147],

$$g_1(t) = \frac{\langle E(0) \cdot E(t) \rangle}{\langle E(0) \rangle^2} = \sqrt{\frac{g_2(t) - A}{B}}$$

2.17

with A, B usually being equally to unity. A is determined by an experimental baseline, and B is a coherence factor accounting for deviation from the ideal correlation.

In the case of dilute solutions of monodisperse hard spheres, $g_1(t)$ can be described by the exponential function

$$g_1(t) = e^{-\Gamma \cdot t} = e^{-Dq^2 t}$$

2.18

with a decay rate Γ, being directly proportional to the square of the scattering vector, q and the translational diffusion coefficient, D, of the scattering species. The hydrodynamic radius, R_h, can be determined via the Stokes-Einstein equation[144,146,148]

$$R_h = \frac{k_B T}{6\pi\eta D}$$

2.19

with the knowledge of the solvents viscosity, η, the Boltzmann constant, k_B, and the temperature, T, in Kelvin.

Real solutions exist of polydisperse solutions and have to be treated with the following equation

$$g_1(q,t) = \sum_j a_j(q)e^{-\Gamma_j t}$$
2.20

with $a_j(q)$ as the relative amplitudes and

$$a_j(q) = \frac{c_j M_j P_j(q)}{\sum_j c_j M_j P_j(q)}$$
2.21

with M_j as the molecular weight and P_j as the form factor of the particle j. An angular dependence of $g_1(t)$ can be observed for spheres larger than $\lambda/20$ and $P_j(q) < 1$.

Changes from hard spheres to polymer molecules in solution involve rotational diffusion and internal modes in addition to translational diffusion. Rotational diffusion is of particular importance in rod-like molecules, whereas internal modes are significant in large coil-like molecules.[148] From a mathematical point of view, these factors involve additional additive and multiplicative terms. The terms can be eliminated by angle dependent measurements as the amplitudes approach zero for $q^2 > 0$.[144] The determination of the mean diffusion coefficient and standard deviation for polydisperse systems is best accomplished by the CONTIN method developed by S. Provencher.[149] The function $g_1(t)$ is described by a continuous distribution

$$g_1(q,t) = \int_{\Gamma_{min}}^{\Gamma_{max}} G(\Gamma)e^{-\Gamma t}d\Gamma$$
2.22

with $G(\Gamma)$ describing the fluctuation rate distribution function. This equation can be inverted by a Laplace transformation. This inversion is problematic as there are basically an unlimited number of solutions that describe the data within experimental error. In order to minimize these solutions, the CONTIN analysis uses the following regularization

$$R_n(G(\Gamma)) = \int_{\Gamma_{min}}^{\Gamma_{max}} \left(\frac{\delta^n G(\Gamma)}{\delta \Gamma^n} \right) d\Gamma$$
2.23

with n as the order of regularization. Regularization of 0th order represents minimization of the integration area of function $G(\Gamma)$; regularization of 2nd order corresponds to the smoothing of the function $G(\Gamma)$. The original CONTIN routine calculates a rate distribution [$\log(\Gamma)$ scale], whereas the CONTIN routine of the ALV software calculates a time distribution [log(t) scale] that is proportional to the distribution of hydrodynamic radius. The ALV soft-

ware also enables a direct fit of $g_2(t)-1$ via a special algorithm. This usually yields to a smoother distribution function with fewer artefacts as compared to $g_1(t)$

$$g_2(t)-1=\left(\int_{t_{min}}^{t_{max}}e^{-t}G(t)dt\right)^2 \qquad \textbf{2.24}$$

Special care must be exerted on interpreting results to avoid artefacts, especially in the case of a low signal-to-noise ratio, an inappropriate baseline or inappropriate choice of Γ_{max} and Γ_{min}. Thus, the signal-to-noise ratio should always be high. For evaluation of the results, it should be considered that two different distributions can only be distinguished with the CONTIN program if the respective hydrodynamic radii differ from each other by a factor of at least two. The radii or rather diffusion coefficients obtained by the CONTIN method are z-average values. In order to eliminate the influence of form factors for large molecules, the D and R_h values measured at different angles have to be extrapolated to $q^2 > 0$.

Sample preparation for micellar systems

All solutions were filtered three times through nylon syringe filters (13-HV, Millipore, 0.45 µm pore size) prior to the DLS measurements. The filtered solutions were allowed to equili-brate over night. The filtered silsesquioxane nanoparticle solutions were equilibrated at least for 2 hours prior to the measurements. The DLS measurements were conducted in cross-correlation mode using sealed cylindrical scattering cells (d = 10 mm) at five different scatter-ing angles (mostly 30°, 60°, 90°, 120° and 150°) with the use of an ALV DLS/SLS-SP 5022F equipment consisting of an ALV-SP 125 laser goniometer, an ALV 5000/E correlator, and a HeNe laser with the wavelength (λ = 632.8 nm). Measurements were repeated three to five times with an accumulation time between 30 and 300 s. Regularized Laplace inversion (CON-TIN algorithm) was applied to analyze the obtained autocorrelation functions. Apparent hy-drodynamic radii, R_h, were determined using the intensity-weighted distribution of particle sizes and were calculated according to the Stokes-Einstein equation.

Light scattering (LS) titration experiments for micellar systems were performed with the same DLS setup and a computer controlled titrator (Titrando 809, Metrohm). Both instru-ments were synchronized employing home-made software and hardware synchronization (Figure 2.9). Measurements were carried out in home-made glass cells consisting of a cylin-drical scattering cell connected to a three necked reservoir containing the solution, the stirrer (Methrom), the micro-pH-electrode (Metrohm) as well as the titration tube (Methrom) which was immersed in the solution. Sample preparation followed the same protocol as above. Five

DLS and SLS measurements per titration step were performed at an angle of 90° with an accumulation times between 20 and 60 s. The different titration parameters like stirring speed, stirring time as well as the lag time between the stirring period (equilibration period) and the actual LS measurement time were optimized to prevent any kinetic effects. About 20 titration steps with a 30 µL addition volume per addition step were mostly used for one LS titration experiment. The concentration of the titrant (100 g/L silsesquioxane nanoparticles) was high enough to ensure only minor dilution effects of the micellar solution. The dilution was taken into account during the analysis of the data. During each titration step vigorous stirring was performed for 30 s, followed by a lag time of 30 s between the addition step and the DLS measurement of the quiescent solution.
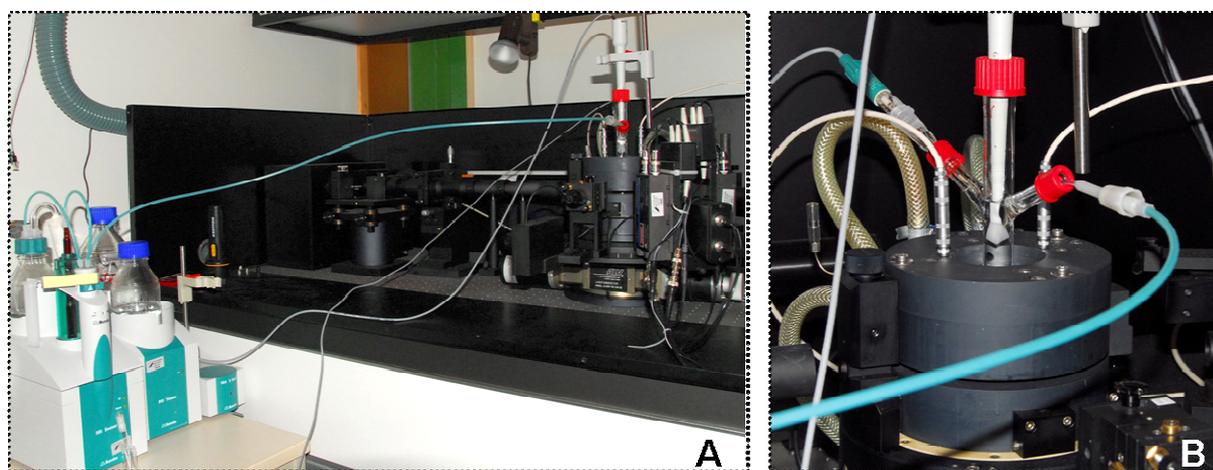
Figure 2.9. Experimental setup for LS titration experiments showing the dosing unit, pH electrode and the stirrer connected to the ALV instrument (A). B shows the specially prepared cuvette for LS titration measurements with lateral inlets for the pH electrode, the burette tip and the stirrer from the top.

Sample preparation for star systems

All solutions were filtered three times through nylon filters (13-HV, Millipore, 0.45 µm pore size) prior to the DLS measurements. The filtered star and the corresponding nanohybrid star solutions were allowed to equilibrate at least for 5 hours. The filtered nanoparticle solutions equilibrated at least for 2 hours prior use. The DLS measurements were conducted in cross-correlation mode using sealed cylindrical scattering cells (d = 10 mm) at five different scattering angles (mostly 30°, 60°, 90°, 120° and 150°) with the use of an ALV DLS/SLS-SP 5022F equipment consisting of an ALV-SP 125 laser goniometer, an ALV 5000/E correlator, and a HeNe laser with the wavelength (λ = 632.8 nm). Measurements were repeated three to five

times with an accumulation time between 30 and 300 s. Regularized Laplace inversion (CON-TIN algorithm) was applied to analyze the obtained autocorrelation functions. Apparent hydrodynamic radii, R_h, were determined using the intensity-weighted distribution of particle sizes and were calculated according to the Stokes-Einstein equation.

Light scattering (LS) titration experiments for star systems were performed with an ALV5000 multiple τ digital correlator and an argon ion laser with a wavelength of 514.5 nm. Titrations were performed using a computer-controlled titration setup (Schott) utilizing a home-made software for synchronising the titrator and the DLS apparatus. LS titration measurements were carried out in home-made glass cells consisting of a cylindrical scattering cell connected to a three necked reservoir containing the solution, the stirrer, the pH-electrode (Mettler Toledo) and the titration tube. Sample preparation followed the same protocol as above. Five DLS measurements per titration step were performed at an angle of 90° with an accumulation times of 30 to 90 s. The different titration parameters like stirring speed, stirring time as well as the lag time between consecutive stirring periods (equilibration period) and DLS measurements were optimized to prevent any kinetic effects. About 65 to 75 titration steps with a 30 µL addition volume per addition step were mostly used for one LS titration experiment. The concentration of the titrant (100 g/L silsesquioxane nanoparticles) was chosen to ensure only minor dilution effects of the polymer solution. However, the dilution was taken into account during the analysis of the data. After addition of nanoparticles the solutions were vigorous stirred for 60 s for each titration step, followed by a lag time of 60 s without stirring to allow subsequent DLS measurements on quiescent solutions.

2.4   Refractive Index Increment (dn/dc)

For evaluation SLS measurements the refractive index increment dn/dc has to be known. It represents the scattering contrast of the solution compared to the particles. The refractive index increment dn/dc can be evaluated by linear fitting of the slope of a plot of the difference of the refractive indices, n, of various solutions with different polymer concentrations to the solvent against, c, of the various polymer solutions. The measurements of the refractive index increment of the polymer solution were performed on a diffraction refractometer DnDC2010/620 (PSS) at $\lambda = 620$ nm.

2.5   Potentiometric Titration

The degree of ionization of weak polyelectrolytes depends directly on the degree of neutralization and therefore on the pH. It is often necessary to know the degree of charging, α', at a certain pH. For the determination of the protonation or deprotonation behavior in dependence on pH one measures the pH of the pure polymer solution in dependence of added strong acid or base. The amount of added acid or base can be put into correlation with the amount of ionisable groups present in the mixture and gives directly the degree of neutralization α. Since we are regarding solutions of weak polyelectrolytes with $pK_{a/b}$ values larger than 4, the self-(de)protonation is only relevant at the outer limits of the titration curve (at the very low or very high pH values). $pK_{a/b}$ is the negative decadic logarithm of equilibrium constant of deprotonation or protonation for acids or bases, respectively. On the other hand the $pK_{a/b}$ values are not larger than 10. Therefore principally complete (de)protonation can be achieved within the standard pH range ($0 < \text{pH} < 14$) by addition of strong base or acid. Thus, the degree of neutralization, α, is identical to the degree of ionization (degree of charging), α', at intermediate degrees of neutralization in very good approximation.

The easiest way to measure the pH is the use of a pH glass electrode being an ion-selective electrode, sensitive to oxonium ions (H_3O^+). It consists of a thin glass membrane, which surface is swollen by water. Protons can be exchanged depending on the pH leading to a change in membrane potential. To compare the potentials, it needs to be measured against a known potential given by a reference electrode. The reference electrode (e.g. AgCl/Ag) can be located in the same electrode (combined electrode), which produces a potential irrespective to the H_3O^+ concentration. It is filled with KCl solution, as KCl generates almost no diffusion potential across the diaphragm of the reference electrode due to similar mobility of potassium and chloride ions.

Potentiometric titrations were performed at room temperature with an automatic titrator (Titrando 806, Metrohm Prozessanalytik) controlled by the Metrohm Tiamo computer software. The used glass electrodes (Unitrode Pt1000 and micro-pH-electrode, Metrohm) were calibrated prior the measurements. Sample preparation followed the description above. The titration curves of the micelles were already published.[46] The measurements of the silsesquioxane nanoparticles were performed form pH 2.5 to 12.5 and from pH 12.5 back to 2.5 with 0.1 M NaCl and 0.1 M HCl, respectively and showed the same behaviour. The equivalence points of the titration were set as the inflection points (maximum of the first derivative).

2.6   Small angle neutron scattering (SANS)

Small angle neutron scattering (SANS) is a very powerful technique to investigate polymer structures in solution and in bulk.[5,150-152] This is based on the fact that neutrons are strongly interacting with atomic nuclei and therefore the scattered wave contains information about the investigated material. A typical setup[153] for SANS experiments is shown in Figure 2.10.
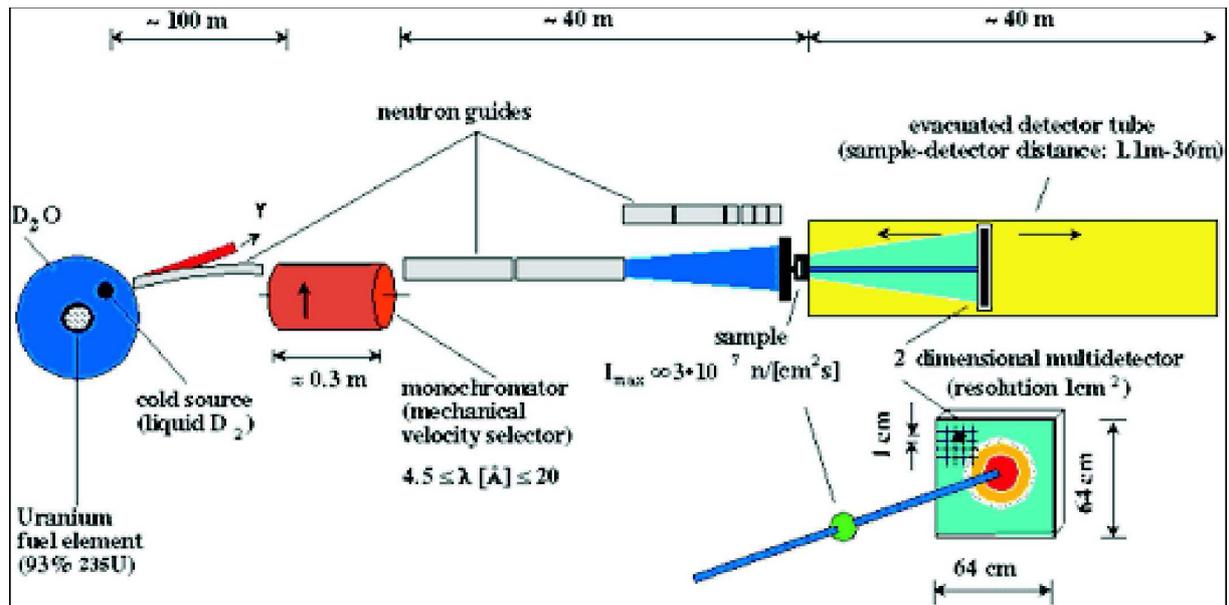
Figure 2.10. Setup of a SANS experiment including neutron source, sample and the detector system.[153]

According to De Broglie neutrons – like each moving particle - can be considered as a wave with a specific wavelength, λ, as well as a particle (particle-wave dualism). This can be expressed by

$$\lambda = \frac{\hbar}{m \cdot c}$$

2.25

with the mass, m, and the velocity, c, of the particle, the wavelength, λ, and the Planck constant, $\hbar$. Due to the particle-wave dualism effects appearing in SANS can be treated analogue comparable effects in X-ray or light scattering. The three different analytical methods differ in their wavelengths and due to that also in the investigated dimensions (Table 2.2).[5,141,150,151]

Table 2.2. Overview of various radiation methods, their wavelength and resolution.

Radiation	Wavelength λ [Å]	Resolution [Å]
Light	$4 \cdot 10^3 - 6 \cdot 10^3$	$\sim 10^3 - 10^5$
Neutrons	1 - 20	$0.5 \cdot 10^3 - 2 \cdot 10^3$
X-rays	1 - 4	$0.5 \cdot 10^2 - 5 \cdot 10^2$

In SANS the differential scattering cross section $\dfrac{d\sum}{d\Omega}$ is the value comparable to the Rayleigh ratio R_Θ from SLS. It is a measure of the number of neutrons scattered per time and space compared to the intensity I_0 of the incident beam. After normalization with the scattering volume, V, a differential scattering cross section independent of the setup is obtained

$$\frac{d\sum}{d\Omega} = \frac{A \cdot I(q)}{V \cdot I_0} \qquad \textbf{2.26}$$

with A being the area of the sample scattering and I_0, the number of neutrons per time. The scattering vector q is defined as

$$q = \frac{4\pi}{\lambda} \cdot \sin\left(\frac{\Theta}{2}\right) \qquad \textbf{2.27}$$

with λ being the wavelength and Θ the scattering angle.

In SANS the contrast of the sample compared to the background (solvent, sample cell, detector dark count) comes from differences in scattering length density, $\bar{\rho}$, of different species in the sample, comparable to the dn/dc value in SLS. When neutrons are scattered by an atom, the scattering length, b_i, is a measure of the scattering power of each sort of atoms. The overall scattering length density, $\bar{\rho}$, can be calculated as

$$\bar{\rho} = \frac{1}{V}\sum b_i \qquad \textbf{2.28}$$

The contrast between sample and background is proportional to the square of the difference in their scattering length density. The differential scattering length density can be calculated as

$$\frac{d\sum}{d\Omega} = N \cdot (\bar{\rho} - \rho_s)^2 \cdot \left\langle V^2 \cdot P(q) \cdot S(q) \right\rangle \qquad \textbf{2.29}$$

with particle density, N, solvent scattering length density, ρ_s, particle volume, V, form factor, $P(q)$ and structure factor, $S(q)$. This is only valid for coherent scattering. As there is

always a certain amount of neutrons scattered incoherently, the scattering intensity contains an isotropic background that has to be subtracted from the measured intensity. The incoherent scattering I_{inc} can be fitted, according to the mentioned fitting model (for micelles: page 42ff. and for stars: page 45ff.).

Evaluations of double logarithmic plots of scattering intensity $I(q)$ against q can be used for fitting the curves according to theory of particles with different shapes. Besides rods, vesicles and spheres many other form factors have already been published in literature.

2.6.1 Sample preparation for SANS experiments

Samples for SANS experiments were prepared in D_2O and measured in 1 mm or 2 mm Hellma quartz cuvettes at room temperature. Measurements were performed using the instrument D11 at the Institut Laue-Langevin (ILL) (Grenoble, France) with a neutron wavelength, λ, between 6 Å and 8 Å and at sample-to-detector distances of 1.1, 4 and 16 m, which corresponds to a scattering vector, q, of $0.003 - 0.34$ Å^{-1}. The detector sensitivity and the intensity of the primary beam were calibrated with a 1 mm reference water sample. The obtained data were radially averaged, corrected for detector background, detector dead time, and the scattering from the empty quartz cuvettes. The relative scattering intensities were converted into absolute units using water as a secondary standard and in accordance with standard routines supplied by ILL. The "GRASP"[154] software package was used for data reduction. SANS data were not corrected for the incoherent background mainly resulting from the solute. DCl and NaOD solutions (Deutero GmbH) were diluted with D_2O (Deutero GmbH) to obtain the required concentration.

2.6.2 Fitting model for SANS data of micellar nanohybrid systems

Fitting of the data was performed with the "SASfit"[155] software package. All SANS data shown were normalized to the concentration of the polymer and given in units of cm^2/g. As the micelles are kinetically frozen the aggregation number of the micelles does not change and the detectable increase of the scattering intensity can be attributed to the incorporation of the silsesquioxane nanoparticle in the micelle. The relative change in the scattering intensity compared to the unloaded micelle can thereby be used to determine the number of nanoparticles per micelle.

The structure of star-like micelles is described in terms of the model of star-like polymers proposed by Daoud and Cotton[156]. Wijmans & Zhulina[157] extended that model to polymer brushes on D-dimensional curved surfaces including the effect of solvents quality. According to that model star-like polymers consist of a homogeneous, dense core surrounded by a stretched polymer layer. As a consequence of the spherical shape, the scattering length density profile, $\eta(r)$, in the polymer layer decreases as

$$\eta(r) = \begin{cases} \eta_{core} & \text{for } r < R_{core} \\ \eta_{sh}\left(\dfrac{r}{R_{core}}\right)^{-\alpha} & \text{for } R_{core} \leq r \leq R_{core} + t \\ 0 & \text{for } r > R_{core} + t \end{cases}$$

2.30

with $\alpha = (D-1)(3\upsilon-1)/(2\upsilon)$. D is determined by the dimension of the curvature of the grafted surface (for spherical particles $D = 3$, for cylindrical ones $D = 2$ and for planar particles $D = 1$). The Flory exponent, ν, has characteristic values depending on the thermodynamic state of the polymer chains. For stretched chains like for polyelectrolytes ν is 1, so that α can be assumed to be 2 for spherical particles ($D = 3$). The corresponding density profile is schematically shown in Figure 2.11. The investigated micelles consist of a well-defined core which is determined by the size of the hydrophobic PnBA block with a fixed radius R_{core}. The corona of the polyelectrolyte micelles extends to the outer micelle radius

$$R_{mic} = R_{core} + t$$

2.31,

where t is the thickness of the corona and R_{mic} is the radius of the whole polyelectrolyte micelle.
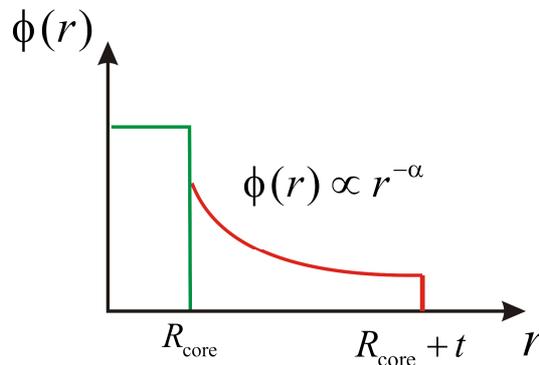
Figure 2.11. Micellar, star-like polymers with a homogeneous core and a corona with decaying density profile with R_{core} as the radius of the homogeneous core formed by the PnBA block of the copolymer and t as the thickness of the PAA corona. For charged polyelectrolytes the exponent α can be assumed to be $\alpha = 2$.

For a known radial profile of the scattering length density, η(r), the SANS form factors of the core and the corona are given by

$$f_{core}(q, R_{core}) = \frac{\int_0^{R_{core}} 2\pi r^2 \, \eta_{core} \frac{\sin(qr)}{qr} dr}{\int_0^{R_{core}} 2\pi r^2 \, \eta_{core} \, dr} = 4\pi \frac{\sin(qR_{core}) - qR_{core}\cos(qR_{core})}{q^3} \qquad \textbf{2.32}$$

$$f_{sh}(q, R_{core}, t) = \frac{\int_{R_{core}}^{R_{core}+t} 2\pi r^2 \, \eta_{sh} \left(\frac{r}{R_{core}}\right)^{-\alpha} \frac{\sin(qr)}{qr} dr}{\int_{R_{core}}^{R_{core}+t} 2\pi r^2 \, \eta_{sh} \left(\frac{r}{R_{core}}\right)^{-\alpha} dr} \qquad \textbf{2.33}$$

The scattering intensity as observed by SANS can be calculated (e.g.[158-161]) by

$$\begin{aligned}
I(q) = I_0 \Big[& N_{agg}^2 \beta_{PnBA}^2 f_{core}^2(q, R_{core}) \\
& + N_{agg}(N_{agg}-1) \beta_{sh}^2 f_{sh}^2(q, R_{core}, t) \\
& + 2N_{agg}^2 \beta_{PnBA} \beta_{sh} f_{core} f_{sh} \\
& + N_{agg} P_{PAA} \Big] \\
& + I_{inc}
\end{aligned} \qquad \textbf{2.34}$$

which contains the following five contributions. These are the contribution from the core of the polyelectrolyte micelle, the shell, a cross-term between core and shell, a contribution from the scattering of the individual PAA chains plus an additional background accounting for the incoherent scattering, I_{inc}.

For the pure micelle the only fitting parameters are the thickness of the shell, t, a scaling factor, I_0 and the micellar aggregation number, N_{agg}, as well as the incoherent background contribution, I_{inc}. As the core is assumed to consist of the PnBA blocks only its radius can be calculated from the aggregation number and the known molecular volume of the PnBA block.

The excess scattering length of the PnBA and PAA blocks are given by

$$\beta_{PnBA} = V_{PnBA}(\eta_{PnBA} - \eta_{solv}) \qquad \textbf{2.35}$$

$$\text{and } \beta_{PAA} = V_{PAA}(\eta_{PAA} - \eta_{solv}), \qquad \textbf{2.36}$$

respectively, with η_{solv} as the scattering length density of the solvent D_2O ($\eta_{solv} = 6.33 \cdot 10^{10} \, cm^{-2}$). The scattering length density η_{PnBA} and η_{PAA} of PnBA and PAA together with their volumes V_{PnBA} and V_{PAA} and their excess scattering length, β, are listed in Table 2.3.

Table 2.3. Used scattering length densities, η_x, the corresponding volumes, V_x, and the calculated excess scattering length, β_x.

x	PnBA$_{90}$	PnBA$_{100}$	PAA$_{100}$	PAA$_{150}$	PAA$_{300}$	nano
$\eta_x\,10^{10}$ [cm^{-2}]	0.58	0.58	1.59	1.59	1.59	0.71
$V_x\,10^{-21}$ [cm^3]	18.34	22.85	10.40	15.59	31.19	4.62
β_x [fm]	10550	13144	4932	7393	14792	2596

For the nanohybrids the excess scattering length of the shell, β_{sh}, increases linearly with the amount of silsesquioxane nanoparticles incorporated in the shell. To account for their scattering contribution - the excess scattering of the shell - is assumed to be

$$\beta_{sh} = \beta_{PAA} + \beta_{nano} = V_{PAA}\left(\eta_{PAA} - \eta_{solv}\right) + x_{nano}V_{nano}\left(\eta_{nano} - \eta_{solv}\right) \qquad \textbf{2.37}$$

where x_{nano} is the average number of silsesquioxane nanoparticles per PAA arm of the micelle, V_{nano} the volume of a single nanoparticle and η_{nano} its scattering length density. It is assumed that the nanoparticles are equally distributed along a PAA chain and therefore contribute in the same way to the radial profile. Equations 3.30 to 3.38 allow to describe the SANS scattering profile.

2.6.3 Fitting model for SANS data of PAA nanohybrid star systems

Fitting of the data was performed with the "SASfit"[155] software package. All SANS data shown were normalized to the concentration of the star polymer and given in units of cm^2/g. As the number of PAA arms per star is fixed the detectable increase of the scattering intensity can be attributed to the incorporation of the silsesquioxane nanoparticle in the star. The relative change in the scattering intensity compared to the unloaded star can thereby be used to determine the number of nanoparticles per star.

The structure of stars is described in terms of the model of a micellar, star-like polymer as proposed by Daoud and Cotton[156] as stars can serve as model systems for micelles. According to this model star-like polymers consist of a homogeneous, dense core - here the macroinitiator residue - surrounded by a stretched polymer layer - here the PAA arms. As a consequence of the spherical shape, the scattering length density profile $\eta(r)$ in the polymer layer decreases according to Wijmans and Zhulina[157] as already shown in equation 4.30. The corresponding density profile is schematically shown in Figure 2.11.

The $(PAA_{100})_{21}$ star consists of a well-defined core which is determined by the size of the cyclodextrin-based initiator with a fixed core radius, R_{core}, of 1.0 nm. The corona of the polyelectrolyte star extends to the outer star radius $R_{star} = R_{core}+t$, where t is the thickness of the corona and R_{star} is the radius of the whole polyelectrolyte star.

For a known radial profile of the scattering length density η(r) the SANS form factors of the core and the corona are given by equations 3.32 and 3.33. The scattering intensity as observed by SANS can then be calculated (see e.g.[158-161]) by

$$
\begin{aligned}
I(q) = I_0 \Big[& \beta_{core}^2 f_{core}^2 (q, R_{core}) \\
& + N_{agg}(N_{agg}-1) \beta_{sh}^2 f_{sh}^2 (q, R_{core}, t) \\
& + 2 N_{agg} \beta_{core} \beta_{sh} f_{core} f_{sh} \\
& + N_{agg} P_{PAA} \Big] \\
& + I_{inc} + Cq^{-4}
\end{aligned}
$$

2.38

which contains the six contributions. These are the contribution from the core of the polyelectrolyte star, the shell, a cross-term between the core and the shell, a contribution from the scattering of the individual PAA chains plus an additional background accounting for the incoherent scattering and finally a q^{-4} background contribution, which was needed to describe the intensity at very small q-values. The excess scattering length of the core was taken equal to that of the nanoparticles. The error introduced by this is low since the contribution of this scattering length is small compared to the other contributions.

For the pure star the only fitting parameters are the thickness, *t*, of the shell and a scaling factor, I_0, as well as the background contribution, $I_{inc}+Cq^{-4}$. The arm number of the star is known to be $N_{agg} = N_{arm} = 21$. The used scattering length densities, $η_x$, the corresponding volumes, V_x, and the calculated excess scattering length, $β_x$ are given in Table 2.3.

For the nanohybrid stars the excess scattering length of the shell increases linearly with the amount of nanoparticles incorporated in the shell. To account for their scattering contribution - the excess scattering of the shell - is given in equation 3.38, where x_{nano} is the average number of silsesquioxane nanoparticles per PAA arm of the star, V_{nano} the volume of a single nanoparticle and $η_{nano}$ its scattering length density. It is assumed that the nanoparticles are equally distributed along a PAA chain and therefore contribute in the same way to the radial profile. Equations 3.30 and 4.38 to 3.41 allow to describe the SANS scattering profile of the organic-inorganic nanohybrid stars.

2.7 Gel permeation chromatography (GPC)

Molecular weight distributions and averages were characterized by conventional GPC and GPC/viscosity using THF as the eluent, at a flow rate of 0.8 to 1.0 mL per min, at room temperature. For all GPC systems precolumns (5 µm, 100 Å, 5 cm • 0.8 cm diameter) are used to protect the separation columns. A conventional THF-phase GPC system was used to obtain the apparent molecular weights. GPC system I: column set: 5 µm PSS SDV gel, 10^2, 10^3, 10^4, 10^5 Å, 30 cm • 0.8 cm diameter each; injection volume 20 µL of a 2 mg per mL solution; detectors: Waters 410 differential refractometer and Waters 996 photodiode array detector. Narrow PS standards (PSS, Mainz) were used for the calibration of column set I. The molecular weight of the star-shaped polymer was determined by the universal calibration principle[162] using the viscosity module of the PSS WinGPC scientific V 6.1 software package on GPC system II. Linear PMMA standards (PSS, Mainz) were used to construct the universal calibration curve. GPC system II: column set: 5 µm PSS SDV gel, 10^3 Å, 10^5 Å and 10^6 Å, 30 cm • 0.8 cm diameter each; detectors: Shodex RI-71 refractive index detector, Jasco Uvidec-100-III UV-detector (λ = 254 nm), Viscotek viscosity detector H502B, which needed to be purged extensively before every measurement and on an Agilent HPLC system (1200 series) with four detectors (UV (260 nm), RI, Viscometer, Model 250 (Viscotek), (Columns: PSS–SDV, 10^6 Å, 5 µm, 10^5 Å, 5 µm, 10^3 Å, 5 µm)). The extracted number average molecular mass M_n was used to determine the degree of polymerization $DP_{n,arm}$ of one arm by dividing M_n by the molar mass of the polymer's repeating unit and, for stars, by the initiation sites per initiator molecule (assuming f_i = 1). The initiator was taken into account. The third setup was an aqueous GPC (internal standard ethylene glycol; additives: 0.1 M NaN_3, 0.01 M NaH_2PO_4), which validated that the PAA stars were intact both before and after the purification steps. Column set: two 8 µm PL Aquagel-OH columns (mixed and 30 Å), operated at 35 °C. Detector: Bischoff RI-Detector 8110.

2.8 Isothermal calorimetric titration (ITC)

Micellar solutions ($c_{polymer}$ ~ 0.2 g/L, 0.1 M NaCl, pH 6) were titrated with a solution of silsesquioxane nanoparticles ($c_{nanoparticle}$ ~ 50.0 g/L, pH 8 to 9) to ensure complete nanohybrid formation during the measurement. All ITC measurements were performed using the VP-ITC (Microcal) instrument. The silsesquioxane solution was filled in the injector. The micellar solution was subsequently filled in the sample cell. Special attention was paid during all steps

to avoid the formation of bubbles in the solutions as they disturb the caloric measurements drastically. The reference cell was filled with degassed water. Prior to the measurement, the system was stirred at 290 rpm and equilibrated at 25 °C. During the measurement, the stirring rate was kept constant. The following parameters were used for the measurement for all samples: number of injections, 150; volume per injection, 2 µl; duration of injection, 4 s; spacing between two injections, 900 s for the first 20 injections then 600 s; filter period, 2 s. Origin 7 SR2 software (OriginLab) was used for all calculations in this study. Background measurements were performed under the same conditions once with Millipore water (0.1 M NaCl, pH 6) and the same silsesquioxane solution and once with the used micellar solution and Millipore water (0.1 M NaCl, pH 9). As the second background measurement did not show any effects it was not used for further calculations.

In principle the investigated system exists of micelles, M, interacting with a high number, a, of silsesquioxane nanoparticles, nano, which can be calculated via this method, and can be denoted as,

$$M + a \cdot nano \; \rightleftharpoons \; M(nano)_a \qquad\qquad \textbf{2.39}$$
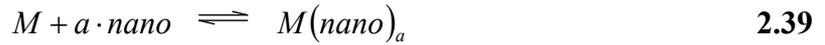
In a calorimetric experiment the heat, q, that is evolved or absorbed for each injection step is proportional to the change in concentration of bound nanoparticles, $\Delta[nano]_{bound}$,

$$q = V_0 \cdot \Delta H^0 \cdot \Delta[nano]_{bound} \qquad\qquad \textbf{2.40}$$

where V_0 is the active cell volume, and ΔH^0 the apparent enthalpy of binding. ΔH^0 is an apparent value as the binding reaction may be accompanied by many linked equilibria yielding heat changes.

As the system has just one kind of interaction sites on the polyelectrolyte side the model of a "single set with identical sites"[163,164] can be used for the calculation of the cumulative heat, Q, which can be expressed by,

$$Q = \frac{a[M]\Delta H^0 V_0}{2}\left[1 + \frac{[nano]}{a[M]} + \frac{1}{aK[M]} - \sqrt{\left(1 + \frac{[nano]}{a[M]} + \frac{1}{aK[M]}\right)^2 - \frac{4[nano]}{a[M]}}\right] \qquad \textbf{2.41}$$

with K as the binding constant, a as the number of sites, $[M]$ as the total concentration of the micelle in V_0 and $[nano]$ as the total concentration of the nanoparticle in V_0. Equation (2.41) is subsequently fitted. Additionally, the dilution is taken into account. The free energy ΔG^0 is known through

$$\Delta G^0 = \Delta H^0 - T\Delta S^0 = -RT \ln K \qquad\qquad \textbf{2.42}$$

where ΔS^0 is the entropy of the binding and T the temperature. Fitting of equation 2.41 to the data provides the values ΔH^0 and K_a. ΔS^0 can be calculated from these values. The error of ΔS^0 is calculated via the law of error propagation.

2.9   *Cryogenic transmission electron microscopy (cryo-TEM)*

Cryogenic transmission electron microscopy (cryo-TEM) measurements were performed on a Zeiss EM922 EF-TEM (Zeiss NTS GmbH, Oberkochen, Germany) at temperatures around 90 K. The TEM was operated at an acceleration voltage of 200 kV. Zero-loss filtered images ($\Delta E = 0$ eV) were taken under reduced dose conditions (approx. $100 - 1000$ e/nm^2). All images were recorded digitally by a bottom mounted CCD camera system (Ultrascan 1000, Gatan) combined and processed with a digital imaging processing system (Digital Micrograph 3.10 for GMS 1.5, Gatan). To prepare the sample one drop of the aqueous solution was put on a hydrophilized (home-made equipment, Biozentrum Basel) lacey carbon-coated copper grid (Plano GmbH, Wetzlar, Germany), where most of the liquid was removed with blotting paper leaving a thin film stretched over the lacey holes. The specimens were instantly shock vitrified by rapid immersion into liquid ethane cooled at ~90 K by liquid nitrogen in a temperature-controlled freezing unit (Zeiss Cryobox, Zeiss NTS GmbH, Oberkochen, Germany). The temperature was monitored and kept constant in the chamber during the whole sample preparation steps. After freezing a specimen, remaining ethane was removed using blotting paper. The specimen was inserted into a cryo-transfer holder (CT3500, Gatan, München, Germany) and transferred to the TEM instrument. Examinations were carried out at ~90 K. Cryo-TEM micrographs of the pure stars can not be obtained due to the bad signal to noise ratio.

For evaluation of the data the open source programme ImageJ[165] was used. For normalized averaged radially integrated grey-scale analysis (in the following denoted as "grey-scale analysis") the plugins "Radial Profile" and "Radial Profile Extended" were used. Single micelles or the corresponding organic-inorganic nanohybrids of the cryo-TEM micrographs were radially integrated using a radius that is slightly larger than the by DLS measurements known hydrodynamic radius but still ensures the investigation of a single particle. The integration was done with the mentioned plugins. The data for each radially integrated particle in one cryo-TEM micrograph were exported and averaged followed by intensity normalization. The averaged radially integrated grey-scale analyis of each cryo-TEM micrograph were averaged. The measurements of the core-core distance and the grey-scale analysis was performed

on various cryo-TEM micrographs with the same magnification over 80 to 150 micelles or the corresponding nanohybrids to ensure good statistics.

2.10   Thermogravimetric analysis (TGA)

Thermogravimetrical analysis (TGA) was performed on a Mettler TGA/SDTA 85 InterCooler within the temperature interval from 30 – 1000 °C with a heating rate of 2 °C / min under air flow. The final temperature was kept constant for additional 2 hours to ensure complete removal of all organic material. The aqueous samples were prepared according to the above mentioned sample preparation. The nanohybrid solutions were dialyzed (Serva Electrophoresis GmbH, Servapore: MWCO 12000-14000) for two weeks with seven time removal of the dialysate against Millipore water with the same salinity and pH value as the nanohybrid solution to ensure complete removal of all excess free silsesquioxane nanoparticles. The aqueous samples were freeze-dried and additionally dried in vacuum to give a white powder residue.

2.11   Fourier-transform infrared spectroscopy (FT-IR)

The aqueous samples were prepared according to the above mentioned sample preparation. The nanohybrid solutions were dialyzed (Serva Electrophoresis GmbH, Servapore: MWCO 12000-14000) for two weeks with seven time removal of the dialysate against Millipore water with the same salinity and pH value as the nanohybrid solution to ensure complete removal of all excess free silsesquioxane nanoparticles. The aqueous samples were freeze-dried and additionally dried by oil pump vacuum. The obtained white powder residue was mixed with KBr and measured as a KBr-pellet on a Bruker EQUINOX 55/S infrared spectrometer.

2.12   Asymmetric flow field-flow fractionation (AFFFF)

In field-flow fractionation (FFF), a solution of the sample is introduced into a stream of solvent that flows through a ribbonlike channel. An external field is applied perpendicular to the flow, which interacts with the solute, forcing it toward the channel wall. The combination of the effect of the field, giving rise to a concentration gradient, and diffusion, which causes a

concentration gradient to relax, results in a steady-state layer of solute against the wall, within which the distribution of solute is usually exponential,

$$c = c_0 e^{-\frac{x}{l}}$$
                                                                                    2.43

where c is the concentration of solute at a distance x from the wall, c_0 is the concentration at the wall, and l represents the mean thickness of the layer.[68]

For a given solute species, l depends on the velocity, U, with which solute molecules move toward the wall as a result of the applied field and on the diffusion coefficient, D, for the solute species ($l = \dfrac{D}{U}$). In general, smaller species, which have higher diffusion coefficients, form thicker steady-state layers. The flow profile within a thin channel is parabolic, the fluid velocity being greatest near the centre of the channel. Solute species possessing steady-state layers that extend furthest into the faster flowing regions are swept out of the channel first, followed by those species that are more tightly compressed into the slower flowing regions near the wall. Because separation in FFF is dependent on D, the effect of charge on D needs to be taken into account when analyzing polyelectrolytes by FFF methods.[68]

Usually smaller solute species emerge first from an FFF channel, but on going to very large particle sizes, the elution order may be reversed. This is a steric effect arising from the physical bulk of the particle, which limits how closely its centre of mass can approach the wall what is sometimes referred to as steric FFF.[68]

Asymmetric flow field-flow fractionation (AFFFF) applies an asymmetric flow field to the channel. AFFFF with just one permeable wall offers a faster and more efficient separation compared to a symmetric channel with two permeable walls. AFFFF measurements of the micellar and nanohybrid solutions ($c_{polymer} \sim 0.1$ g/L) were performed on a flow-FFF system, Eclipse 2 Separation system (Wyatt Technology, USA) equipped with an autosampler, a degasser and a programmable pump, Isocratic 1200 (Agilent Technologies) and flow channel equipped with a 30 kDa regenerated cellulose membrane and 490 μm thickness spacer (Wyatt Technology, USA). Online detection used multiangle light scattering (Dawn EOS, Wyatt Technology, $\lambda = 690$ nm), UV-VIS spectroscopy ($\lambda = 280$ nm, Postnova Analytics GmbH, Germany) and a refractive index meter (Shodex RI-101). Astra Software 4.90.08 (Wyatt Technology, USA) was used to collect the MALS, UV-VIS absorbance and RI detector signals. Absolute scattering intensity was calculated based on Rayleigh scattering from toluene, and the MALS detectors sensitivities at various angles were calibrated using pure HPLC grade toluene (Merck), and normalized using an aqueous solution of dextran ($M_w = 65000$,

$\left\langle R_g^2 \right\rangle^{1/2}$ = 7 nm). An aqueous solution with the same pH and salt content as the sample was used as eluent at room temperature. The flow profile was 1 min of an initial focusing step, 100 µL sample injection into the flow channel over 2 min, followed by a sample focusing step of 2 min. A volumetric channel flow rate was set at 0.50 or 0.70 mL/min, and a constant cross-flow rate was set at 0.15 or 0.20 mL/min for 60 or 90 minutes. The collected data were processed with the Astra for Windows software version 4.90.08 (Wyatt Technology, USA) using a Zimm fit with fitting degree of one. The number-average, weight-average, and z-average particle radius, R_n, R_w, and R_z, respectively, were derived from the corresponding root-mean-square radii of gyration. The polydispersity was determined as follows: PDI = M_w/M_n. According to the small size of the silsesquioxane nanoparticles excess of them did not disturb the measurements of the nanohybrids, which where prepared as with silsesquioxane nanoparticle oversaturated micellar solutions to ensure complete nanohybrid formation.

3 Smart organic-inorganic nanohybrids based on amphiphilic block copolymer micelles and functional silsesquioxane nanoparticles

Micelles of the amphiphilic block copolymer $PnBA_x$-b-PAA_y (with x = 90, 100 and y = 100, 150, 300) are directly formed by dissolving the polymer in Millipore water containing 1.1 equivalents of NaOH with respect to the carboxylic functions of the PAA block. Subsequent addition of NaCl leads to monodisperse spherical micelles with well-defined size at pH 9 as reported by Colombani et al.[45,46] The pH of the micellar solution can be tuned through addition of HCl solution.

The silsesquioxane nanoparticles are highly functionalized with ca. 14.2 tertiary amines per particles, each amino group bearing four hydroxyl groups. They are easily soluble in water and methanol. The diameter of the silsesquioxane nanoparticles (d ≈ 3 nm)[112,122] in aqueous solutions is rather small compared to the size of the micelles (d = 60 to 116 nm at pH 7). For the formation of organic-inorganic nanohybrids micellar solutions were simply mixed at room temperature with an aqueous solution of silsesquioxane nanoparticles possessing the same salinity as the micellar solution. The pH of the formed organic-inorganic nanohybrids was changed via the addition of HCl solution.

The effect of pH and salinity on the system should be investigated as both can play an important role in the nature of the interaction between the nanoparticles and the micelles. This interaction can be due to Coulombic attraction of the negatively charged poly(acrylic acid) (pK_a = 5.5 to 5.7 for the micellar corona at 0.1 M NaCl)[46] at pH ≥ 6 and the partially positively charged amino function of the nanoparticles (pK_a = 7.6 ± 0.2). As seen from Figure 3.1, the strongest overlap of the potentiometric titration curves is in the pH region from 5.6 to 7.4. Furthermore, the protonated acid functions of the polyelectrolyte micelle can interact with the amino functions of the nanoparticles at low pH by protonating the amino groups. The hydroxyl functions of the nanoparticles can form hydrogen bonds to the protonated COOH functions of poly(acrylic acid).

Those various interactions may lead to different morphologies of the formed organic-inorganic nanohybrids. The nanoparticles may act as possible crosslinkers between various micelles. This could lead to the formation of either rather small, defined aggregates of micelles or even large, undefined aggregates. Changes in salinity or pH may induce transformations between both aggregate types. Alternatively, interaction of the nanoparticles with the

PAA shell inside the micelle may lead to defined, individual organic-inorganic nanohybrids within the micellar dimensions. Due to screening of the charges of the PAA corona the micelle may contract. On the other side the introduction of a high amount of nanoparticles may also induce an expansion due to additionally required space for the nanoparticles. Furthermore pH and salinity may influence this system significantly, as it is well-known for IPECs[89-92,136,137] of weak polyelectrolyte micelles and strong oppositely charged polyelectrolytes.
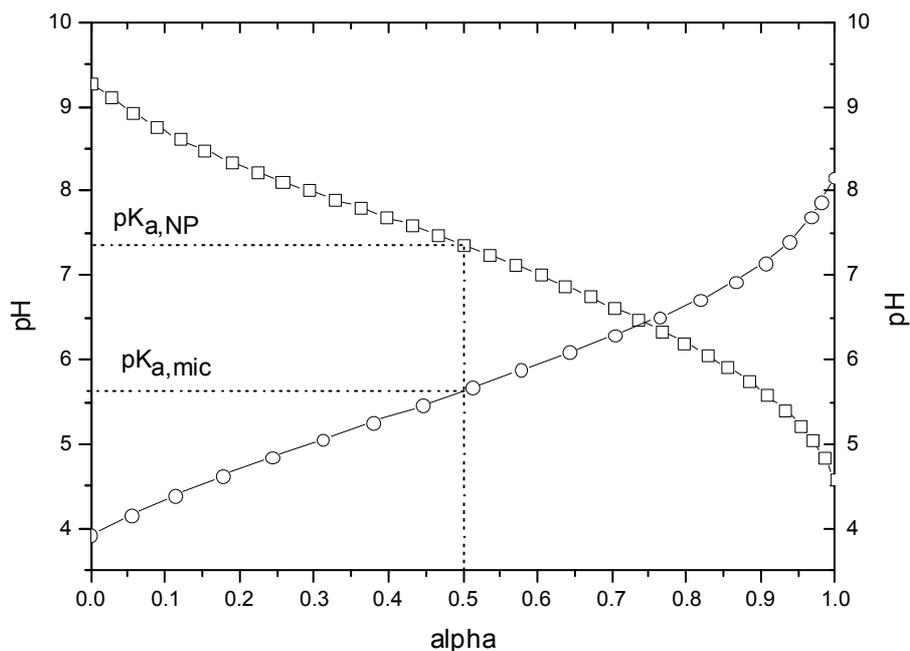

Figure 3.1. Potentiometric titration curves of silsesquioxane nanoparticles (-□-) and PnBA$_{90}$-b-PAA$_{300}$ micelles[46] in presence of 0.1 M NaCl (-○-).

3.1   Dynamic light scattering experiments

DLS measurements (Table 3.1) provide a first insight into the system. LS titration measurements (Figure 3.2) show systematic changes within the micellar system during the addition of nanoparticles. For LS titrations the solutions of micelles were titrated with a solution of the nanoparticles using online pH monitoring combined with DLS and SLS measurements that are performed and recorded after each titration step and a subsequent stirring and waiting time. The titrations were performed up to a very high ratio of silsesquioxane nanoparticles per acrylic acid units of the block copolymer, r = [n(nanoparticles)/n(AA)], to ensure oversaturation, which may provoke crosslinking of micelles. As the behaviour of the PnBA$_{90}$-b-PAA$_{300}$ micelles is representative for all investigated system (Table 3.1) this system is discussed in detail.

Table 3.1. Hydrodynamic radii obtained by DLS for different micellar systems ($c_{polymer}$ = 0.1 to 0.2 g/L) at pH 9 before addition of silsesquioxane nanoparticles and at a final ratio r = [n(nanoparticles)/n(AA)] and experimental ratios based on the increase in scattering intensity.

	c_{NaCl} [mol/L]	R_h [nm] micelle	r_{stoich}[a]	R_h [nm] hybrid	$\frac{I_{max}}{I_{micelle}}$	r_{LS}[b]
P*n*BA$_{90}$-*b*-PAA$_{300}$	0.1	50 ± 2	0.76	50 ± 2	2.07[c]	0.06[c]
		50 ± 2	4.63	50 ± 2	4.95	0.18
	0.01	58 ± 2	0.81	58 ± 2	6.36[c]	0.25[c]
		58 ± 2	5.74	58 ± 2	10.1	0.49
P*n*BA$_{100}$-*b*-PAA$_{150}$	0.1	51 ± 3	8.52	57 ± 3	3.97	0.14
	0.02	50 ± 1	10.1	49 ± 3	8.04	0.42
P*n*BA$_{90}$-*b*-PAA$_{100}$	0.1	30 ± 2	9.61	34 ± 1	4.95	0.35
	0.02	30 ± 2	9.30	33 ± 1	4.98	0.43

[a] stoichiometric ratio in the solution, [b] experimental determined ratio inside the nanohybrid by LS titration, [c] obtained with more efficient stirring

For the P*n*BA$_{90}$-*b*-PAA$_{300}$ block copolymer the CONTIN analysis of the DLS data of each titration step shows a constant hydrodynamic radius of 50 ± 2 nm in the case of 0.1 M NaCl (Table 3.1) for both the micelles and the corresponding nanohybrids and 58 ± 2 nm in the case of 0.01 M NaCl (Table 3.1). This is in very good agreement with the reported size of the aggregates of pure P*n*BA$_{90}$-*b*-PAA$_{300}$ at the same conditions: R_h = 51 nm at pH ~ 10-11 with 0.1 M NaCl and R_h = 61 nm at pH ~ 10-11 with 0.01 M NaCl.[45] It proves the absence of crosslinking of various micelles. Similar results are obtained for the other block copolymers. The dependence of the hydrodynamic radii on the salt concentration is due to the well-known salt effect. According to that, the electrostatic repulsion of highly charged polyelectrolytes is screened in the presence of salt, leading to a reduced chain stretching.[27,28,34,36] Since no effect of the silsesquioxane nanoparticles on the hydrodynamic radius of the micelles is observed one might argue that there is no interaction at all. For that reason we analyzed the scattering intensities during the titrations.

3.2   Light scattering titration experiments

The LS titrations depicted in Figure 3.2 show a marked effect of silsesquioxane addition on the scattering intensities, measured as the count rates at 90°. The pH increase in all titrations

is due to the silsesquioxane nanoparticle solution having an intrinsic pH of 8 to 9. The micellar solution was not buffered to eliminate any influence of additional components. To exclude that the observed changes in scattering intensities are due to the pH increase, titration with NaOH solution was performed to reach the same final pH. These LS titrations showed no changes in the count rate with increasing pH. All LS titrations of the micellar solution with a starting pH of around 6 show a dramatic increase in the scattering intensity by a factor of ~2 (c_{NaCl} = 0.1) to ~10 (c_{NaCl} = 0.01) (Table 3.1).
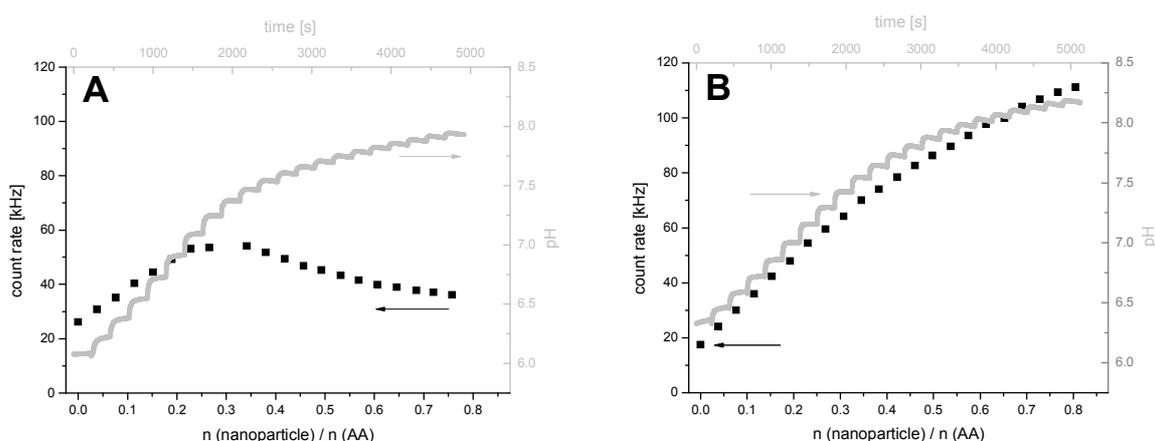

Figure 3.2. Light scattering intensities (squares) and pH values (lines) during titration of PnBA$_{90}$-b-PAA$_{300}$ micelles ($c_{polymer}$ = 0.184 g/L) with silsesquioxane nanoparticles (c_{nano} = 100 g/L), A: c_{NaCl} = 0.1 M starting pH = 6.08; B: c_{NaCl} = 0.01 M, starting pH 6.33).

As the count rate depends on the weight concentration, c, and the molecular weight, M_w, of the scattering particles, the refractive index increment, dn/dc, and an equipment-specific constant, K', this increase is a strong indication for the formation of particles with higher molecular weight, i.e. interaction of the micelles with silsesquioxane nanoparticles.

$$I = K' \cdot c \cdot M_w \cdot \left(\frac{dn}{dc}\right)^2 \qquad \textbf{3.1}$$

This is true as long as dn/dc of the nanohybrids does not increase significantly and the pure silsesquioxane nanoparticles do not have any significant contribution to the scattering intensity of the solution. The silsesquioxane nanoparticles possess a refractive index increment, dn/dc = 0.150 mL/g without added salt and of 0.151 mL/g for the solutions with 0.1 M NaCl. Furthermore almost no scattering signal of the pure silsesquioxane nanoparticles in solution can be detected due to their low molecular weight (M_w = 3760 g/mol). The concentration of the micelles depending on the experiment decreases by 4.8 … 19.4 % of the original

value due to dilution during titration. This was taken into account for all calculations. The dn/dc values for the $PnBA_x$-b-PAA_y micelles are in the range of 0.167 mL/g ($PnBA_{90}$-b-PAA_{100}) to 0.192 mL/g ($PnBA_{90}$-b-PAA_{300}) at pH = 7[45], which is significantly higher than that of the silsesquioxane nanoparticles. In conclusion, the increased count rate can be only due to an increased molecular weight of the scattering species, indicating the formation of real complexes.

A first semi-quantitative analysis of the amount of silsesquioxane nanoparticles within the nanohybrid (r_{LS} = [n(nanoparticles)/n(AA)]) can be performed using the LS titration results. Knowledge of the molecular weight of the pure micelle, the starting concentration, the refractive index increment, and the measured count rate, I, of the pure the micelle solution enables the determination of the equipment-specific constant, K', from equation 3.1. Using the same equation with dn/dc, the concentration and the measured count rate, of the nanohybrid, its molecular weight can be estimated. The difference of the molecular weights of the nanohybrid and the micelle, divided by the molecular weight of the nanoparticles renders the amount of nanoparticles within the nanohybrid,

$$n_{NP,\exp} = \left(M_{hybrid} - M_{micelle} \right) / M_{NP}.$$ **3.2**

The maximum of the observed intensities was used for the calculation. The corresponding experimental ratios, $r_{\exp}$, are given in Table 3.1. The salt dependence of the system can be clearly observed. All values for 0.01 M and 0.02 M NaCl are significantly higher than the ones for 0.1 M NaCl content. Furthermore, the quantitative analysis points to an equilibrium system. The more silsesquioxane nanoparticles are within the solution the more can be accumulated within the nanohybrid. The determined $r_{\exp}$ values are significantly lower than the stoichiometric ones, r_{stoich}.

The micellar system with a salt content of 0.1 M NaCl (Figure 3.2A) shows an increase of the count rate with each titration step until a maximum is reached. After that the count rate drops constantly. The final value of the count rate is higher by a factor of 1.55 ± 0.15 compared to that of the pure the micelles. As the decrease of the count rate after the maximum is always at a pH of 7.5 the explanation for this observation is that the interaction between the nanoparticles and PAA is the strongest at pH < 7.5 and the largest number of silsesquioxane nanoparticles is interacting with the PAA corona. With a further increase of the pH the interaction is getting weaker, and as a result less silsesquioxane nanoparticles can interact with the micelle at high pH indicated by the decreasing scattering intensity resulting in nanohybrids with a lower mass. This is in agreement with the observation that micellar solutions with a starting pH > 8 do not show any significant increase in the count rate.

The micellar system with low salt content (0.01 M NaCl, Figure 3.2B) shows a much stronger increase of the count rate, reaching a plateau at about ten times the initial value but not showing a maximum. Throughout the LS titration the scattering intensity is higher than for the case of high ionic strength. As will be shown later, dialysis experiments of the nanohybrids with fluorescently-labelled silsesquioxane nanoparticles give a similar trend (page 61ff.). The charges of the polyelectrolyte system with low salt content are less screened, as can be seen in the larger hydrodynamic radius of this system compared to the micelles and nanohybrids containing 0.1 M NaCl (Table 3.1). As a result the driving force to entrap silsesquioxane nanoparticles into the PnBA$_{90}$-b-PAA$_{300}$ micelle is stronger at low ionic strength, leading to nanohybrids with a larger number of interacting nanoparticles and consequently to a higher molecular weight. A decrease of turbidity was also reported by Mori et al.[112,113] for the interaction of nanoparticles with linear PAA and increasing salt concentration and confirms the well-known fact that the stability of IPECs decreases with increasing salinity.[89-92,136,137] It indicates that ionic interactions play a significant role in the complexation process.

As already mentioned, micellar solutions with a starting pH > 8 do not show a significant change in count rate during the LS titration measurement. This implies that the pH of the system strongly influences the interaction between the nanoparticles and the PAA corona of the micelles. At high starting pH of the micellar solution the interaction is weaker than at lower starting pH. This is pointing out that the degree of ionization of the PAA block is a key factor for an effective interaction with the nanoparticles and that hydrogen bonding also plays an important role.[112,113] Thus, this observation opens the possibility to form pH-tunable organic-inorganic nanohybrids.

The size invariance of the pure micelles and the corresponding nanohybrids for all investigated micellar systems (Table 3.1) over a wide pH range (pH 6 to 9) is known for this micellar system.[45] As the micelles are kinetically frozen the core cannot undergo any structural size changes. The incorporation of the silsesquioxane nanoparticles into the micelles has no effect on the charge repulsion of the PAA chains in the corona. The hydrodynamic radius of block copolymer micelles is mainly determined by the extension of the charged corona, which is rather collapsed at high ionic strength, but extended at low salinity. An uptake of nanoparticles at high ionic strength may cause an extension of the corona due to steric constraints. However, attractive interactions between corona and nanoparticles may counterbalance any significant extension of the corona. Moreover, the concentration of nanoparticles trapped in the micellar corona is expected to be low at high salinity. At low ionic strength, the corona is in its most extended state. The incorporation of nanoparticles may screen the repul-

sive interactions between the polymer chains, leading to a less extended corona. This is likely to be counterbalanced by increased steric repulsion through nanoparticle uptake. Hence, we do not expect any impact of nanoparticle-micelle complexation on the geometric size of the particles, which is mainly determined by the original micelle. The size conservation is not only evident by DLS but is also sustained by cryogenic transmission electron microscopy (cryo-TEM; page 59ff.) measurements, which provide a direct insight into the micellar system and the corresponding nanohybrids.

3.3   Cryogenic transmission electron microscopy experiments

Typical cryo-TEM micrographs of the $PnBA_{90}$-b-PAA_{300} micelles and the corresponding nanohybrids are shown in Figure 3.3. Caesium ions were added as staining agent for the PAA corona. The samples possess the same block copolymer concentration, salinity, caesium content, and pH.

The micellar structure of $PnBA_{90}$-b-PAA_{300} is clearly demonstrated in Figure 3.3A, as well as the relatively uniform size distribution of the micelles. The micrograph shows the dark $PnBA$ core with a diameter of ~20 nm, having a high segment density leading to a high contrast. The corona is hardly visible although the sample was stained with caesium ions to enhance the contrast. As the micelles are quite closely packed, the shell of two neighbouring micelles may partially overlap. Nevertheless, the core-to-core distance of two neighbouring micelles with 114 ± 14 nm is a good approximation for the diameter of a single micelle, leading to a radius of 57 ± 7 nm for the $PnBA_{90}$-b-PAA_{300} micelle, which is in good agreement with the observed hydrodynamic radius of 50 ± 2 nm by DLS measurements (Table 3.1). The grey-scale analysis of the cryo-TEM micrograph (Figure 3.3C) shows that the core-corona interphase is very sharp. In this analysis high intensity values correspond to low contrast, i.e., the lighter parts. Thus, the part with an intensity value of 0.0 in the grey-scale analysis corresponds to the $PnBA$ core of the micelle as the data were normalized to be zero for the micellar core. The radius of the micellar core is determined from Figure 3.3C as 10 ± 1 nm. In the subsequent interphase region the intensity values rapidly increase, representing the decreasing density of the corona. At 34 ± 1 nm (90% of the normalized grey-scale, corresponding to 2/3 of the hydrodynamic radius) the density profile flattens.
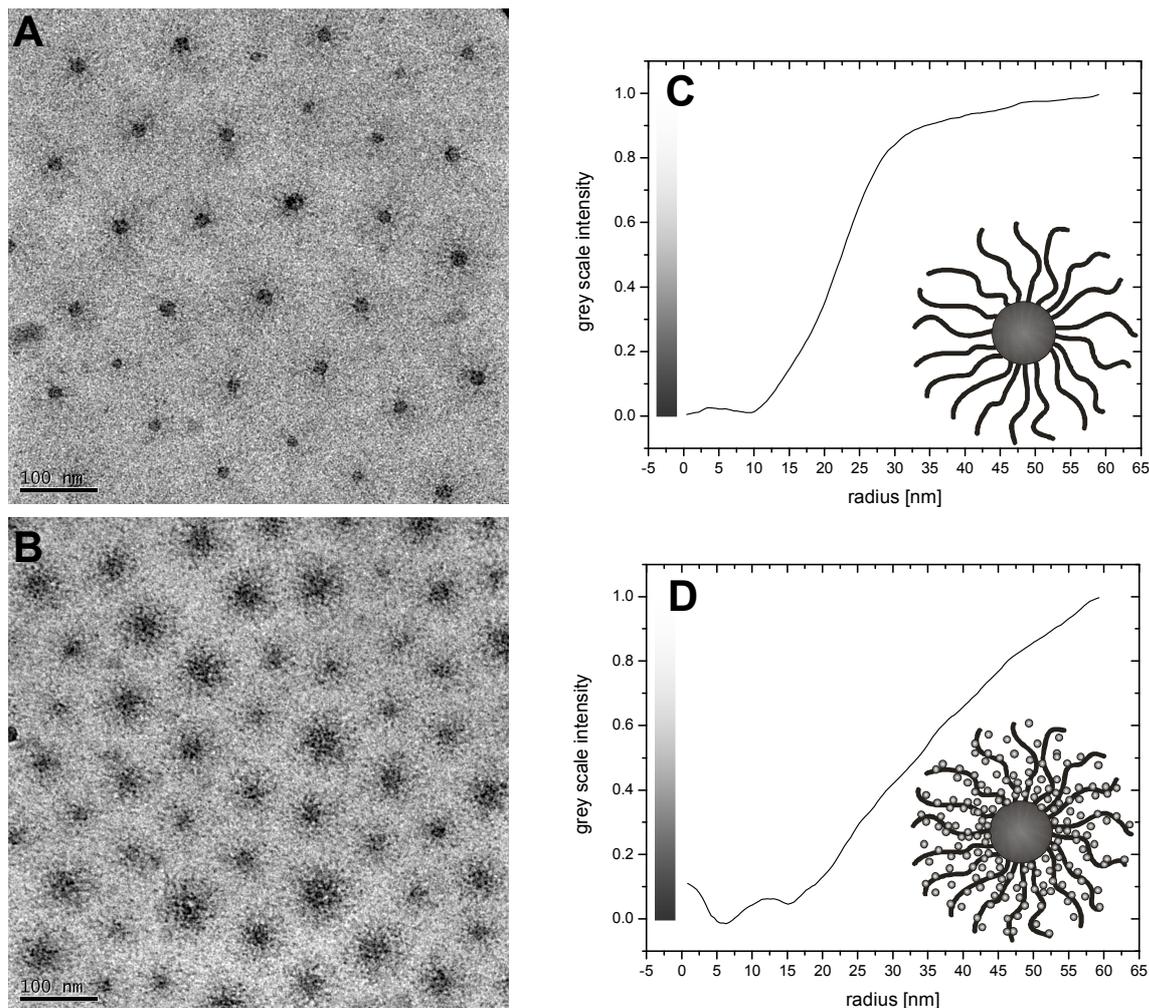
Figure 3.3. Cryo-TEM micrographs of PnBA$_{90}$-b-PAA$_{300}$ micelles and nanohybrids after staining of the PAA corona with caesium ions at pH 7 and 0.1 M NaCl. $c_{polymer}$ = 5 g/L; A: pure micelles, B: $c_{polymer}$ = 5 g/L and nanoparticles at c_{NP} = 5 g/L (size bar: 100 nm) and the corresponding intensity-normalized, averaged radially integrated grey-scale analysis (C and D).

The modified structure of the organic-inorganic nanohybrid can be clearly observed in (Figure 3.3B,D). The micrographs prove that the sizes of the nanohybrids are equal to those of the pure amphiphilic micelles. The grey-scale analysis shows that the core-corona interphase is less sharp than for the pure micelles. The radius of the dark region is significantly increased to 15 ± 1 nm, indicating that it corresponds not only to the PnBA core but also to a dense shell of PAA strongly interacting with the nanoparticles. After this region a slow increase of the normalized intensity to 53 ± 1 nm follows, indicating a less densely packed layer of the PAA corona interacting with the nanoparticles. The core-to-core distance of the organic-inorganic nanohybrid is with 102 ± 16 nm slightly smaller than the corresponding value of the pure mi-

celles (114 ± 14 nm). As the core-to-core distance is a relatively good estimate for the radius of the particles, this evaluation indicates that the nanohybrids possess a comparable radius (51 ± 8 nm) as the corresponding micelles (57 ± 7 nm) according to cryo-TEM. The size of the original micelles is conserved taking the error of the measurement and of the evaluation into account.

Table 3.2. Comparison of the dimensions of the micellar systems at pH 6 - 7 and 0.1 M NaCl for the cryo-TEM analysis and at pH 9 and 0.1 M NaCl for the DLS experiments.

		R_h (DLS) [nm] pH 9	R (cryo-TEM) [a] [nm] pH 6 - 7	R_{core} [nm] pH 6 - 7
$PnBA_{90}$-b-PAA_{300}	micelle	50 ± 2	57 ± 7	10 ± 1
	hybrid	50 ± 2	51 ± 8	15 ± 1
$PnBA_{100}$-b-PAA_{150}	micelle	51 ± 3 [b]	20 ± 4	8 ± 1
	hybrid	57 ± 3 [b]	25 ± 4	18 ± 1
$PnBA_{90}$-b-PAA_{100}	micelle	30 ± 2	25 ± 5	11 ± 1
	hybrid	34 ± 1	24 ± 4	18 ± 1

[a] half the core-to-core-distance, [b] hints for cluster formation

The grey-scale analysis of the nanohybrids in comparison to the pure micelles points to a core-shell model for the organic-inorganic nanohybrid (Figure 3.3D), the core being composed of the PnBA block. The subsequent layer is formed by the PAA of the block copolymer interacting with the silsesquioxane nanoparticles. With increasing distance from the core and decreasing PAA segment density, the uptake of nanoparticles shows a gradient in the concentration profile (Figure 3.3). An uptake of strongly hydrophilic nanoparticles into the hydrophobic core can be reasonably excluded.

3.4   Dialysis experiments with labelled silsesquioxane nanoparticles

Silsesquioxane nanoparticles were labelled with Rhodamine B to observe their location after dialysis at pH 9 and to ensure that no free nanoparticles remained in the solution (Figure 3.4). Determination of dialysis conditions is required for the FT-IR measurements and reported below. Furthermore, dialysis experiments provide a qualitative insight into the strength of the interaction between PAA and the silsesquioxane nanoparticles at pH 9 at different salinity.

The dialysis was continued until the dialysate did not show any colour or fluorescence of the labelled nanoparticles. The required dialysis time was two weeks with seven times changing the dialysate. The solution of the nanohybrids at 0.1 M NaCl released more labelled nanoparticles than the one without salt, as seen from the colour of the solutions after dialysis (Figure 3.4). The solutions with salt released the labelled nanoparticles faster, as the first dialysates were more intensely coloured than the corresponding dialysates of the organic-inorganic nanohybrids without salt.
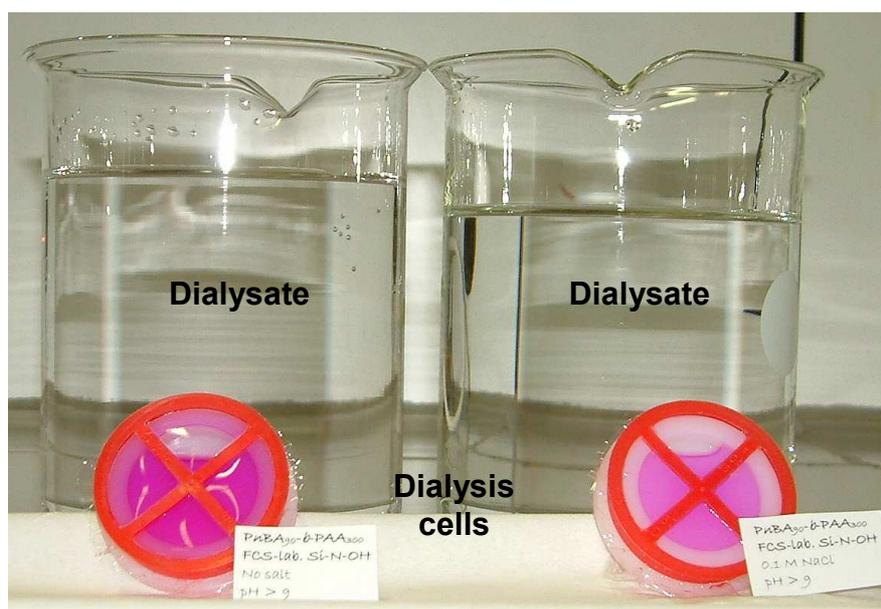

Figure 3.4. Dialysis experiments with organic-inorganic nanohybrids composed of PnBA$_{90}$-b-PAA$_{300}$ and Rhodamine B labelled silsesquioxane nanoparticles without added salt (left side) and with 0.1 M NaCl (right side) at pH 9. The dialysis cells and the dialysates at daylight after two weeks of dialysis are shown.

Two conclusions may be drawn upon these observations: First, at complete deprotonation of the PAA corona and only ca. 10% residual protonation of the nanoparticles (pH ≈ 9) the micelles still bind nanoparticles, which cannot be completely removed by dialysis. Second, the salt-free nanohybrid solutions bind more nanoparticles than the salt-containing ones (Figure 3.4). This is in good agreement with the well-known salt effect in polyelectrolytes[27,28,34,36] and IPECs[89-92,136,137].

3.5   Fourier-transform infrared spectroscopy experiments

For FT-IR measurements (Figure 3.5) the same dialysis method was used to prepare samples of the PnBA$_{90}$-b-PAA$_{300}$ micelles and the corresponding nanohybrids at pH 9 as well as at pH 5. Samples were prepared at a ratio r = [n(nanoparticle)/n(AA)] = 0.25 and dialyzed. Then, the dialyzed solutions were freeze-dried and the dry samples were analysed as KBr pellets by FT-IR. The spectra of the pure micelles obtained at pH 9 and the silsesquioxane nanoparticles do not differ significantly (Figure 3.5A) except in the wave-number region between 1250 and 890 cm^{-1}, typical of Si-O-Si bands (Figure 3.5B).

The Si-O-Si stretching vibration is characteristic for silsesquioxanes at 1100-1140 cm^{-1} and 1057-1085 cm^{-1}. They can be detected as strong and sharp bands at 1123 cm^{-1} and 1039 cm^{-1} for the pure silsesquioxane nanoparticles. The corresponding bands are also found in the spectra of the organic-inorganic nanohybrids at 1120 cm^{-1} and 1060 cm^{-1} as strong and broad bands. The band at 1163 cm^{-1} in the spectra of the organic-inorganic nanohybrid can be assigned to the corresponding band in the spectra of the pure PnBA$_{90}$-b-PAA$_{300}$ micelles at pH 9 at 1167 cm^{-1} that correspond to the deformation vibration of the alkyl functions.[122,166,167] The combination of bands confirms the presence of the nanoparticles in the micelles at pH 9 that was already indicated by the dialysis of the Rhodamine B labelled nanohybrids.

At pH 5 (Figure 3.5C,D) the Si-O-Si bands in the spectra of the nanohybrids are significantly stronger than in the spectra at pH 9 (Figure 3.5A,B). Both spectra are normalized to the band of the carbonyl function (1737 cm^{-1}, COOR) which is not affected by the pH change for better comparison. The carboxylate band (1570 cm^{-1}) is significantly decreased as PAA is less deprotonated at pH 5 than at pH 9. Those two changes in the spectra indicate that the interaction is dominated by the PAA proton.
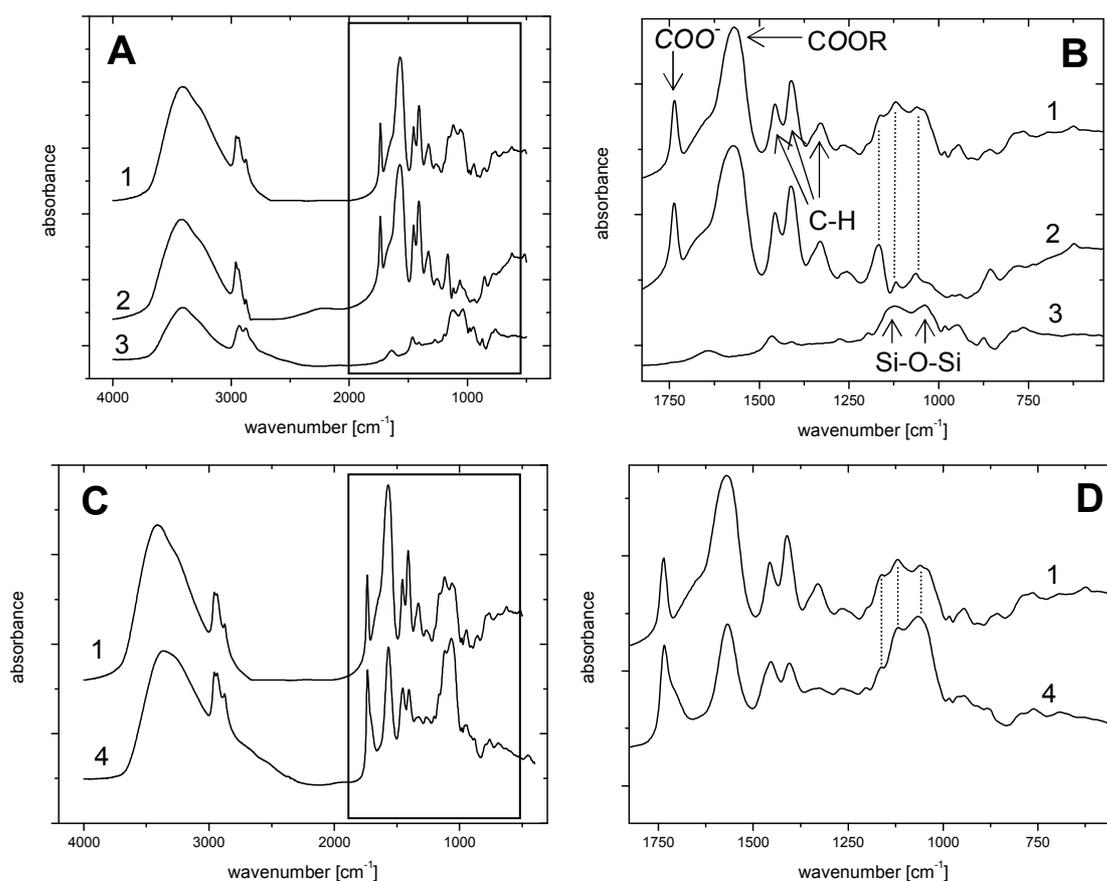
Figure 3.5. FT-IR measurements of the silsesquioxane nanoparticles (3), PnBA$_{90}$-b-PAA$_{300}$ micelles (2) and the corresponding nanohybrids at pH 9 (1) and pH 5 (4). r = [n(nanoparticle)/n(AA)] = 0.25 before the dialysis. Measurements are shown after two weeks of dialysis without added salt followed by freeze-drying. B shows an expansion of A. C compares the organic-inorganic nanohybrids at pH 9 (1) and at pH 5 (4). D shows an expansion of C.

3.6 Potential complexation mechanism

All presented data point to an equilibrium for the formation of the organic-inorganic nanohybrid. The more silsesquioxane nanoparticles are in the solution the more can take part in the formation of the organic-inorganic nanohybrid, what can be seen in the LS titrations (Figure 3.2, Table 3.1). This means on the other side that the longer the dialysis is performed, the more nanoparticles are expelled from the nanohybrid again. Nevertheless, dialysis with the Rhodamine B labelled nanoparticles (Figure 3.4) and the corresponding FT-IR measurements (Figure 3.5) shows that even after an exhaustive dialysis the organic-inorganic nanohy-

brid is conserved to a certain extent. LS titration (Figure 3.2) and dialysis (Figure 3.4) experiments also show the difference depending on salinity. Lower salinity leads to nanohybrids with a higher amount of silsesquioxane nanoparticles within the micelle, e.g. a higher count rate in the LS titrations and a stronger colour in the dialysis experiment.

Additionally, the LS titrations give a deeper insight in the interaction mechanism of the complex formation. The significant difference in the evolution of the scattering intensity with increasing nanoparticle concentration and pH can be explained taking the main driving forces for complexation into account: attractive Coulomb interactions and hydrogen bonding between acrylic acid and the tertiary amine functions of the silsesquioxane nanoparticles.

At low pH (3.5 < pH < 7.5) the acrylic acid corona of the micelle is partially (or nearly completely) protonated[45,46] and hence may participate in a hydrogen-bonding complexation as discussed by Mori et al.[112,122] The negatively charged corona results in an additional attraction of the partially oppositely charged silsesquioxane nanoparticles ($pK_a = 7.6 \pm 0.2$) by Coulomb forces. Whereas attractive ionic interactions are easily accepted to contribute substantially at low ionic strength, they are less effective at high ionic strength as charges are efficiently screened in the presence of sufficient salt. Hence, hydrogen-bonded *and* ionic complexation interactions are present at low ionic strength, whereas hydrogen-bonding remains a driving force for complex formation at high ionic strength. This is evident in the lower total scattering intensity at 0.1 M NaCl indicating nanohybrids with lower molecular mass compared to the case of low salinity.

In the alkaline regime, i.e. pH > 7.5, the acrylic acid functions are mostly ionized and cannot contribute significantly to the hydrogen-bonding between the micellar corona and the nanoparticles. Only ionic interaction between the oppositely charged components can mediate complexation comparable to the well-known IPECs[89-92,136,137]. At low ionic strength ionic forces can be easily considered to be sufficient to grant an effective interaction between micelles and nanoparticles. At high ionic strength, charges are screened and hence less effective. The incorporation of nanoparticles in a less stretched corona may cause an entropic penalty due to steric demands of the nanoparticles. An uptake of nanoparticles at high pH and high ionic strength is energetically less favourable, causing the partial release of nanoparticles of the nanohybrids under these conditions. This can be seen in the LS titrations at 0.1 M salinity (Figure 3.2A): after reaching the maximum (pH > 7.5) also the nanoparticle concentration in the solution is increasing while the count rate is decreasing. Nevertheless, the count rate of the nanohybrid at pH > 8 is still increased compared to the count rate of the pure micelle (Figure 3.2) showing that there is still interaction of the micelles and the nanoparticles at this pH. The

same is observable in the dialysis experiments (Figure 3.4) which are performed at pH 9 and are still coloured because of the interaction of the micelle with the Rhodamine B labelled nanoparticles. Finally FT-IR measurements at pH 9 (Figure 3.5) again prove the complexation at high pH.

Scheme 3.1. Potential interaction mechanism between the silsesquioxane nanoparticles and the PAA chains of the P*n*BA-*b*-PAA micelles.
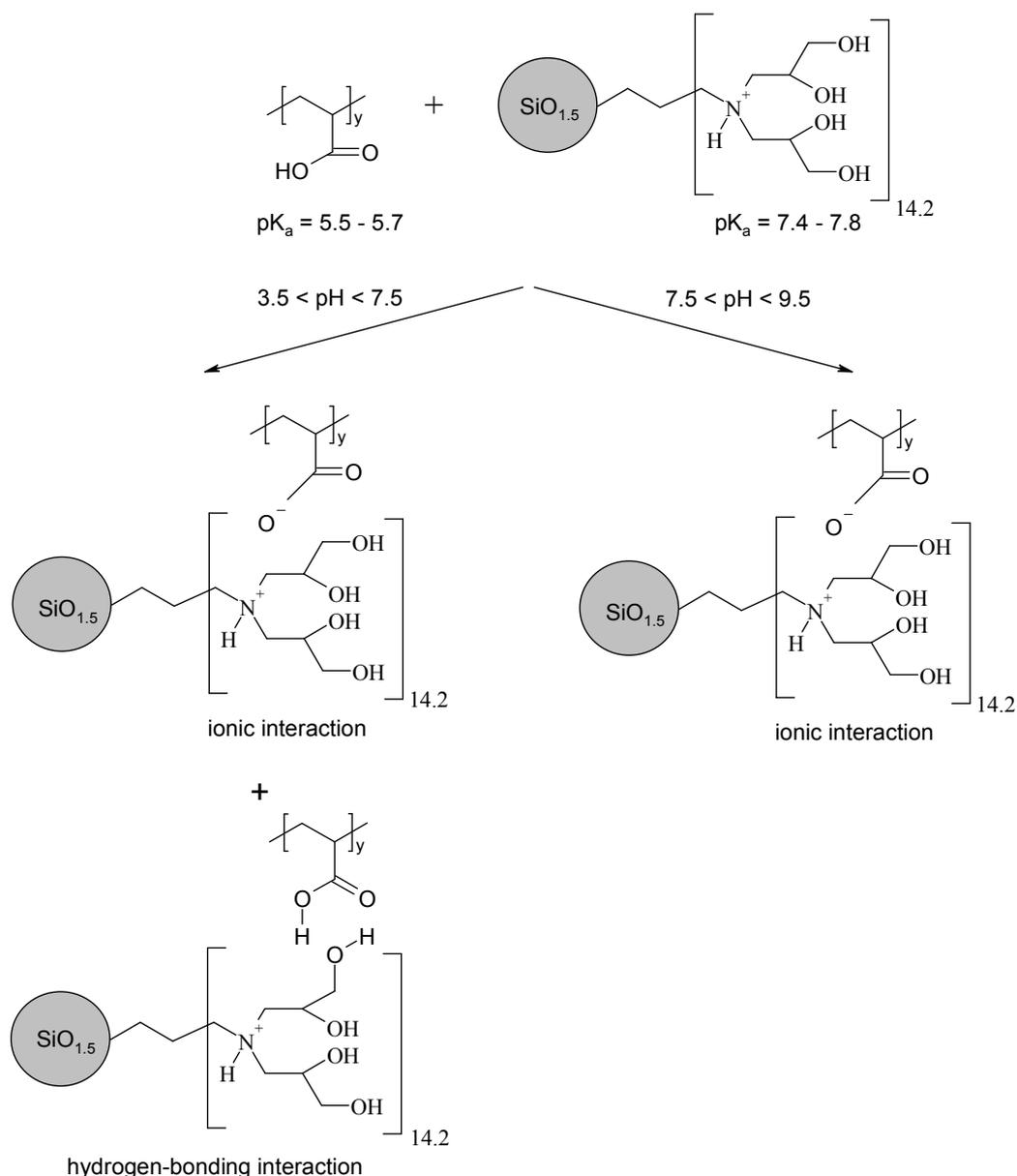
Following the discussion above, we may discriminate two major complexation mechanisms depending on the pH of media (Scheme 3.1). At low pH complexation is driven by hydrogen-bonding as well as ionic interactions between micelles and nanoparticles. At high pH, only ionic interactions can mediate complexation. Depending on ionic strength, attractive

Coulomb interactions may be (i) either sufficient to promote complexation even at high pH, where hydrogen-bonding is absent (low ionic strength, Figure 3.2B), or are (ii) screened (high ionic strength, Figure 3.2A), resulting in less favourable interactions between micelles and silsesquioxane nanoparticles.

3.7   Quantifying the amount of silsesquioxane nanoparticles incorporated in the micellar organic-inorganic nanohybrids

After proving the easy formation of organic-inorganic nanohybrids through mixing of aqueous solutions of silsesquioxane nanoparticles and a basic solution of micelles of amphiphilic block copolymers, quantifying the amount of incorporated nanoparticles within the micelle or for better comparison the amount of nanoparticles per acid functionality, r, is the next step in the investigation of this micellar nanohybrid system. To prove the postulated complexation mechanism (Scheme 3.1) and to quantify the amount of nanoparticles within the micelles at different pH and salinity various methods were used.

A first qualitative analysis was already shown through the calculation of r_{LS} based on LS titration experiments (page 55ff.). Further promising methods for this question are static light scattering (SLS) experiments, asymmetric flow field-flow fractionation (AFFFF) measurements, isothermal titration calorimetry (ITC) experiments, small angle neutron scattering (SANS) experiments and thermographimetric analysis (TGA).

SLS measurements and AFFFF experiments provide the possibility to determine and to compare the molecular weights of the micelles and the organic-inorganic nanohybrids at different pH and salinity in solution. Isothermal Titration (ITC) experiments lead to a different insight in the complexation mechanism. SANS experiments and an appropriate fitting model that needs to be developed may give detailed insight in the structure of the formed organic-inorganic nanohybrids. On the other hand, the fitting model for SANS data may allow the calculation of the amount of nanoparticles incorporated in the micelles. TGA experiments offer another way to quantify the incorporated nanoparticles in the nanohybrid but require a dialysis treatment prior to the measurements. The results obtained with the various methods are shown below.

3.7.1 Static Light Scattering experiments

Static light scattering (SLS) measurements were performed with all three micellar systems at pH 9 and 0.1 M NaCl and evaluated with Zimm plots. Table 3.3 presents the results. The aim of the measurements was to determine the amount of nanoparticles (*nano*) in the micelle represented through the value $r_{SLS} = n_{nano}$ per $n_{[AA]}$ (per acid functionality; for better comparison of the different nanohybrid systems). The calculation is done through subtraction of the obtained molecular weights of the pure micelles from the obtained molecular weights of the nanohybrids followed by division through the molecular weight of the nanoparticles, the known aggregation number of the micelles[45] and the degree of polymerization[46].

The radius of gyration, R_g, of the micelles is not influenced through the interaction of the nanoparticles as R_g of the nanohybrids is constant within the error. This was expected as the hydrodynamic radius, R_h, according to dynamic light scattering (DLS) measurements (Table 3.1) stays within the same range after complexation.[168] The same holds true for the obtained sizes from cryogenic transmission electron microscopy (cryo-TEM; Figure 3.3, Table 3.2).[168]

At pH 9 and high salinity the interaction is the weakest leading to values that are expected to be rather small. Undialyzed nanohybrids should contain more nanoparticles than dialyzed ones. Otherwise the estimated r_{SLS} values are so small that meaningful differences are rather unlikely to be expected. Nevertheless, in all cases the molecular weights of the nanohybrids are slightly increased compared to the molecular weights of the net micelles. This shows that complexation at high pH and salinity is taking place and enables us to quantify the amount of silsesquioxane nanoparticles within the nanohybrids. Also r_{SLS} appears to be small recalculation leads to values between 160 and 1300 nanoparticles per micelles what is a quite impressive number of nanoparticles under these conditions.

Table 3.3. Results of the Zimm plot evaluation of the SLS measurements of different micelles and nanohybrids (c_{NaCl} = 0.1 M, pH 9)

		10^{-6} M_w [g/mol]	10^6 A_2 [mol mL/g^2]	R_g [c)] [nm]	r_{SLS} [d)]
P*n*BA$_{90}$-*b*-PAA$_{300}$	micelle [a) 45]	10.7	43	65	-
	hybrid [a)]	10.9	16	60	0.002
P*n*BA$_{100}$-*b*-PAA$_{150}$	micelle [b)]	6.8	17	43	-
	hybrid [b)]	7.1	37	41	0.001
P*n*BA$_{90}$-*b*-PAA$_{100}$	micelle [b)]	5.8	13	28	-
	hybrid [b)]	8.4	-6	25	0.016

[a)] not dialyzed; [b)] 48 hours dialyzed; [c)] radius of gyration; [d)] $r_{SLS} = n_{nano}$ per $n_{[AA]}$

3.7.2 Asymmetric Flow Field-Flow Fractionation (AFFFF) experiments

AFFFF experiments may give a more detailed insight in the pH-dependence of the complexation especially as AFFFF in combination with a multi-angle light scattering (MALS) detector provides the possibility to study the nanohybrid system without any further treatment like dialysis after the mixing process of the micellar solution and the nanoparticle solution. As the system is able to react on external stimuli the required dialysis step for SLS (Table 3.3) and TGA (Table 3.8) investigations most probably influences the system. As we showed previously[168] the system is an equilibrium system meaning that the more extended the dialysis is performed the more nanoparticles are expelled from the micellar corona again (page 64ff.). All this drawbacks can be avoided by the investigation of the system via AFFFF as the free nanoparticles in solution, which are not taking part in the complexation mechanism, are assumed not to disturb the measurement. Avoiding the dialysis step is also the reason that the quantitative values for the amount of nanoparticles (n_{nano}) per acid function ($n_{[AA]}$) are expected to be larger than the ones determined form SLS (Table 3.3) and TGA (Table 3.8) experiments. The only drawback of the method is that during the measurement a shear force is exerted to the micelles and the corresponding nanohybrids that cannot be avoided.

Table 3.4. Results of the AFFFF experiments with different micellar systems at pH 6 and 9 and 0.01 M NaCl with r_{AFFFF}= n_{nano} per $n_{[AA]}$.

	pH	system	M_w [10^6 g/mol]	R_g [nm]	PDI (= Mw/Mn)	r_{AFFFF}
PnBA$_{90}$-b-PAA$_{300}$	9	micelle	3.3	47	1.04	-
		hybrid	4.8	53	1.02	0.013
	6	micelle	6.1	53	1.16	-
		hybrid	13.6	51	1.43	0.026
PnBA$_{100}$-b-PAA$_{150}$	9	micelle	4.7	48	2.18	-
		hybrid	5.1	42	2.28	0.002
	6	micelle	6.8	26	1.59	-
		hybrid	9.3	26	1.29	0.015

The experiments were performed with two different micellar systems (PnBA$_{90}$-b-PAA$_{300}$ and PnBA$_{100}$-b-PAA$_{150}$) at pH 6 and 9 at low salinity (0.01 M NaCl) as there the complexation rates are expected to be the highest. The results of the measurements are listed in Table 3.4. The difference of the molecular weights between the nanohybrid, $M_{w,nanohybrid}$, and the micelle, $M_{w,mic}$, was divided by the molecular mass of the silsesquioxane nanoparticle, M_{nano}, the aggregation number, N_{agg}, of the micelle[45] and the degree of polymerization, DP, of the amphiphilic block copolymer yielding to

$$r_{AFFFF} = n_{nano} \; per \; n_{[AA]} = \frac{\left(M_{w,nanohybrid} - M_{w,mic}\right)}{M_{nano} \cdot N_{agg} \cdot DP}$$

(3.3)

The values at pH 6 are higher by a factor of two than those at pH 9. This is in good agreement with the postulated interaction mechanism (Scheme 3.1). The r values obtained by SLS (Table 3.3) and AFFFF (Table 3.4) are in a comparable range. Figure 3.6 shows the obtained AFFFF measurement of the PnBA$_{90}$-b-PAA$_{300}$ micelle and the corresponding nanohybrid at pH 6 and 0.01 M NaCl. The increased molecular mass of the nanohybrid is obviously seen in Figure 3.6A. Figure 3.6B reveals the constant radius of the micelles and the nanohybrid. The corresponding radii of all measurements are presented in Table 3.4.
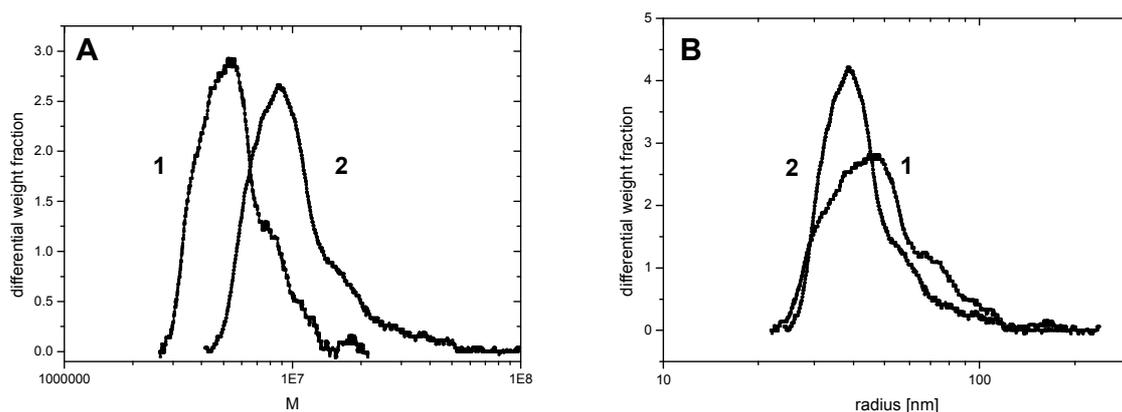
Figure 3.6. AFFFF results of the P*n*BA$_{90}$-*b*-PAA$_{300}$ micelle (1) and the corresponding nano-hybrid (2) at pH 6 and c_{NaCl} = 0.01 M. A showing the molecular weight distribution (MWD) and B the distribution of the radius of gyration (R$_g$).

3.7.3 Isothermal Titration Calorimetry (ITC)

ITC measurements provide another chance to quantify the amount of silsesquioxane nanopar-ticles within the nanohybrid without disturbing the system, e.g. through dialysis, like in the case of SLS (Table 3.3) or TGA (Table 3.8) experiments. The measurement was exemplarily performed with P*n*BA$_{90}$-*b*-PAA$_{300}$ micelles (pH 6, 0.1 M NaCl) which were titrated with a highly concentrated nanoparticle solution (pH 9, 0.1 M NaCl) to reduce the dilution effects on the one hand and to ensure complete filling of the micelles with the nanoparticles on the other hand. The required background measurements were performed through titration of Millipore-water (pH 6, 0.1 M NaCl) titrated with the same nanoparticle solution and with the used mi-cellar solution titrated with Millipore-water (pH 9, 0.1 M NaCl) to study the effect of dilution and pH change. The second background measurement did not show any changes in the heat, q, and was due to that not taken into account.

The measurement of the complexation (Figure 3.7A, black line) and the corresponding back-ground (Figure 3.7A, red line) measurement are shown in Figure 3.7. The green line in Figure 3.7A shows the smooth and overlaying baseline for both measurements representing that the system was able to reach an equilibrium state between each titration step. Figure 3.7A dis-plays the untreated raw data of the experiments representing the amount of heat per titration step in units of µcal per second shown versus the reaction time in units of minutes.

First, it is obvious that the complexation is an exothermic reaction as there is heat gener-ated with each addition of nanoparticles to the micellar solution. Furthermore, it can be de-

duced that the maximum amount of nanoparticles is incorporated within the micelles roughly after 900 minutes of reaction time as the measurements curves of the experiment and the background are overlaying. So no more silsesquioxane nanoparticles are able to interact with the micellar corona afterwards and all later observed effects are due to dilution. The amount of generated heat is high within the first titration steps followed by a time of less generated heat. This sequence is repeated three times. This behaviour can be explained through an equilibrium binding reaction. The more silsesquioxane nanoparticles are present in the solution the more can be incorporated in the micellar corona. Additionally, the change of the pH during the measurement may have an influence. The performed second background measurement points out that the pH change has no major effect on the micellar side but this does not exclude the potential influence of the pH change on the interaction of the PAA and the nanoparticles as expected from the previously shown other experiments[168] (page 54ff.).

Figure 3.7B shows the recalculated ITC data after background subtraction ($\bigcirc$) and the corresponding fit (straight line) with the model of a single set of identical sites. The fitted values of the binding reaction are given in Table 3.5. The value n_{nano} per $n_{micelle}$ can be recalculated to n_{nano} per acid functionality (n[AA]) for easier comparison with other experiments. This results in $r_{ITC} = 0.28$ nanoparticles per acid functionality what is rather high in comparison to the previous with other methods determined values. As already mentioned ITC measurements do not disturb the system. As the complexation is an equilibrium reaction higher values are expected to be obtained by methods which work with the undisturbed nanohybrid solutions, e.g. AFFFF (Table 3.4), ITC or light scattering (LS) titration (page 55ff.). The LS titration experiments yield to comparably high values for these conditions (starting pH 6, 0.1 M NaCl; up to $r_{LS} = 0.18$). Nevertheless, the value determined by AFFFF is lower by a factor of ten.
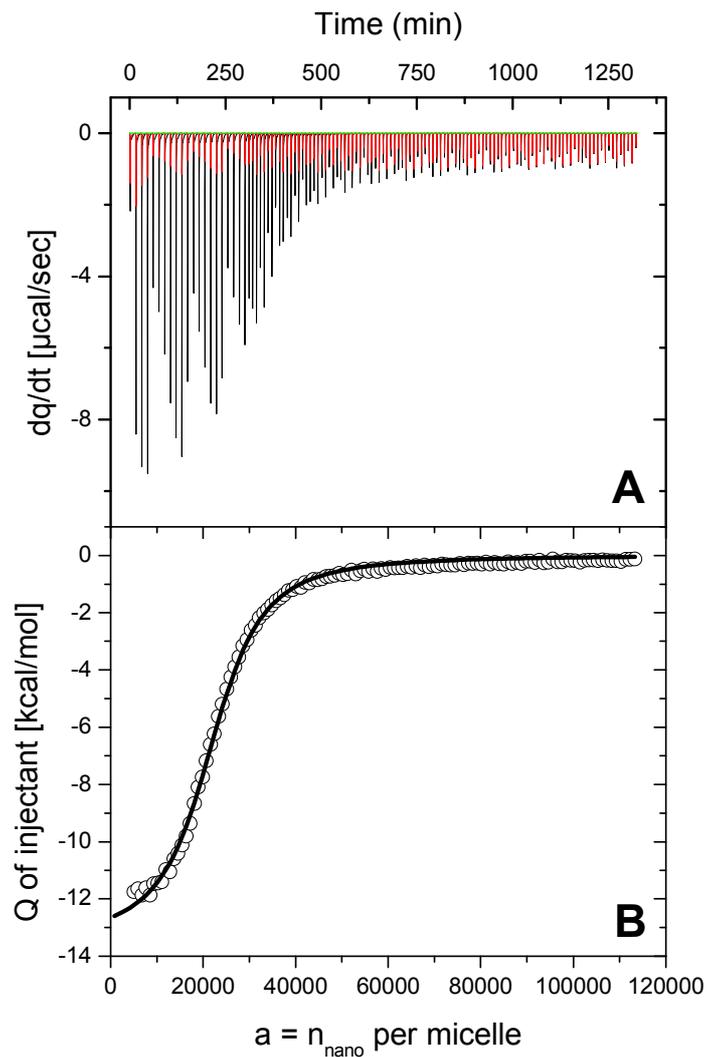
Figure 3.7. Original ITC data of PnBA$_{90}$-b-PAA$_{300}$ micelles (A, black curve; c = 0.194 g/L, starting pH 6, c_{NaCl} = 0.1 M) titrated with a silsesquioxane nanoparticle solution (c = 49.57 g/L, pH 9, c_{NaCl} = 0.1 M) without background (A, red curve; Millipore-water, pH 6, c_{NaCl} = 0.1 M titrated with the same silsesquioxane nanoparticle solution) subtraction. The green line in A shows the baseline. The symbol (○) in B represent the recalculated ITC data after background subtraction and the corresponding fit (B, straight line). The molar ratio, a, corresponds to n_{nano} per micelle.

Table 3.5. Results of the fit with a "single set of sites" model of ITC measurement with K as the binding constant, ΔH^0 as the apparent enthalpy of the binding and ΔS^0 as the entropy of the binding.

n_{nano} per micelle	$22{,}800 \pm 110$
r_{ITC}	0.28
K	$30{,}500 \pm 1000$
ΔH^0 [cal/mol]	$-13{,}500 \pm 100$
ΔS^0 [cal/(mol*K)]	-24.6 ± 0.3

According to the ITC data the equilibrium constant for the process, K, is quite high. The negative value of ΔS^0 is to be expected for a complexation reaction. The negative value of the binding enthalpy indicates that the whole process is enthalpy-driven.

3.7.4 Small angle neutron scattering (SANS) experiments

Experiments are performed at pH 9, as pH changes led to precipitation. As this behaviour is only observable in D_2O we ascribe this effect to the known differences between D_2O and H_2O. The aim for SANS measurements was to investigate the structural changes inside the micelle during complexation in more detail. Additionally, the amount of nanoparticles within the nanohybrid should be quantified with the help of SANS experiments. All curves of the nanohybrids with different amount of nanoparticles within the solution but the same pH and salinity have been fitted simultaneously to get a consistent set of parameters. The only fitting parameters are N_{agg}, I_0, t and β_{nano} together with the background contribution I_{inc}, where N_{agg} and I_0 are taken as global fitting parameters and are the same for all scattering curves. The shell thickness, t, influences only the shape of the scattering curve but not the forward scattering. Therefore the increase of the forward scattering is a sensitive measure for the amount of nanoparticles incorporated inside the micelles. The parameterization for the model has been chosen to account for all constrains determined by the chemical composition of the nanohybrid complexes.
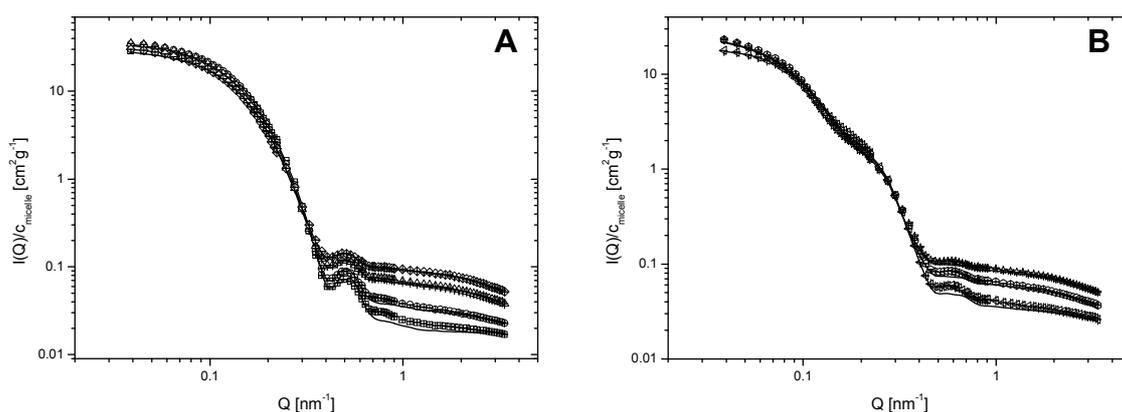
Figure 3.8. Experimental data of the SANS experiments (symbols) and the corresponding fits (straight lines) for PnBA$_{90}$-b-PAA$_{100}$ nanohybrids (A; □, ○, △, ◇) and PnBA$_{90}$-b-PAA$_{300}$ nanohybrids (B; ◁, ○, ☆) with increasing content of silsesquioxane nanoparticles at pH 9 and c$_{NaCl}$ = 0.1 M (denotation in Table 3.6) together with the error bars of each measurement point.

Figure 3.8 shows the fitting result (continuous line) together with the experimental data (symbols) of the PnBA$_{90}$-b-PAA$_{100}$ nanohybrids (A) at pH 9 and 0.1 M salinity as well as the PnBA$_{90}$-b-PAA$_{300}$ nanohybrids (B) under the same conditions with different amount of silsesquioxane nanoparticles in the polymer solution. The symbols and stoichiometric compositions of the micelle-nanoparticle solutions are given in Table 3.6. Error bars of each measurement point are indicated in Figure 3.8. All shown experiments still contain the incoherent background. All nanohybrid solutions were prepared with increasing content of silsesquioxane nanoparticles. The experimental data of the PnBA$_{100}$-b-PAA$_{150}$ nanohybrids showed with increasing silsesquioxane nanoparticle content in the solution a significant change in the structure factor. Due to that simultaneous fitting of the experimental SANS data of the nanohybrids with different content of nanoparticles was not possible.

Table 3.6. Denotation of the stoichiometry of the mixed solutions of the $PnBA_{90}$-b-PAA_{100} micelles and the nanoparticles as well as for the $PnBA_{90}$-b-PAA_{300} micelles and the nanoparticles.

sample	m_{nano} / $m_{micelle}$	n_{nano} / micelle	$x_{nano,\,stoich}$ = n_{nano} / block copolymer	r_{stoich} = n_{nano} / AA unit
$PnBA_{90}$-b-PAA_{100} (N_{agg} = 440)				
☐	1.2	2641	6.00	0.060
○	3.0	6527	14.8	0.148
△	6.0	13146	29.9	0.299
◇	9.0	19542	44.4	0.444
$PnBA_{90}$-b-PAA_{300} (N_{agg} = 270)				
◁	2.6	6281	23.3	0.078
⬠	5.3	12704	47.1	0.157
☆	7.9	18763	69.5	0.232

The fitting parameters for the investigated nanohybrids are given in Table 3.7. The value I_{inc} corresponds to the fitted background. Here it is to note that the chain stretching parameter (equation 2.30) was set to $\alpha = 2$ in all studied cases. This is well in agreement with what is expected for a stretched conformation of a charged polymer chain in alkaline solution. Hence, this value was kept constant as a global fitting parameter for all fits to reduce the number of fitting parameters and to allow more accuracy in the determination of the quantity of nanoparticles trapped within PAA micelle.

Table 3.7 shows the core radius, R_c, of the nanohybrid composed of PnBA and the additional polyelectrolyte shell, t, consisting of PAA interacting with the silsesquioxane nanoparticles. As we found during the fitting process that the core radius is not affected during the interaction of the micelles with the nanoparticles, it was used as a global parameter. It results to $R_c = 10.71$ nm for $PnBA_{90}$-b-PAA_{100} nanohybrids and $R_c = 8.77$ nm for $PnBA_{90}$-b-PAA_{300} nanohybrids. The values are in comparable range to the values obtained for R_c of the net micelles ($R_c = 11.3$ nm for $PnBA_{90}$-b-PAA_{100} and $R_c = 9.7$ nm for $PnBA_{90}$-b-PAA_{300}).[45] No significant changes during the fitting process were obtained when the polyelectrolyte shell, t, was fitted independently for each SANS experiments. Consequently, this value was also set as a global parameter. Anyhow, a significant change in size is not expected considering the stretched conformation of PAA in alkaline solution. The size of the nanohybrid detectable via

SANS experiments is given as $R = R_c + t$, meaning 22.95 nm for the PnBA$_{90}$-b-PAA$_{100}$ nano-hybrids and 35.34 nm for the PnBA$_{90}$-b-PAA$_{300}$ nanohybrids.

Considering the excess scattering length of PAA and the nanoparticles, the quantity h_{nano} can be used to calculate the number of nanoparticles per amphiphilic block copolymer $x_{nano} = n_{nano}$ per block copolymer according to

$$h_{nano} \cdot \beta_{PAA} = x_{nano} \cdot \beta_{1,nano} \qquad\qquad \textbf{3.4}$$

with $\beta_{PAA_{100}} = 4932$ fm, $\beta_{PAA_{300}} = 14792$ fm and the scattering length of one nanoparticle $\beta_{1,nano} = 2596$ fm (Table 2.3). h_{nano} describes how much the nanoparticles contribute to the scattering relative to β_{PAA} of the PAA of a single block copolymer and has been used as a fit parameter. Here we note that h_{nano} is subject to an error of 10 %.

The value x_{nano} representing the amount of silsesquioxane nanoparticles within the PAA of the block copolymer can be divides by the DP of the PAA block of the block copolymer to obtain the number of nanoparticles per AA unit, r, (Table 3.7). Those values increase with increasing amount of nanoparticles in the solution. When compared with stoichometric quantity it is realized that only a fraction of nanoparticles is incorporated within the micelles. This clearly indicates an equilibrium between trapped and free nanoparticles under the conditions studied herein. The comparison of the entrapped silsesquioxane nanoparticles, r_{fit}, with the added amount of nanoparticles in the micellar solution, r_{stoich}, shows that 0.4 to 4.7 % of the added nanoparticles are taking part in the complexation. Consequently, the complexation mechanism must be an equilibrium process, as the addition of more nanoparticles into the polymer solution leads to a higher amount of entrapped nanoparticles within the micelle at the same pH and salt content shifting the equilibrium towards the side of the organic-inorganic nanohybrids.

The knowledge of the excess scattering length of all nanoparticles on one block co-polymer, β_{nano} (equation 2.37), and PAA may be also used to obtain the excess scattering length of the shell of the nanohybrid, β_{sh}, which can be written as

$$\beta_{sh} = \beta_{PAA} + \beta_{nano} = \beta_{PAA}\left(1 + h_{nano}\right) \qquad\qquad \textbf{3.5}$$

leading to

$$\beta_{nano} = \beta_{PAA} \cdot h_{nano} \qquad\qquad \textbf{3.6}$$

Equation 3.5 was used to calculate β_{nano} in Table 3.7. So the values h_{nano} and x_{nano} differ only by a calculation factor.

Table 3.7. Fitting parameters for the PnBA$_{90}$-b-PAA$_{100}$ nanohybrids as well as the PnBA$_{90}$-b-PAA$_{300}$ nanohybrids at pH 9 and c_{NaCl} = 0.1 M with $\beta_{PAA_{100}}$ = 4932 fm, $\beta_{PAA_{300}}$ =14792 fm and $\beta_{1,nano}$ = 2596 fm corresponding to the excess scattering length of a single silsesquioxane nanoparticle.

	β_{nano} [fm]	I_{inc}	h_{nano}	x_{nano}	r_{fit} = x_{nano} / AA unit	r_{fit} / r_{stoich}	R_c [nm]	t [nm]
			PnBA$_{90}$-b-PAA$_{100}$ (N$_{agg}$ = 440)					
□	534	0.001	0.108	0.21	0.0021	0.034	10.71	12.24
○	1804	0.025	0.366	0.69	0.0069	0.047	10.71	12.24
△	2424	0.067	0.491	0.93	0.0093	0.031	10.71	12.24
◇	1580	0.094	0.320	0.61	0.0061	0.014	10.71	12.24
			PnBA$_{90}$-b-PAA$_{300}$ (N$_{agg}$ = 270)					
◁	247	0.035	0.017	0.10	0.0003	0.004	8.77	26.57
⬡	2929	0.062	0.198	1.13	0.0038	0.024	8.77	26.57
☆	3908	0.089	0.264	1.51	0.0050	0.022	8.77	26.57

The quality of the data is not good enough to provide more precise information about the distribution of the particle within the star-like micelle additionally to the information that the nanoparticles are equally distributed along the PAA chain (Gaussian distribution of the nanoparticles within the micellar PAA shell), although the fitting model included a beta function to discriminate the position of the nanoparticles within the PAA of the single block copolymer (fitting of the single experimental data let always to a homogenous distribution). As the fitting routine did not lead to any safe determination of the position of the nanoparticles within the polyelectrolyte micelle, the beta function was not fitted in the global fits.

Fitting of the experimental SANS data shows that the formed nanohybrids consist of a PnBA core with comparable size as the net micelles[45]. The interaction of the silsesquioxane nanoparticles is as expected[168] just taking place within the PAA shell of the micelles (Scheme 3.1). The organic-inorganic nanohybrids possess a core-shell morphology with gradually decreasing amount of nanoparticles incorporated within the PAA shell.

3.7.5 Thermogravimetric analysis (TGA) experiments

Figure 3.9 shows the TGA traces of the reference substances (Figure 3.9A) as well as the PnBA$_{90}$-b-PAA$_{300}$ nanohybrids (Figure 3.9B, traces 4 - 7) at different pH (5 and 9) and salinity (0.0 M and 0.1 M NaCl). This amphiphilic block polymer was investigated as it is representative for all micellar nanohybrids. Trace 1 shows that the complete organic polymer is vanished after 14440 seconds (= 520 °C). The silsesquioxane nanoparticles (trace 2) are transformed to SiO$_2$ under the applied conditions. The transformation is completely finished after 22700 s (= 750 °C). The original mass of silsesquioxane nanoparticles (m_{nano}) can be recalculated with the mass of the residue ($m_{residue}$) as

$$m_{nano} = m_{residue} \cdot \frac{M_{nano}}{14.2 \cdot M_{SiO_2}}$$

3.7

with M_{nano} and M_{SiO_2} as the molecular weight of the nanoparticles and the formed siliciumdioxid. The error of this calculation is less than 2 % in the case of the pure silsesquioxane nanoparticles. Trace 3 representing the behaviour of NaCl under these conditions shows a sharp sublimation process in the region of 23000 to 27800 seconds (= 790 to 925 °C). Sublimation at this temperature is reasonable as NaCl is fine dispersed within the micelles leading to an earlier sublimation.
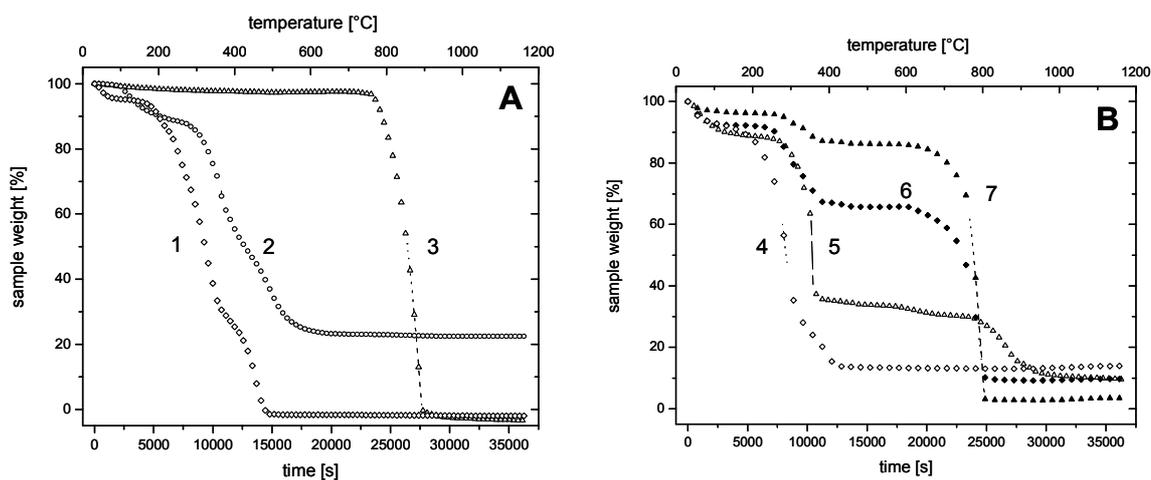

Figure 3.9. TGA traces of the reference substances (A: PnBA$_{90}$-b-PAA$_{300}$ polymer (1), silsesquioxane nanoparticles (2), NaCl (3)) and the PnBA$_{90}$-b-PAA$_{300}$ nanohybrids at different pH and salt (B: pH 5: no salt (4), 0.1 M NaCl (6); pH 9: no salt (5), 0.1 M NaCl (7)).

Summarizing this leads to the conclusion that NaCl has no effect on the amount of residue of the nanohybrids after the TGA experiment and that the residue can be taken as a direct measure of the amount of silsesquioxane nanoparticles within the micelles. The actual salt content of the sample can be calculated through the calculated mass loss between 23000 and 27800 seconds. This is a necessary step in the accurate calculation of the amount of nanoparticles and polymer in the dialyzed, freeze-dried nanohybrid sample. As already mentioned in the experimental part, the amphiphilic block copolymer needs to be dissolved in alkaline solution, followed by screening of the charges via addition of NaCl to get very monodisperse micelles. After complexation of the micellar solution with nanoparticle solution the pH needs to be adjusted. All these steps lead to the generation of salt in the nanohybrid solution. The subsequent required exhaustive dialysis procedure makes the accurate calculation of the amount of salt within the nanohybrid solution, which is subsequently freeze-dried, impossible. The same sample preparation was also used for the samples without salt, requiring to cross-check via this calculation method the actual amount of salt within the nanohybrid.

Afterwards, the mass of the amphiphilic polymer within the nanohybrid can easily be calculated via the difference of the weighed in sample minus the calculated accurate mass of the salt and minus the mass of the nanoparticles. With the knowledge of the exact composition of the dried nanohybrid sample the calculation of content of nanoparticles (n_{nano}) per micelle or per acid functionality ($n_{[AA]}$) for the various samples is possible (Table 3.8).

Table 3.8. Content of silsesquioxane nanoparticles (n_{nano}) within the micelle and per acid functionality ($n_{[AA]}$) for different micellar systems determined with TGA experiments at pH 5 and 9 different salinity with $r_{TGA} = n_{nano}$ per $n_{[AA]}$.

	c_{NaCl} [mol/L]	pH	n_{nano} per micelle	r_{TGA}
PnBA$_{90}$-b-PAA$_{300}$	0.0	9	2400	0.030
		5	4330	0.053
	0.1	9	610	0.008
		5	490	0.006
PnBA$_{100}$-b-PAA$_{150}$	0.0	9	3370	0.051
		5	2180	0.033
	0.1	9	950	0.014
		5	1570	0.024
PnBA$_{90}$-b-PAA$_{100}$	0.1	9	1150	0.031
		5	570	0.015

As expected, Table 3.8 shows that the content of silsesquioxane nanoparticles within the nanohybrid decreases with increasing salt content. High salinity decreases the possibility for

ionic interaction between the charged PAA of the micelle and the amino function of the nanoparticles as the charges are more effective screened. This is well in agreement to our postulated complexation mechanism (Scheme 3.1). The known pH dependence of the complexation does not show any significant trend. Most probably the analysis method is not sensitive enough to extract such detailed information. According to the previously shown experiments (page 54ff.) with this system we expected that the amount of nanoparticles within the nanohybrid increases with lower pH. At lower pH (pH 5) the possibility exists to form complexes via ionic bonds and hydrogen-bonding, as in the case of alkine solution (pH 9) just ionic bonds can be accounted for the interaction as depicted in Scheme 3.1. Another important factor is that TGA experiments require an exhaustive dialysis procedure as already mentioned. This leads to an extraction of a large number of interacting silsesquioxane nanoparticles as the interaction is an equilibrium process. Consequently, the number of determined nanoparticles within the micelle via TGA resembles the amount of strongly bound nanoparticles within the micelle and not the amount of nanoparticles being able to interact with the micelle in a nanohybrid solution without prior dialysis.

3.8   Conclusions

Mixing aqueous solutions of anionic block copolymer micelles and of silsesquioxane nanoparticles leads to the easy and straightforward formation of organic-inorganic nanohybrids. DLS, LS titration, SLS, AFFFF, SANS and cryo-TEM confirm that the size of the micelles is preserved during formation of the water-soluble nanohybrids.

LS titrations give an insight in the postulated interaction mechanism. Complexation in acidic media is driven by hydrogen-bonding and ionic interaction, in alkaline media nanohybrids are mainly formed due to ionic interaction. The reason for the size conservation is most probably due to the kinetically frozen micellar core and the compensation of (i) increased steric repulsion due to complexation and (ii) attractive interactions between the silsesquioxane nanoparticle and the charged PAA. FT-IR and dialysis measurements with fluorescently labelled silsesquioxane nanoparticles confirm the nanohybrid formation over a relatively wide range in pH. Cryo-TEM micrographs point a core-shell structure of the nanohybrids with gradually decreasing nanoparticle density. The responsiveness of the system on pH and salinity as external stimuli is shown with LS titration, dialysis and FT-IR measurements. LS titration experiments allow a first quantitative analysis of the amount of incorporated silsesquioxane nanoparticles within the micellar system.

A more detailed and quantitative analysis of the system was performed by SLS, AFFFF, ITC, SANS and thermogravimetry. SLS and AFFFF demonstrate constant radii of the micelles and the formed organic-inorganic nanohybrids. Quantifying the amount of nanoparticles incorporated in the micelles turns out to be an arduous task. SLS of dialysed and undialysed samples and AFFFF of undialysed samples clearly show increased molecular weights of the formed nanohybrids compared to the net micellar systems under the same conditions. Furthermore, those experiments show the tenability of the system with salinity and pH. TGA requires an exhaustive dialysis procedure prior to the measurements. This affected the amount of nanoparticles within the micellar systems as complexation is an equilibrium process. Nevertheless, also TGA shows increased molecular masses of the nanohybrids and allows the recalculation of the incorporated nanoparticles amount.

ITC provides an insight in the complex formation. Additionally, quantifying of the amount of nanoparticles within the nanohybrids is possible leading to rather high values compared to all other investigated methods. SANS experiments have been conducted at basic conditions and provide information about the inner structure of the nanohybrids. The new developed fitting model enables the determination of the radial profiles of the organic-inorganic nanohybrids, which is used to get a more detailed insight in the structure of the organic-inorganic nanohybrids. Additionally, it allows the calculation of the amount of silsesquioxane nanoparticles per micelle under these conditions.

The responsiveness of the system on external stimuli (pH and salinity) is shown with TGA and AFFFF measurements. All various used methods to determine the amount of nanoparticles incorporated within the micelles sustain the formation of the organic-inorganic nanohybrids. Also the calculated values for the amount of interaction nanoparticles per acid functionality appear to be small (mostly around 0.002 to 0.053, depending on the used method and conditions), recalculation to nanoparticles incorporated within one micelle leads to a quite high number of interacting nanoparticles (160 to 4300).

4 Smart organic-inorganic nanohybrid stars based on star-shaped poly(acrylic acid) and functional silsesquioxane nanoparticles

Poly(acrylic acid) (PAA) stars can directly be dissolved in Millipore water containing 1.1 equivalents of NaOH with respect to the carboxylic functions of the PAA, leading to polyelectrolyte star solutions at pH 9. NaCl can be added subsequently. The pH of the star solutions was adjusted by addition of HCl. The silsesquioxane nanoparticles are highly functionalized with in average 14.2 tertiary amino groups per particle, each amino function bearing four hydroxyl groups. The radius of the nanoparticles (r = 1.5 nm)[112,122] in aqueous solutions is still small compared to the size of the stars (r = 10 - 23 nm at pH 9 and 0.1 M NaCl; Table 4.1).

For the formation of the water-soluble nanohybrid stars the star solutions were simply mixed at room temperature with an aqueous solution of the silsesquioxane nanoparticles possessing the same salinity as the star solution. The pH of the formed nanohybrid stars was adjusted by addition of HCl solution. The effect of pH and salinity in the system was studied as they were shown earlier (Chapter 3) to play an important role in the interaction between the silsesquioxane nanoparticles and PAA.

4.1 Dynamic Light Scattering (DLS) and LS titrations experiments

DLS measurements (Table 4.1) provide a first insight into the system. LS titration measurements show systematic changes within the star system during the addition of the nanoparticles. Here, star polyelectrolyte solutions were titrated with a solution of nanoparticles using online pH monitoring and simultaneous dynamic and static LS measurements that were performed on quiescent solutions subsequently after each titration step. The titrations were performed up to a relatively high ratio of nanoparticles per acrylic acid unit of the star polymer, r = n(nanoparticles)/n(AA), to ensure oversaturation, which might provoke crosslinking of stars. Here we note that DLS (intensity-weighted CONTIN plot, Figure 4.1) and cryo-TEM (Figure 4.3 indicated by circles) revealed a minor quantity of large aggregates already present in pure star solutions in the case of the $(PAA_{100})_{21}$ star system. In a mass-weighted size distribution the fraction of aggregates is negligible. We attribute these aggregates to counterion mediated star-star aggregation of fully extended PAA stars, which is sustained by the fact that their amount decreases with increasing salt content.
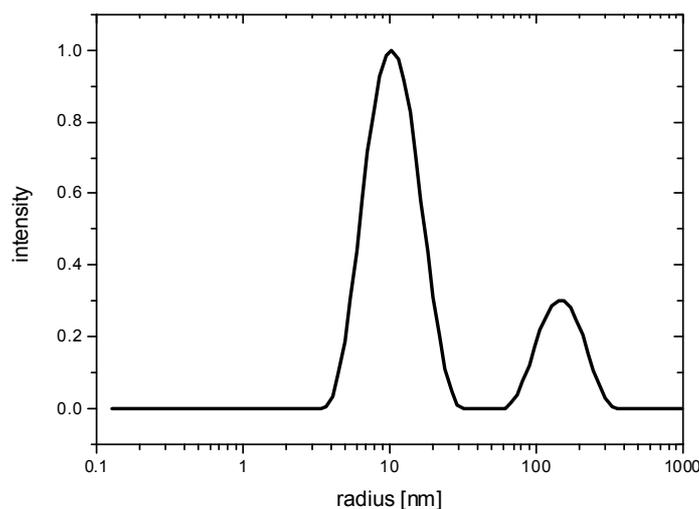
Figure 4.1. Typical intensity-weighted CONTIN plot of pure $(PAA_{100})_{21}$ star polymer at pH 5 and 0.1 M NaCl showing single, well-separated stars and a minor fraction of star-star aggregates.

In the case of $(PAA_{200})_{24}$ star-star aggregation led to a characteristic broadening of the size distribution as obtained by CONTIN analysis of the DLS correlation function. This broadening (Table 4.1) may be rationalised considering the insufficient resolution to discriminate between single PAA stars and star-star aggregates (with this instrument a factor of 2 to 3 in diffusion times is at least required to discriminate different species). Addition of nanoparticles led to sharper distributions as the screening of charges leads to a lower stretching of the PAA arms and hence to a more globular morphology that is in contrast to star-star aggregation.[27,28,34,36]

Table 4.1. Radii of star systems from DLS and from cryo-TEM measurements ($c_{polymer}$ = 0.5 to 1.0 g/L) at pH 9 before addition of silsesquioxane nanoparticles and at a final stoichiometric ratio r = n(nanoparticles)/n(AA) = 0.28 to 0.60.

	c_{NaCl} [mol/L]	$R_{h,z}$ [nm] pure star	$R_{h,z}$ [nm] nanohybrid	$R_{n,TEM}$ nanohybrid
$(PAA_{100})_{21}$	0.1	10 ± 1	12 ± 1	12 ± 1
	0.02	10 ± 1	10 ± 1	-
$(PAA_{200})_{24}$	0.1	23 ± 2 (broad)	14 ± 2 (sharp)	15 ± 1
	0.02	24 ± 3 (broad)	18 ± 1 (broad)	-

CONTIN analysis of the DLS data of each titration step shows a constant hydrodynamic radius of 10 ± 1 nm in the case of 0.02 M NaCl (Table 4.1) for the $(PAA_{100})_{21}$ stars and the corresponding nanohybrids. In the case of 0.1 M NaCl (Table 4.1Table 3.1) the size of the nanohybrids (12 ± 1 nm) is slightly larger than the corresponding pure star (10 ± 1 nm; Figure 4.1). Nevertheless, this size change is within the experimental error. The evaluation of the differences between the pure star and the nanohybrid stars was arduous in the case of the $(PAA_{200})_{24}$. As already mentioned the size distribution was broadened (Table 4.1). Nevertheless, no nanoparticle induced crosslinking of various stars was observed for both star polymers. However, the hydrodynamic radius - as obtained by DLS - is insufficient to provide clear evidence for complexation between the PAA stars and nanoparticles. Here, the discussion of the scattering intensity is more valuable and provides more detailed information.

Figure 4.2A (0.1 M NaCl) and C (0.02 M NaCl) show the LS titration measurements of the $(PAA_{100})_{21}$ star with the nanoparticles. Figure 4.2B (0.1 M NaCl) and D (0.02 M NaCl) depicts the same measurement of the larger star $(PAA_{200})_{24}$. The pH increase for all LS titrations is due to the silsesquioxane nanoparticle solution, having an intrinsic pH of 8 to 9. The polyelectrolyte star solutions were not buffered to eliminate any influence of additional components. All LS titrations (Figure 4.2) show a distinct effect in the scattering intensities, measured as the count rates at 90°. The count rate of the star solutions with a starting pH of around 5 shows a remarkable increase in intensity by a factor of 4~5 for the case of high salinity. In the case of low salinity the effect is even more pronounced with an increased scattering intensity of 10~11. As the count rate depends on the weight concentration, c, and the molecular weight, M_w, of scattering particles and the refractive index increment, dn/dc, and the equipment specific constant K', this increase is a strong indication for the formation of particles with higher molecular weight, i.e. complexation of the stars and silsesquioxane nanoparticles.

$$I = K' c \cdot M_w \cdot \left(\frac{dn}{dc} \right)^2 \qquad \qquad \textbf{4.1}$$

This is true as long as dn/dc of the nanohybrid stars does not increase significantly, the number of the stars stays constant and the pure nanoparticles do not have any significant contribution to the scattering intensity of the solution. The nanoparticles possess a refractive index increment, dn/dc = 0.150 mL/g without added salt and of 0.151 mL/g for the solutions with 0.1 M NaCl. Furthermore almost no scattering signal of the pure nanoparticles in solution can be detected because of their low molecular weight (M_w = 3760 g/mol). The concentration of the stars and the corresponding nanohybrid stars decreases by 19.5 to 23.1 % of the

original value as a result of dilution during titration. The dilution was taken into account for all calculations. The dn/dc values for the polyelectrolyte stars (($PAA_{100})_{21}$: 0.244 mL/g and ($PAA_{200})_{24}$: 0.197 mL/g) are higher than that of the silsesquioxane nanoparticles. In conclusion, the increased count rate can be only explained by an increased molecular weight, indicating the formation of complexes. The apparent hydrodynamic radii of the stars do not change significantly during complex formation within experimental error (Table 4.1).
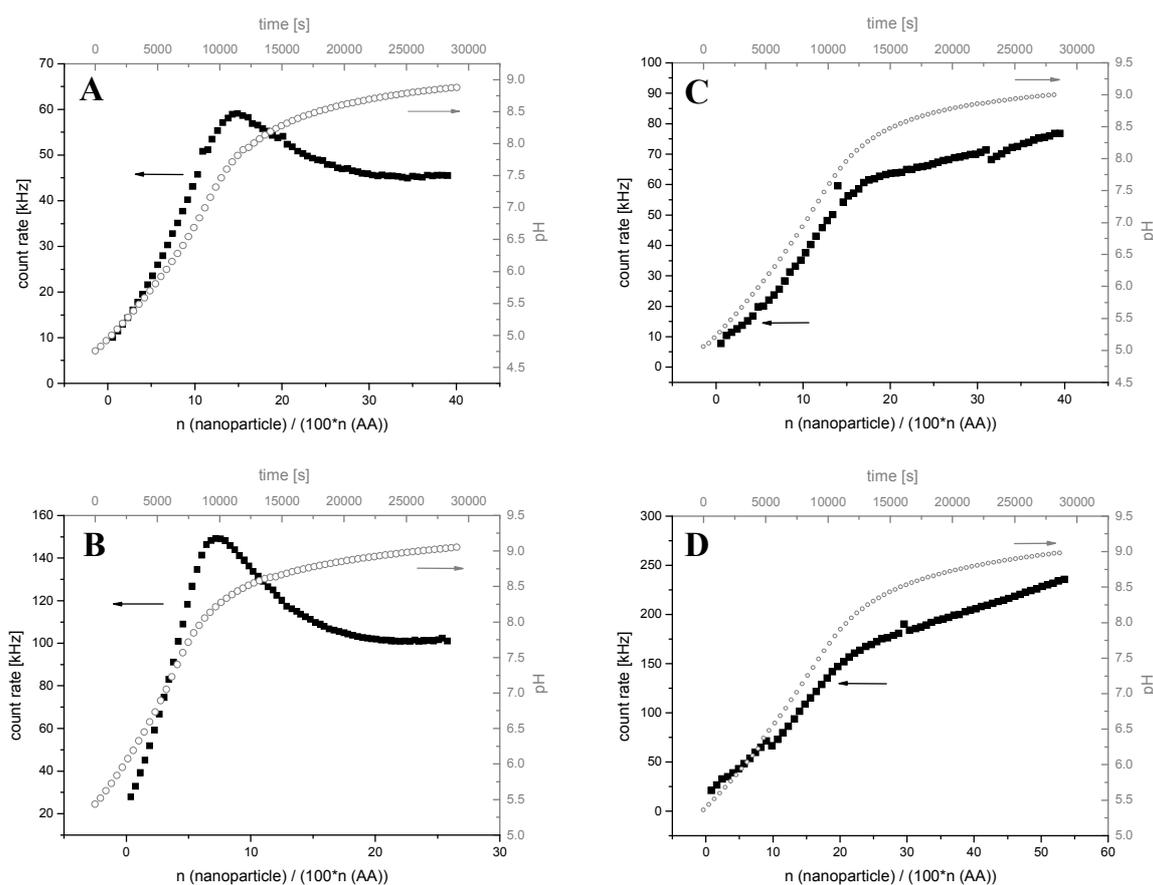
Figure 4.2. Light scattering intensities (■) and pH values (○) during titration of ($PAA_{100})_{21}$ stars (A: $c_{polymer}$ = 0.989 g/L, c_{NaCl} = 0.1 M, starting pH 4.76; C: $c_{polymer}$ = 1.010 g/L, c_{NaCl} = 0.02 M, starting pH 5.06) and ($PAA_{200})_{24}$ (B: $c_{polymer}$ = 0.958 g/L, c_{NaCl} = 0.1 M, starting pH 5.43; D: $c_{polymer}$ = 0.942 g/L, c_{NaCl} = 0.02 M, starting pH 5.36) with the silsesquioxane nanoparticles (100 g/L).

Both star systems with 0.1 M NaCl (Figure 4.2A,B) exhibit an increase of the count rate with each titration step until a maximum is reached. A further increase of the nanoparticle concentration leads to gradually decrease of the scattering intensity, which converges to a value 4 to 5 times higher than the initial scattering intensity. The already mentioned observable second peak (Figure 4.2) in the ($PAA_{100})_{21}$ star solutions does not increase during addi-

tion of nanoparticles compared to the peak of the pure polyelectrolyte star. The decrease of the count rate starts at pH ~ 8 (0.1 M NaCl, Figure 4.2A and Figure 4.2B). In the cases of low salinity no maximum is observed (Figure 4.2C,D) and the count rate is gradually increasing, reaching a plateau at ca. 10~11 times the initial value. However, a significant change in the slope of the count rate can be detected at pH ~ 8. The absolute scattering intensity is higher than in the case of high ionic strength, because the charges of the polyelectrolyte system with low salt content are less screened. As a result the force to entrap nanoparticles into the PAA star is stronger, leading to nanohybrid stars with a larger number of interacting nanoparticles and due to that to a higher molecular weight.

This indicates that the interaction between nanoparticles and PAA stars is the strongest for pH < 8 in the case of high salinity. At higher pH the interaction strength weakens, resulting in either a release of nanoparticles at high ionic strength or a diminishing uptake of nanoparticles in the case of low ionic strength. This is in good agreement with the observation that $(PAA_{100})_{21}$ stars with a starting pH > 8 do not show any significantly increase in the count rate during the LS titration measurement.

Mori et al.[112] found maximum turbidity in the range of pH 2.5 to 5.7 for linear PAA. Retsch et al.[123] observed a binding maximum at pH = 5.3 for planar PAA brushes, whereas the strongest interaction for $PnBA_{90}$-b-PAA_{300} micelles at high salinity was found for pH < 7.5 (chapter 3).[168] The fact that the stability of IPECs decreases with increasing salinity is well-known.[89-92,136,137] It indicates that ionic interactions play a significant role in the complexation process.

In conclusion, LS titration measurement revealed a distinct impact of pH and salinity on the interaction strength between PAA stars and nanoparticles. The strongest interactions are present for pH < 7.8, where hydrogen-bonding and Coulomb interactions may be envisaged as main driving forces for complexation. For pH > 8 only ionic interaction or weak hydrogen-bonding interactions may mediate complex formation at intermediate and high pH, respectively. This is sustained by the fact, that an uptake of nanoparticles is maintained at low ionic strength, while a saturation limit is observed at high ionic strength, where Coulomb interactions are known to be effectively screened. This indicates that the degree of ionization of the PAA is a key factor for an effective interaction with the nanoparticles and that hydrogen-bonding also plays a vital role.[112,113]

4.2 Cryogenic transmission electron microscopy experiments

Typical cryo-TEM micrographs of the nanohybrid stars (pH 9, 0.1 M NaCl) are shown in Figure 4.3. No staining agent was added. This provides direct evidence for the presence of nanohybrid complexes as the contrast of the pure PAA stars is insufficient to be visible without staining. The evident contrast can be solely attributed to the incorporation of silsesquioxane nanoparticles.

All samples measured by cryo-TEM are solutions after LS titration measurements, i.e. in the presence of a high nanoparticle concentration. Even under these conditions no nanoparticle induced star-star aggregation is evident (Figure 4.3A and B). The few larger assemblies in Figure 4.3A (circles) are already present in the pure star polymer solutions and are attributed to counterion-mediated star-star aggregation as already mentioned above.

The cryo-TEM micrographs of $(PAA_{100})_{21}$ (Figure 4.3A) and $(PAA_{200})_{24}$ (Figure 4.3B) clearly prove the uniform distribution of the poly(acrylic acid) nanohybrid stars without significant crosslinking. The single nanohybrid stars exhibit an increased electron and mass density compared to the water background leading to a high contrast (dark spots in the corresponding cryo-TEM micrographs) and they are well separated. The scale bar in the two mentioned micrographs is different (100 nm for $(PAA_{100})_{21}$ in Figure 4.3A and 200 nm for $(PAA_{200})_{24}$ in Figure 4.3B) due to the different size of the corresponding nanohybrid stars.

The detectable radius of the nanohybrid stars was evaluated by the method of the grey-scale analysis.[168] Here, the high intensity values correspond to low contrast. i.e. the lighter parts and vice versa. Thus, the part with an intensity value of 0.0 in the grey-scale analysis corresponds to the PAA-silsesquioxane complex of the nanohybrid star as the data were normalized to be zero for the star centre. The corresponding radial average of the grey scale intensities are shown in Figure 4.3C for the (PAA_{100}) and in Figure 4.3D for $(PAA_{200})_{24}$. Both figures illustrate a continuous increase of the grey-scale intensity with increasing distance from the star centre. The radius is deduced at 90% of the total grey-scale intensity, where a distinct change in the slope is evident. For the nanohybrid $(PAA_{100})_{21}$ stars at 0.1 M NaCl (Figure 4.3C) we obtain a radius of 12 ± 1 nm which is in good agreement to the DLS measurements of the nanohybrid stars that give a hydrodynamic radius of 12 ± 1 nm (Table 4.1). The same holds true of the larger PAA star and its corresponding nanohybrids. From Figure 4.3D a radius of 15 ± 1.0 nm is evaluated at 90% intensity, close to the hydrodynamic radius.
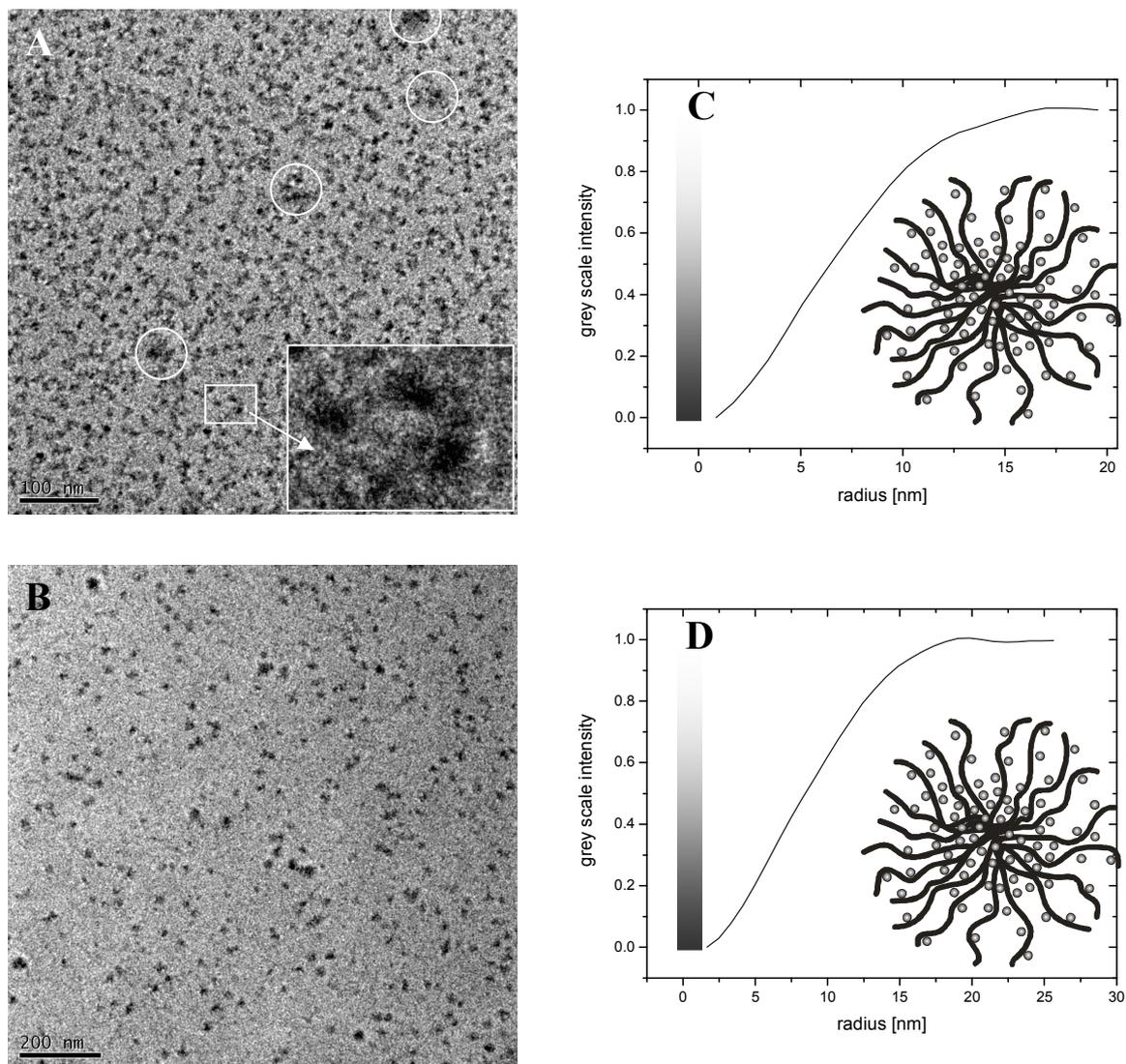
Figure 4.3. Cryo-TEM micrographs of nanohybrid stars after LS titration measurements (A: $(PAA_{100})_{21}$; B: $(PAA_{200})_{24}$) without any additional staining at pH 9 and 0.1 M NaCl (c_{star} ~ 1 g/L; size bar: A: 100 nm; B: 200 nm) and the corresponding grey-scale analysis (C: $(PAA_{100})_{21}$; D: $(PAA_{200})_{24}$). The circles in A represent star-star aggregates.

4.3 Small angle neutron scattering experiments

The aim for SANS measurements was to investigate the structural changes inside the star during complexation in more detail. Furthermore the amount of nanoparticles within the nanohybrid star should be quantified with the help of SANS experiments. All curves of the PAA star with different amount of nanoparticles within the solution but the same pH and salinity have been fitted simultaneously to get a consistent set of parameters. The only fitting parameters are I_0, t and β_{nano} together with the background contribution $I_{inc}+Cq^{-4}$, where I_0 is taken as a

global fitting parameter for all scattering curves. The thickness, t, influences only the shape of the scattering curve but not the forward scattering. Therefore the increase of the forward scattering is a sensitive measure for the amount of silsesquioxane nanoparticles incorporated inside the star. The parameterization for the model has been chosen to account for all constrains determined by the chemical composition of the nanohybrid complexes.
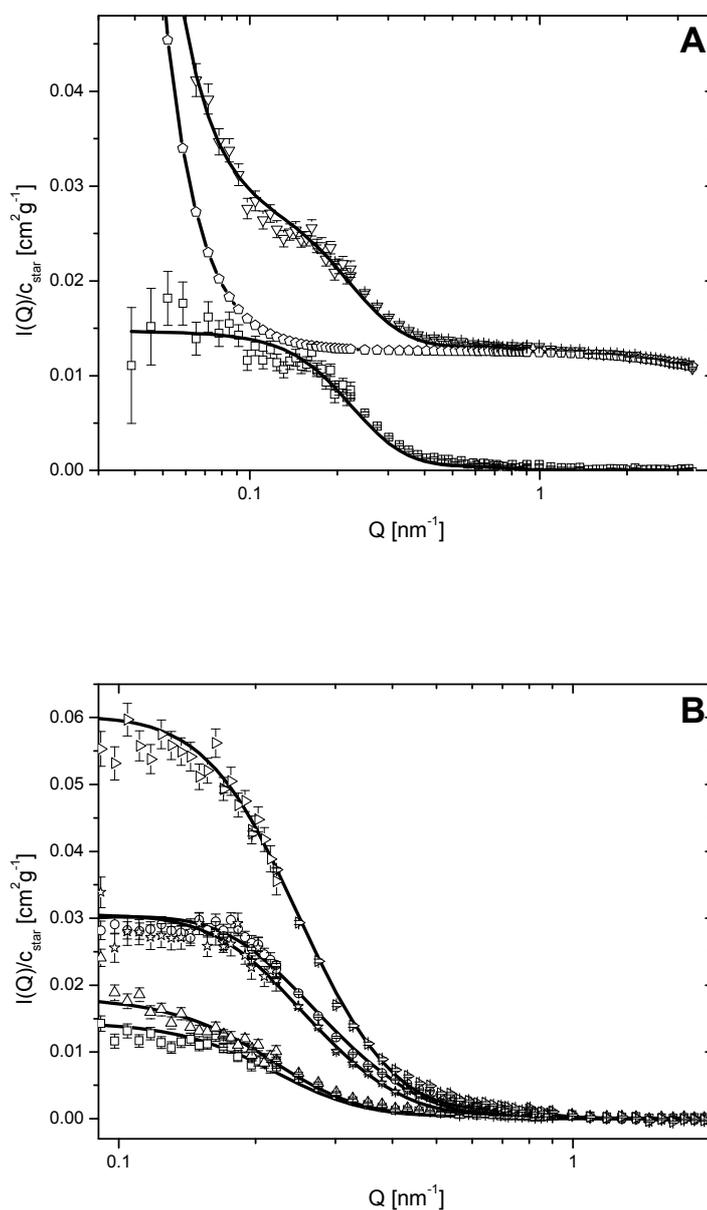

Figure 4.4. SANS experimental data and the corresponding fits for $(PAA_{100})_{21}$ star and the respective nanohybrid star at pH 9.5 and 0.1 M NaCl. A shows the experimental data of the pure star (∇), the fitted background ($\hexagon$) and the data after background subtraction ($\square$). B shows the experimental data after background subtraction with $\square$ as the pure star and all oth-

ers symbols representing the nanohybrid stars with different content of silsesquioxane nanoparticles in the solution (denotation in Table 4.2).

Figure 5A shows the fitting results (continuous line) together with the experimental data (symbols) of the pure $(PAA_{100})_{21}$ star polymer at pH 9.5 with 0.1 M NaCl. Curve 1 ($\triangledown$) shows the experimental data and the corresponding fit without background subtraction. Curve 2 ($\varhexagon$) represents the fitted background, a $I_{inc}+Cq^{-4}$ contribution to the experimental curve. It is assumed that this contribution is due to the small fraction of star aggregates, which can be described by a q^{-4} power law. Subtraction of the background from the experimental data yields to curve 3 ($\square$). Error bars of each single measurement point are shown.

In Figure 5B all plots represent experimental data after background subtraction. In addition to the pure star, the experimental scattering functions and the fitting results of the nanohybrid stars with different amount of silsesquioxane nanoparticles are shown. The symbols and the fitting results considering the composition of the star-nanoparticle solution are given in Table 4.2.

Table 4.2. Denotation of the $(PAA_{100})_{21}$ star and the stoichiometry of the mixed solutions of stars and nanoparticles.

symbol	$m_{nano}\,/\,m_{star}$	$n_{nano}\,/\,star$	$x_{nano,\,stoich}=$ $n_{nano}\,/\,arm$	$r_{stoich}=$ $n_{nano}\,/\,AA\;unit$
$\square$	0	0	0	0
$\triangle$	2.4	96	4.57	0.046
$\bigcirc$	6.1	246	11.6	0.116
$\star$	12.2	485	23.1	0.231
$\triangleright$	18.1	717	34.1	0.341

The fitting parameters for the $(PAA_{100})_{21}$ star and the corresponding nanohybrids are given in Table 4.3. The values of I_{inc} and C in Table 4.3 correspond to the fitted background ($I_{inc}+Cq^{-4}$). Here we note that the chain stretching parameter (equation 2.30) was set to $\alpha = 2$ in all studied cases. This is well in agreement with what is expected for a stretched conformation of a charged polymer chain in alkaline solution. Hence, this value was kept constant as a global fitting parameter for all fits to reduce the number of fitting parameters and to allow more accuracy in the determination of the quantity of nanoparticles trapped within the PAA star.

Table 4.3 shows the radius of the $(PAA_{100})_{21}$ star indicated through the value R_{star} to be 12.9 nm. This is within the error in good agreement with the detected apparent hydrodynamic radius (10 ± 1 nm) obtained by DLS measurements at pH 9 and 0.1 M salinity (Table 4.1). The radius of gyration, R_g, can be calculated from the radial profile of the scattering length density by,

$$R_g^2 = \frac{\int_0^{Rc+t} 2\pi r^4 \eta(r)\, dr}{\int_0^{Rc+t} 2\pi r^2 \eta(r)\, dr}$$

4.2

The size of the nanohybrid complexes is hardly affected with increasing nanoparticle concentration (R_{star} = 9.8 to 13.6 nm and R_g = 5.9 to 8.1 nm, depending on the amount of silsesquioxane nanoparticles in the solution) and well in accordance with the hydrodynamic radii obtained by DLS (R_h = 12 ± 1 nm for the nanohybrids at 0.1 M NaCl and pH 9). A significant change in size is not expected considering the stretched conformation of PAA in the alkaline solution. Guinier analysis (Table 4.3) determines R_g = 7.2 ± 0.2 for the pure star, what leads to a R_g/R_h ratio of 0.72 what is close to hard spheres with 0.775. The Guinier determination of R_g for the nanohybrids leads to values in the range of 6.1 to 7.5 (± 0.2) and consequently to a R_g/R_h ratio of 0.54 to 0.63 for the nanohybrids. The decreased R_g/R_h ratio confirms the increase of mass close to the core.

Considering the excess scattering length of PAA and the nanoparticles, the quantity h_{nano} can be used to calculate the number of nanoparticles per PAA arm x_{nano} = n_{nano} / arm according to

$$h_{nano} \cdot \beta_{PAA} = x_{nano} \cdot \beta_{1,nano}$$

4.3

with β_{PAA} = 4932 fm and the scattering length of one nanoparticle, $\beta_{1,nano}$ = 2596 fm. h_{nano} describes how much the nanoparticles contribute to the scattering relative to β_{PAA} of a PAA arm and has been used as a fit parameter. Here it is noted that h_{nano} is subject to an error of 10 %.

The knowledge of the excess scattering length of the all nanoparticles on one arm, β_{nano} (equation 2.37), and PAA may be also used to obtain the excess scattering length of the shell of the nanohybrid, β_{sh}, which can be written as

$$\beta_{sh} = \beta_{PAA} + \beta_{nano} = \beta_{PAA}(1 + h_{nano})$$

4.4

leading to

$$\beta_{nano} = \beta_{PAA} \cdot h_{nano}$$

4.5

Equation (4.5) was used to calculate β_{nano} in Table 4.3. So the values h_{nano} and x_{nano} differ only by a calculation factor.

Table 4.3. Fitted parameters for the $(PAA_{100})_{21}$ star and the corresponding nanohybrid stars at pH 9.5 and 0.1 M NaCl with $\beta_{PAA} = 4932$ fm and $\beta_{1,nano} = 2596$ fm corresponding to the excess scattering length of a single silsesquioxane nanoparticle.

symbol	β_{nano} [fm]	I_{inc}	10^6 C	h_{nano}	x_{nano}	$r_{fit} =$ x_{nano} / AA unit	r_{fit} / r_{stoich}	R_{star} [nm]	$R_g^{a)}$ [nm]	$R_g^{b)}$ [nm]
□	0	0.028	0.6	0	0	0		12.9	7.7	7.2
△	755	0.013	0.8	0.153	0.29	0.0029	0.06	13.6	8.1	7.5
○	2269	0.015	1.1	0.460	0.87	0.0087	0.08	9.8	5.9	6.1
☆	2392	0.020	1.1	0.485	0.92	0.0092	0.04	10.9	6.6	6.5
▷	5425	0.022	0.7	1.10	2.09	0.021	0.06	11.6	7.0	6.9

[a)] determined with equation 4.2; [b)] determined via Guinier evaluation

The value x_{nano} representing the amount of silsesquioxane nanoparticles within one arm of the star polymer can be divided by the DP of the arms to obtain the number of particles per AA unit, r, (Table 4.3). Those values increase with increasing amount of nanoparticles in the solution (Table 4.2). When compared with the stoichometric quantity we realize that only a fraction of nanoparticles is complexed by $(PAA_{100})_{21}$. This clearly indicates an equilibrium between trapped and free nanoparticles under conditions studied herein. The comparison of the entrapped silsesquioxane nanoparticles with the added amount of nanoparticles to the star solution shows that 4 to 8 % of the added nanoparticles are taking part in the complexation. The remaining nanoparticles stay free in the solution. Consequently, the complexation mechanism must be an equilibrium process, as the addition of more nanoparticles into the polymer solution leads to a higher amount of entrapped nanoparticles within the star at the same pH and salt content shifting the equilibrium towards the side of the organic-inorganic nanohybrid stars, what is also found for the micellar nanohybrid system (page 74ff.).

The quality of the data is not sufficient to provide more precise information about the distribution of the nanoparticles within the star additionally to the information from cryo-TEM that the nanoparticles are equally distributed along the PAA chain (Gaussian distribution of the nanoparticles within the PAA star), although the fitting model included a beta function to discriminate the position of the nanoparticles within the arm of the star (fitting of

the single experimental data let always to a homogenous distribution). As the fitting routine did not lead to any safe determination of the position of the nanoparticles within the polyelectrolyte star, the beta function was not fitted in the global fits.

The data for the $(PAA_{200})_{24}$ star and its nanohybrids are qualitatively similar, however, the quality of the data is not satisfying for a quantitative evaluation of the incorporated silsesquioxane nanoparticles within the star polymer.

4.4   Proposed interaction model and complexation mechanism

The complexation of the nanoparticles and PAA star, which leads to the formation of star-like nanohybrid complexes, is demonstrated. Whereas SANS clearly indicates an equilibrium between trapped and free nanoparticles, DLS (Table 4.1), LS titration (Figure 4.2) and cryo-TEM (Figure 4.3) do not indicate any crosslinking even at high nanoparticle concentrations. Furthermore, a detailed image analysis of cryo-TEM micrographs (Figure 4.3C,D) indicates a linear concentration profile of trapped nanoparticles within the star polymer. Based on this linear concentration profile, the SANS model well described the experimental scattering functions. Hence, the following morphology for the nanohybrid complexes is proposed.

The interaction between silsesquioxane nanoparticles and PAA star polymers is understood to be fully reversible and results in nanohybrid complexes, which are in equilibrium with free nanoparticles in alkaline solution. Cryo-TEM and SANS strongly indicate a structure for the nanohybrid complexes, where the density gradually decreases with increasing distance from the centre. The gradual decrease of the nanoparticle number density within the corona is rationalised considering the segment density gradient in the PAA star. The situation is schematically depicted in Figure 4.5.
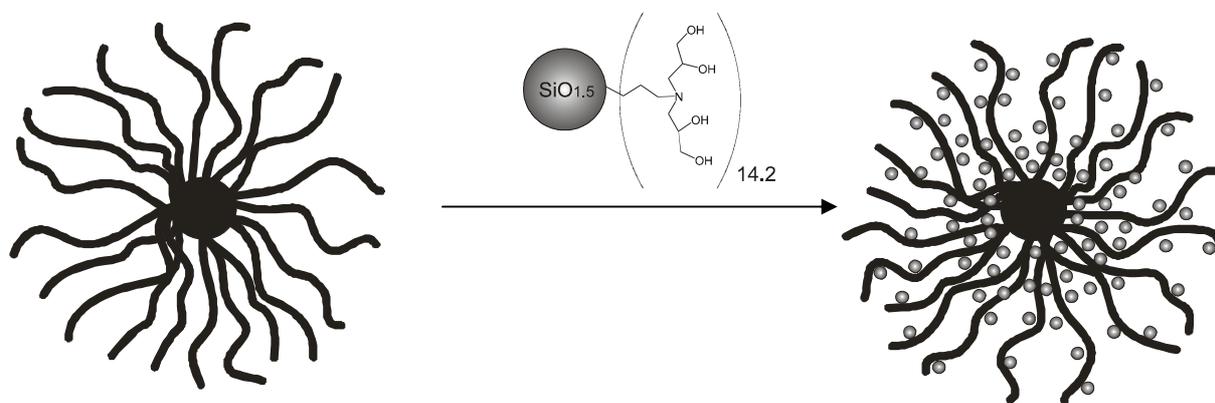

Figure 4.5. Formation of organic-inorganic nanohybrid stars.

LS titrations (Figure 4.2) demonstrate the vital role of two solution properties that affect the complexation: ionic strength and pH. The significant difference in the evolution of the scattering intensity with increasing nanoparticle concentration and pH can be understood considering the main driving forces for complexation: attractive Coulombic interactions and hydrogen-bonding between acrylic acid and the hydroxyl groups of the silsesquioxane nanoparticles as shown in Scheme 4.1 and discussed in detail previously (page 64ff.) dealing with the interaction of the nanoparticles with micelles having a PAA corona.[168]

Scheme 4.1. Potential interaction mechanism between silsesquioxane nanoparticles and PAA of the PAA star.
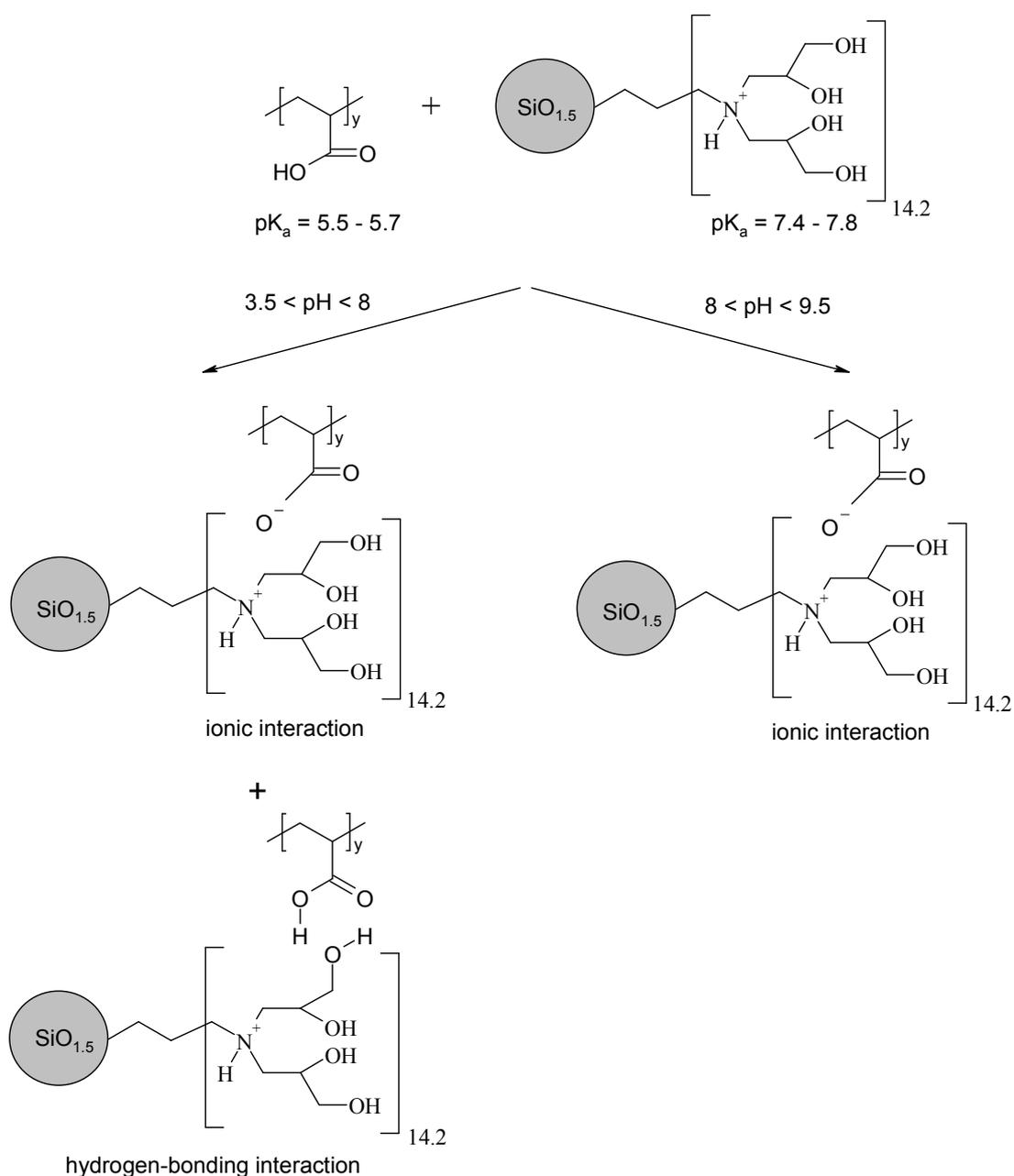
4.5   Conclusions

Mixing aqueous solutions of poly(acrylic acid) PAA stars and silsesquioxane nanoparticles results in the easy and straightforward formation of stimuli-responsive organic-inorganic nanohybrid stars. LS titration measurements provide an insight in the interaction mechanism and show the responsiveness of the system on pH and salinity as external stimuli. Complexation in acidic media is driven by hydrogen-bonding as well as ionic interaction, in alkaline media complexation is solely driven by ionic interaction. Cryo-TEM micrographs confirm the formation of organic-inorganic nanohybrid stars, indicating a gradient in nanoparticle density. This morphology was also sustained by SANS data. A new fitting model of the SANS data for this challenging system was developed that proves the interaction between the silsesquioxane nanoparticles and the PAA and enables to determine the radial profile and the calculation of the amount of entrapped silsesquioxane nanoparticles within one star.

5 References

(1)   Pitsikalis, M.; Pispas, S.; W.Mays, J.; Hadjichristidis, N. *Adv. Polym. Sci.* **1998**, *135*, 1-137.

(2)   Hadjichristidis, N.; Pitsikalis, M.; Iatrou, H. *Adv. Polym. Sci.* **2005**, *189*, 1-124.

(3)   Hadjichristidis, N.; Iatrou, H.; Pitsikalis, M.; Mays, J. *Prog. Polym. Sci.* **2006**, *31*, 1068-1132.

(4)   Tieke, B. *Makromolekulare Chemie*; 1. Auflage ed.; VCH: Weinheim, 1997.

(5)   Lechner, M. D.; Gehreke, K.; Nordmeier, E. H. *Makromolekulare Chemie: Ein Lehrbuch für Chemiker, Physiker, Materialwissenschaftler und Verfahrenstechniker*; 3. überarbeitete und erweiterte Auflage ed.; Birkhäuser Verlag: Basel, 2003.

(6)   Odian, G. *Principles of Polymerization* Fourth Edition ed.; Wiley Interscience: Hoboken, New Jersey, 2004.

(7)   Matyjaszewski, K.; Xia, J. *Chem. Rev.* **2001**, *101*, 2921-2990.

(8)   Abetz, V.; Simon, P. F. W. *Adv. Polym. Sci.* **2005**, *189*, 125-212.

(9)   Bhattacharya, A.; Misra, B. N. *Prog. Polym. Sci.* **2004**, *29*, 767-814.

(10)   Lazzari, M.; Liu, G.; Lecommandoux, S. *Block Copolymers in Nanoscience*; Wiley-VCH: Weinheim, 2006.

(11)   Hadjichristidis, N.; Pispas, S.; Floudas, G. A. *Block Copolymers: Synthetic Strategies*; Wiley-Interscience: New York, 2003.

(12)   Gido, S. P.; Lee, C.; Pochan, D. J.; Pispas, S.; Mays, J. W.; Hadjichristidis, N. *Macromolecules* **1996**, *29*, 7022.

(13)   Hadjichristidis, N. *J. Polym. Sci. A* **1999**, *37*, 857.

(14)   Hadjichristidis, N.; Iatrou, H.; Pitsikalis, M.; Pispas, S.; Averopoulos, A. *Progr. Polym. Sci.* **2005**, *30*, 725.

(15)   Leibler, L. *Macromolecules* **1980**, *13*, 1602.

(16)   Bates, F. S. *Science* **1991**, *251*, 898.

(17)   Fredrickson, G. H.; Bates, F. S. *Annu. Rev. Mater. Sci.* **1996**, *26*, 501.

(18)   Klox, H.-A.; Lecommandoux, S. *Adv. Mater.* **2001**, *13*, 1217.

(19)   Khandpur, A. K.; Forster, S.; Bates, F. S.; Hamley, I. W.; Ryan, A. J.; Bras, W.; Almdal, K.; Mortensen, K. *Macromolecules* **1995**, *28*, 8796.

(20)   Zhang, L.; Barlow, R. J.; Eisenberg, A. *Macromolecules* **1995**, *28*, 6055-6066.

(21)   Zhang, L.; Eisenberg, A. *Science* **1995**, *268*, 1728.

(22)   Gao, Z.; Varshney, S. E.; Wong, S.; Eisenberg, A. *Macromolecules* **1994**, *27*, 7923-7927.

(23)   Moffitt, M.; Khougaz, K.; Eisenberg, A. *Acc. Chem. Res.* **1996**, *29*, 95-102.

(24)   Kabanov, A. V.; Bronich, T. K.; Kabanov, V. A.; Yu, K.; Eisenberg, A. *J. Am. Chem. Soc.* **1998**, *120*, 9941-9942.

(25)   Ding, J. F.; Liu, G. J.; Yang, M. L. *Polymer* **1997**, *38*, 5497.

(26)   Cameron, N. S.; M.K., C.; Eisenberg, A. *Can. J. Chem.* **1999**, *77*, 1311.

(27)   Förster, S.; Abetz, V.; Müller, A. H. E. *Adv. Polym. Sci.* **2004**, *166*, 173-210.

(28)   Rodríguez-Hernández, J.; Chécot, F.; Gnanou, Y.; Lecommandoux, S. *Prog. Polym. Sci.* **2005**, *30*, 691-724.

(29)   Riess, G. *Prog. Polym. Sci.* **2003**, *28*, 1107-1170.

(30)   Hales, K.; Pochan, D. J. *Curr. Opinion Coll. Interface Sci.* **2006**, *11*, 330-336.

(31)   Garnier, S.; Laschewsky, A.; Storsberg, J. *Tenside Surf. Det.* **2006**, *43*, 88-102.

(32)   Burkhardt, M.; Martinez-Castro, N.; Tea, S.; Drechsler, M.; Babin, I.; Grishagin, I.; Schweins, R.; Pergushov, D. V.; Gradzielski, M.; Zezin, A. B.; Müller, A. H. E. *Langmuir* **2007**, *23*, 12864-12874.

(33)   Kennedy, J. P. *Polym. J.* **1985**, *17*, 29-35.

(34)   Khougaz, K.; Astafieva, I.; Eisenberp, A. *Macromolecules* **1995**, *28*, 7135-7147.

(35)   Liu, X. Y.; Wu, J.; Kim, J.-S. *Langmuir* **2006**, *22*, 419.

(36)   Gil, E. S.; Hudson, S. M. *Prog. Polym. Sci.* **2004**, *29*, 1173-1222.

(37)   Bronich, T. K.; Nguyen, H. K.; Eisenberg, A.; Kabanov, A. V. *J. Am. Chem. Soc.* **2000**, *122*, 8339-8343.

(38)   Smitha, B.; Sridhar, S.; Khan, A. A. *Macromolecules* **2004**, *37*, 2233-2239.

(39)   Petrov, A. I.; Antipov, A. A.; Sukhorukov, G. B. *Macromolecules* **2003**, *36*, 10079-10086.

(40)   Sui, Z.; Jaber, J. A.; Schlenoff, J. B. *Macromolecules* **2006**, *39*, 8145-8152.

(41)   Xu, Y.; Bolisetty, S.; Drechsler, M.; Fang, B.; Yuan, J.; Harnau, L.; Ballauff, M.; Müller, A. H. E. *Soft Matter*, *8, published on the web on October 24 (2008)* DOI: 10.1039/b812179f.

(42)   BASF;
http://www.chemicalportal.basf.com/p02/GS/ChemicalPortal/de_DE/portal/show-con-tent/function:pi:/wa/EU~de_DE/Catalog/Chemicals/pi/BASF/Subbrand/pluronic_pe: 2008-11-11.

(43)   Alexandridis, P.; Olsson, U.; Lindman, B. *J. Phys. Chem.* **1996**, *100*, 280.

(44)   Bae, K. H.; Choi, S. H.; Park, S. Y.; Y. Lee, T. G. P. *Langmuir* **2006**, *22*, 6380.

(45)   Colombani, O.; Ruppel, M.; Burkhardt, M.; Drechsler, M.; Schumacher, M.; Grad-
        zielski, M.; Schweins, R.; Müller, A. H. E. *Macromolecules* **2007**, *40*, 4351-4362.

(46)   Colombani, O.; Ruppel, M.; Schubert, F.; Zettl, H.; Pergushov, D. V.; Müller, A. H.
        E. *Macromolecules* **2007**, *40*, 4338-4350.

(47)   Eghbali, E.; Colombani, O.; Drechsler, M.; Müller, A. H. E.; Hoffmann, H. *Langmu-
        ir* **2006**, *22*, 4766-4776.

(48)   Gaillard, N.; Guyot, A.; Claverie, J. *J. Polymer Sci. Part A* **2003**, *41*, 684-698.

(49)   Garnier, S.; Laschewsky, A. *Macromolecules* **2005**, *28*, 7580-7592.

(50)   Garnier, S.; Laschewsky, A. *Langmuir* **2006**, *22*, 4044-4053.

(51)   Jacquin, M.; Muller, P.; Lizarraga, G.; Bauer, C.; Cottet, H.; Théodoly, O. *Macro-
        molecules* **2007**, *40*, 2672-2682.

(52)   Jacquin, M.; Muller, P.; Talingting-Pabalan, R.; Cottet, H.; Berret, J. F.; T. Futterer;
        Théodoly, O. *J. Colloid Interface Sci.* **2007**, *316*, 897-911.

(53)   Jacquin, M.; Muller, P.; Cottet, H.; Crooks, R.; Théodoly, O. *Langmuir* **2007**, *23*,
        9939-9948.

(54)   Lund, R.; Willner, L.; Richter, D.; Dormidontova, E. E. *Macromolecules* **2006**, *39*,
        4566-4575.

(55)   Bendejacq, D.; Joanicot, M.; Ponsinet, V. *Eur. Phys. J. E* **2005**, *17*, 83-92.

(56)   Bendejacq, D.; Ponsinet, V.; Joanicot, M. *Eur. Phys. J. E* **2004**, *13*, 3-13.

(57)   Bendejacq, D.; Ponsinet, V.; Joanicot, M.; Loo, Y.-L.; Register, R. A. *Macromole-
        cules* **2002**, *35*, 6645-6649.

(58)   Nyrkova, I. A.; Semenov, A. N. *Macromol. Theory Simul.* **2005**, *14*, 569-585.

(59)   Gao, L.; Shi, L.; Zhang, W.; An, Y.; Jiang, X. *Macromol. Chem. Phys.* **2006**, *207*,
        521-527.

(60)   Roovers, J.; Marcel Dekker Inc.: New York, 1999, p 285.

(61)   Quirk, R. P.; Lee, Y.; Kim, J.; Marcel Dekker, Inc.: New York, 1999, p 1.

(62)   Rühe, J.; Ballauff, M.; Biesalski, M.; Dziezok, P.; Gröhn, F.; Johannesmann, D.;
        Houbenov, N.; Hugenberg, N.; Konradi, R.; Minko, S.; Motornov, M.; Netz, R. R.;
        Schmidt, M.; Seidel, C.; Stamm, M.; Stephan, T.; Usov, D.; Zhang, H. *Adv. Polym.
        Sci.* **2004**, *165*, 79.

(63)   Burchard, W. *Adv. Polym. Sci.* **1999**, *143*, 113-194.

(64)   Freire, J. J. *Adv. Polym. Sci.* **1999**, *143*, 35-112.

(65)   Furukawa, T.; Ishizu, K. *Macromolecules* **2005**, *38*, 2911-2917.

(66)   Mandel, M. *Polyelectrolytes*; 2nd ed. New York, 1988; Vol. 11.

(67)   Dobrynin, A. V.; Rubinstein, M. *Prog. Polym. Sci.* **2005**, *30*, 1049-1118.

(68)   *Polyelectrolytes, Their Characterization and Polyelectrolyte Solutions* American Scientific Publishers: Stevenson Ranch; Vol. 2.

(69)   Deserno, M.; Holm, C.; Kremer, K. *Physical Chemistry of Polyelectrolytes*; Dekker: New York, 2001.

(70)   Manning, G. S. *J. Chem. Phys.* **1965**, *43*, 4260.

(71)   Manning, G. S. *J. Chem. Phys.* **1969**, *51*, 924-933.

(72)   Manning, G. S. *J. Chem. Phys.* **1969**, *51*, 3249-3252.

(73)   Manning, G. S.; Zimm, B. H. *J. Chem. Phys.* **1965**, *43*, 4250.

(74)   Imai, N. *J. Phys. Soc. Jpn.* **1961**, *16*, 746.

(75)   Imai, N.; Onishi, T. *J. Chem. Phys.* **1959**, *30*, 1115.

(76)   Onishi, T.; Imai, N.; Oosawa, F. *J. Phys. Soc. Jpn.* **1960**, *15*, 896.

(77)   Oosawa, F. *J. Polym. Sci.* **1957**, *23*, 421.

(78)   Oosawa, F. *Polyelectrolytes*; Dekker: New York, 1971.

(79)   Katchalsky, A.; Shavit, N.; Eisenberg, H. *J. Polym. Sci.* **1954**, *13*, 69.

(80)   Lifson, S.; Katchalsky, A. *J. Polym. Sci.* **1953**, *13*, 43.

(81)   Fuoss, F. M.; Katchalsky, A.; Lifson, S. *Proc. Natl. Acad. Sci. USA* **1951**, *37*, 579.

(82)   Jusufi, A.; Likos, C. N.; Ballauff, M. *Coll. Polym. Sci.* **2004**, *282*, 910.

(83)   Jusufi, A.; Likos, C. N.; Lowen, H. *Phys. Rev. Lett.* **2002**, *88*, 018301.

(84)   Jusufi, A.; Likos, C. N.; Lowen, H. *J. Chem. Phys.* **2002**, *116*, 11011.

(85)   Thünemann, A. F.; Müller, M.; Dautzenberg, H.; Joanny, J.-F.; Löwen, H. *Adv. Polym. Sci.* **2004**, *166*, 113-171.

(86)   Babak, V. G.; Merkovich, E. A.; Desbrieres, J.; Rinaudo, M. *Polym. Bull.* **2000**, *45*, 77.

(87)   Bertrand, P.; Jonas, A.; Laschewsky, A.; Legras, R. *Macromol. Rap. Commun.* **2000**, *21*, 319-348.

(88)   Kabanov, A. V.; Bronich, T. K.; Kabanov, V. A.; Yu, K.; Eisenberg, A. *Macromolecules* **1996**, *29*, 6797-6802.

(89)   Pergushov, D. V.; Remizova, E. V.; Feldthusen, J.; Zezin, A. B.; Müller, A. H. E.; Kabanov, V. A. *J. Phys. Chem. B* **2003**, *107*, 8093-8096.

(90)   Pergushov, D. V.; Remizova, E. V.; Gradzielski, M.; Lindner, P.; Feldthusen, J.; Zezina, A. B.; Müller, A. H. E.; Kabanov, V. A. *Polymer* **2004**, *45*, 367-378.

(91)   Burkhardt, M.; Ruppel, M.; Tea, S.; Drechsler, M.; Schweins, R.; Pergushov, D. V.; Gradzielski, M.; Zezin, A. B.; Müller, A. H. E. *Langmuir* **2008**, *24*, 1769-1777.

(92)   Pergushov, D. V.; Babin, I. A.; Plamper, F. A.; Zezin, A. B.; Müller, A. H. E. *Langmuir* **2008**, *24*, 6414-6419.

(93)   Zhao, C.; Yang, X.; Wu, X.; Liu, X.; Wang, X.; Lu, L. *Polymer Bulletin* **2008**, *60*, 495-505.

(94)   Hoffmann, F.; Cornelius, M.; Morell, J.; Fröba, M. *Angew. Chem. Int. Ed.* **2006**, *45*, 3216-3251.

(95)   Han, J. T.; Xu, X.; Cho, K. *Langmuir* **2005**, *21*, 6662-6665.

(96)   Wang, Y.-W.; Yen, C.-T.; Chen, W.-C. *Polymer* **2005**, *46*, 6959-6967.

(97)   Sanchez, C.; Julián, B.; Belleville, P.; Popall, M. *J. Mater. Chem.* **2005**, *15*, 3559-3592.

(98)   Sanchez, C.; Soler-Illia, G. J. A. A.; Ribot, F.; Lalot, T.; Mayer, C. R.; Cabuil, V. *Chem. Mater.* **2001**, *13*, 3061-3083.

(99)   Liu, Y.-L.; Lee, H.-C. *J. Polym. Sci. A* **2006**, *44*, 4632-4643.

(100)   Schmid, A.; Fujii, S.; Armes, S. P.; Leite, C. A. P.; Galembeck, F.; Minami, H.; Saito, N.; Okubo, M. *Chem. Mater.* **2007**, *19*, 2435-2445.

(101)   Vaia, R. A.; Maguire, J. F. *Chem. Mater.* **2007**, *19*, 2736-2751.

(102)   Stelzig, S. H.; Klapper, M.; Müllen, K. *Adv. Mater.* **2008**, *20*, 929-932.

(103)   Saito, R. *J. Polym. Sci. A* **2006**, *44*, 5174-5181.

(104)   Du, J.; Chen, Y. *Angew. Chem.* **2004**, *116*, 5194-5197.

(105)   Liu, Y.; Zheng, S. *J. Polym. Sci. A* **2006**, *44*, 1168-1181.

(106)   Alauzun, J.; Besson, E.; Mehdi, A.; Reyé, C.; Corriu, R. J. P. *Chem. Mater.* **2008**, *20*, 503-513.

(107)   Zhou, J.; Wang, L.; Dong, X.; Yang, Q.; Wang, J.; Yu, H.; Chen, X. *Europ. Poly. J.* **2007**, *43*, 1736-1743.

(108)   Watanabe, M.; Tamai, T. *J. Polym. Sci. A* **2006**, *44*, 4736-4742.

(109)   Neouze, M.-A.; Malenovska, M.; Schubert, U.; Kotlyar, V.; Kuperschmidt, E.; Peled, A.; Lellouche, J.-P. *J. Mater. Chem.* **2008**, *18*, 121-125.

(110)   Yuan, J.; Xu, Y.; Walther, A.; Bolisetty, S.; Schumacher, M.; Schmalz, H.; Ballauff, M.; Müller, A. H. E. *Nat. Mater.* **2008**, *7*, 718-722

(111)   Ogoshi, T.; Chujo, Y. *Macromolecules* **2005**, *38*, 9110-9116.

(112)   Mori, H.; Müller, A. H. E.; Klee, J. E. *J. Am. Chem. Soc.* **2003**, *125*, 3712-3713.

(113) Mori, H.; Lanzendörfer, M. G.; Müller, A. H. E.; Klee, J. E. *Langmuir* **2004**, *20*, 1934-1944.

(114) Lu, S.; Hamerton, I. *Prog. Polym. Sci.* **2002**, *27*, 1661-1712.

(115) Yang, J.; Lee, C.-H.; Ko, H.; Suh, J.-S.; Yoon, H.-G.; Lee, K.; Huh, Y.-M.; Haam, S. *Angew. Chem. Internat. Ed.* **2007**, *46*, 8836-8839.

(116) Balazs, A. C.; Emrick, T.; Russell, T. P. *Science* **2006**, *314*, 1107-1110.

(117) Mackay, M. E.; Tuteja, A.; Duxbury, P. M.; Hawker, C. J.; Horn, B. V.; Guan, Z.; Chen, G.; Krishnan, R. S. *Science* **2006**, *311*, 1740-1743.

(118) Cousinie, S.; Gressier, M.; Alphonse, P.; Menu, M.-M. *Chem. Mater.* **2007**, *19*, 6492-6503.

(119) Wei, Q.; Ji, J.; Shen, J. *Macromol. Rap. Commun.* **2008**, *29*, 645-650.

(120) Djalali, R.; Li, S. Y.; Schmidt, M. *Macromolecules* **2002**, *35*, 4282-4288.

(121) Kickelbick, G. *Hybrid Materials. Synthesis, Characterization and Applications*; Wiley-VCH: Weinheim, 2007.

(122) Mori, H.; Lanzendörfer, M. G.; Müller, A. H. E.; Klee, J. E. *Macromolecules* **2004**, *37*, 5228-5238.

(123) Retsch, M.; Walther, A.; Loos, K.; Müller, A. H. E. *Langmuir* **2008**, *24*, 9421-9429.

(124) Tsuchida, E.; Abe, K. *Adv. Polym. Sci.* **1982**, *45*, 1.

(125) Kabanov, V. A.; Papisov, I. M. *Vysokomol. Soed., A* **1979**, *21*, 243.

(126) Smid, J.; Fish, D. *Encyclopedia of Polymer Science and Engineering*; Wiley: New York, 1988; Vol. 11.

(127) Philipp, B.; Dautzenberg, H.; Linow, K.-J.; Koetz, J.; Dawydoff, W. *Prog. Polym. Sci.* **1989**, *14*, 91.

(128) Kabanov, V. A.; editors, I. *Macromolecular Complexes in Chemistry and Biology*; Springer: Berlin Heidelberg, 1994.

(129) Harada, A.; Kataoka, K. *J. Macromol. Sci., Part A: Pure Appl. Chem.* **1997**, *A34*, 2119-2133.

(130) Harada, A.; Kataoka, K. *Macromolecules* **1998**, *31*, 288-294.

(131) Harada, A.; Kataoka, K. *J. Am. Chem. Soc.* **1999**, *121*, 9241-9242.

(132) Harada, A.; Kataoka, K. *Science* **1999**, 65-67.

(133) Harada, A.; Kataoka, K. *Macromolecules* **1995**, *28*, 5294-5299.

(134) Kabanov, A. V.; Kabanov, V. A. *Bioconjugate Chem.* **1995**, *6*, 7-20.

(135) Kabanov, A. V.; Vinogradov, S. V.; Suzdaltseva, Y. G.; Alakhov, V. Y. *Bioconjugate Chem.* **1995**, *6*, 639-643.

(136) Lindhoud, S.; Vries, R. d.; Norde, W.; Stuart, M. A. C. *Biomacromolecules* **2007**, *8*, 2219-2227.

(137) Hofs, B.; Keizer, A. d.; Burgh, S. v. d.; Leermakers, F. A. M.; Stuart, M. A. C.; Millard, P.-E.; Müller, A. H. E. *Soft Matter* **2008**, *4*, 1473-1482.

(138) Plamper, F. A.; Becker, H.; Lanzendörfer, M.; Patel, M.; Wittemann, A.; Ballauff, M.; Müller, A. H. E. *Macromol. Chem. Phys.* **2005**, *206*, 1813-1825.

(139) Muthukrishnan, S.; Plamper, F.; Mori, H.; Müller, A. H. E. *Macromolecules* **2005**, *38*, 10631-10642.

(140) Kwon, J. Y.; Jang, Y. J.; Lee, Y. J.; Kim, K. M.; Seo, M. S.; Nam, W.; Yoon, J. *J. Am. Chem. Soc.* **2005**, *127*, 10107-10111.

(141) Burkhardt, M. PhD thesis, University of Bayreuth, 2007.

(142) Kratochvil, P. *Classical Light Scattering From Polymer Solutions*; Elsevier: Amsterdam, 1987; Vol. 5.

(143) Berry, G. C. *The Journal of Chemical Physics* **1966**, *44*, 4550-4564.

(144) Berne, B. J.; Pecora, R. *Dynamic Light Scattering*; John Wiley & Sons: New York, 1976.

(145) Schmitz, K. S. *An Introduction to Dynamic Light Scattering by Macromolecules*; Academic Press, Inc.: San Diego, 1990.

(146) Brown, W. *Light Scattering - Principles and Developement*; Calendron Press: Oxford, 1996.

(147) Siegert, A. J. F. *MIT Rad. Lab. Report* **1943**, *465*.

(148) Burchard, W.; Richterling, W. *Prog. Colloid Polym. Sci.* **1989**, *80*, 151-163.

(149) Provencher, S. W. *Computer Physics Communications* **1982**, *27*, 229-242.

(150) Lindner, P.; Zemb, T. *Neutrons, X-rays and Light: Scattering Methods Applied to Soft Condensed Matter*; Elsevier: Amsterdam, 2002.

(151) Higgins, J. S.; Benoit, H. C. *Polymers and Neutron Scattering*; Clarendon Press: Oxford, 1996.

(152) Chen, S. H. *Ann. Rev. Phys. Chem.* **1986**, *37*, 351.

(153) ILL http://www.ill.eu/YellowBook/D11/, 2006-10-20.

(154) Dewhurst, C. http://www.ill.eu/sites/grasp/grasp_main.html, 2006.

(155) Kohlbrecher, J. http://kur.web.psi.ch/sans1/SANSSoft/sasfit.html, 2008.

(156) Daoud, M.; Cotton, J. P. *Journal de Physique* **1982**, *43*, 531.

(157) Wijmans, C. M.; Zhulina., E. B. *Macromolecules* **1993**, *26*, 1214–7224.

(158) Pedersen, J. S. *J. Appl. Cryst.* **2000**, *33*, 637-640.

(159)   Pedersen, J. S.; Svaneborg, C. *Curr. Opinion Coll. Interface Sci.* **2002**, *7*, 158-166.

(160)   Muller, F.; Delsanti, M.; Auvray, L.; Yang, J.; Chen, Y. J.; Mays, J. W.; Demé, B.; Tirrell, M.; Guenoun, P. *Eur. Phys. J. E 3* **2000**, 45-53.

(161)   Förster, S.; Hermsdorf, N.; Böttcher, C.; Lindner, P. *Macromolecules* **2002**, *35*, 4096-4105.

(162)   Benoit, H.; Grubisic, Z.; Rempp, P.; Decker, D.; Zilliox, J. G. *Macromolecules* **1966**, *63*, 1507.

(163)   MicroCal *ITC Data Analyis in Origin - Tutorial Guide*, 1998.

(164)   Wiseman, T.; Williston, S.; Brandts, J. F.; Lin, L.-N. *Analytical Biochemistry* **1989**, *179*, 131-137.

(165)   Rasband, W. S., ImageJ, U. S. National Institutes of Health, Bethesda, Maryland, USA, http://rsb.info.nih.gov/ij/, 1997-2008.

(166)   Hesse, M.; Meier, H.; Zeeh, B. *Spektroskopische Methoden in der Organischen Chemie*; 4. ed.; Georg Thieme Verlag: Stuttgart, 1991.

(167)   *Organikum*; 21. ed.; Wiley-VCH: Weinheim, 2001.

(168)   Schumacher, M.; Ruppel, M.; Yuan, J.; Schmalz, H.; Colombani, O.; Drechsler, M.; Müller, A. H. E. *Langmuir* **2009**, *25*, 3407-3417.

6 Summary

The formation and characterization of smart organic-inorganic nanohybrids was studied. The inorganic part was formed by *N,N*-di(2,3-dihydroxypropyl)3-aminopropylfunctional silsesquioxane nanoparticles being highly functionalized with ca. 14 tertiary amino groups per particles, each amino group bearing four hydroxyl groups. Two different polymer systems were used for the organic side: amphiphilic block copolymer micelles of poly(*n*-butyl acrylate)-*block*-poly(acrylic acid) (PnBA$_x$-*b*-PAA$_y$ with x = 90, 100 and y = 100, 150, 300) and star-shaped poly(acrylic acid)s (PAA$_{100}$)$_{21}$ and (PAA$_{200}$)$_{24}$, the latter serving as a model system for frozen micelles. In all cases the mixing of aqueous solutions of anionic block copolymer micelles or the anionic stars with solutions of the silsesquioxane nanoparticles led to the easy and straightforward formation of organic-inorganic nanohybrids. The structure of the complex nanohybrids depends on pH and salinity. The amount of incorporated silsesquioxane nanoparticles within the micelles or the stars under varying external stimuli was determined using a large number of methods.

Complexation preserved the original size of the micelles - consisting of a PnBA core and a PAA corona - according to dynamic light scattering (DLS) and static light scattering (SLS) as well as light scattering titration measurements and asymmetric flow field-flow fractionation (AFFFF) experiments. Fourier-transform infrared spectroscopy (FT-IR) and dialysis measurements with fluorescently labelled silsesquioxane nanoparticles confirmed the nanohybrid formation over a relatively wide range in pH. Cryogenic transmission electron microscopy (cryo-TEM) micrographs indicated a core-shell structure of the nanohybrids with gradual decreasing density of silsesquioxane nanoparticles.

LS titrations gave an insight in the postulated interaction mechanism. Complexation in acidic media is driven by hydrogen-bonding and ionic interaction; in alkaline media nanohybrids are mainly formed due to ionic interaction. Depending on ionic strength, attractive Coulomb interactions may be (i) either sufficient to promote complexation even at high pH, where hydrogen-bonding is absent (low ionic strength), or are (ii) screened (high ionic strength), resulting in less favourable interactions between micelles and silsesquioxane nanoparticles. The reason for the size conservation is most probably due to the kinetically frozen micellar core and the compensation of (i) increased steric repulsion due to complexation and (ii) attractive interactions between the silsesquioxane nanoparticle and the charged PAA. The maximum of the interaction at 0.1 M could be deduced to be in the range 3.5 < pH < 7.5 NaCl. At low salinity (0.01 M NaCl) more nanoparticles were incorporated within the micelles. Nano-

hybrids exist even up to very basic conditions (pH < 9.5). The responsiveness of the system on pH and salinity as external stimuli was demonstrated by LS titration, dialysis and FT-IR measurements, thermogravimetric analysis (TGA) and AFFFF measurements.

Quantifying the amount of nanoparticles incorporated in the micelles turns out to be a arduous task. SLS of dialysed and undialysed samples and AFFFF of undialysed samples clearly showed increased molecular weights of the formed nanohybrids. TGA - requiring an exhaustive dialysis procedure prior to the measurements - provided information about the amount of incorporated silsesquioxane nanoparticles within the micelles. Isothermal titration calorimetry (ITC) provided the possibility to investigate the complexation mechanism in greater detail. Small angle neutron scattering (SANS) experiments, conducted at basic conditions, provided information on the inner structure of the nanohybrids. A newly developed fitting model enabled the quantification of the amount of interacting nanoparticles under these conditions.

All methods to determine the amount of nanoparticles incorporated within the micelles sustained the formation of the organic-inorganic nanohybrids. The absolute number of nanoparticles per micelle is quite high (in the range from 160 to 4300, depending on the used method and conditions), however, the calculated numbers of nanoparticles per acrylic acid unit are quite low (in the range from 0.002 to 0.053).

The PAA stars $(PAA_{100})_{21}$ and $(PAA_{200})_{24}$ showed behaviour comparable to that of the micelles. According to DLS and SANS experiments their size was preserved during complexation. SANS and LS titration measurements demonstrated the increased mass of the nanohybrid stars compared to the net stars. Cryo-TEM micrographs confirmed the formation of organic-inorganic nanohybrid stars, indicating a morphology with gradually decreasing density of nanoparticles. An appropriate fitting model for the SANS data for this challenging system was developed that proved the interaction between the silsesquioxane nanoparticles and the PAA and enabled the calculation of the amount of entrapped silsesquioxane nanoparticles within one star. The determined values were comparable to the ones calculated for the micellar nanohybrids.

Zusammenfassung

Es wurde die Bildung und Charakterisierung von intelligenten organischen-anorganischen Nanohybriden untersucht. Der anorganische Teil wurde von einem *N,N*-di(2,3-dihydroxypropyl)3-aminopropylfunctionalisiertem Silsesquioxan-Nanopartikel gebildet, das mit ca. 14 tertiären Aminogruppen pro Partikel hoch funktionalisiert ist und bei dem jede Aminogruppe vier Hydroxylgruppen trägt. Zwei unterschiedliche Polymersysteme wurden für die organische Seite benutzt: amphiphile Blockcopolymer-Mizellen aus Poly(*n*-butylacrylat)-*block*-Polyacrylsäure (PnBA$_x$-*b*-PAA$_y$ mit x = 90, 100 und y = 100, 150, 300) und die Polyacrylsäure (PAA)-Sterne (PAA$_{100}$)$_{21}$ und (PAA$_{200}$)$_{24}$, wobei die Letzteren als Modell für gefrorene Mizellen dienen. In allen Fällen führte das Mischen von wässrigen Lösungen der anionischen Blockcopolymer-Mizellen oder der anionischen Sternlösungen und der Silsesquioxan-Nanopartikel zur einfachen und direkten Bildung von organisch-anorganischen Nanohybriden. Die Struktur der komplexierten Nanohybride hängt vom pH-Wert und Salzgehalt der Lösung ab. Der Anteils der in die Mizellen oder die entsprechenden Sterne eingebauten Silsesquioxan-Nanopartikel unter variierender, externer Beeinflussung wurde mit zahlreichen Methoden quantifiziert.

Experimente mit dynamischer Lichtstreuung (DLS) und statischer Lichtstreuung (SLS) wie auch Lichtstreutitrationen und asymmetrische Fluss-Feldfluss-Fraktionierung (AFFFF) konnten bestätigen, dass bei der Komplexierung die Orginalgröße der Mizellen - aufgebaut aus einem PnBA-Kern und einer PAA-Schale - bewahrt wird. Fourier-transform Infrarotspektroskopie (FT-IR) und Dialysemessungen mit fluoreszenzmarkierten Silsesquioxan-Nanopartikeln bestätigten die Bildung der Nanohybride über einen relativ weiten pH-Bereich. Kryogene Transmissionselektronmikroskopie (cryo-TEM)-Bilder deuten auf eine Kern-Schale-Struktur der Nanohybride hin mit graduell abnehmender Dichte der Silsesquioxan Nanopartikel.

LS-Titrationen gaben einen Einblick in den vorgeschlagenen Wechselwirkungsmechanismus. Komplexierung im Sauren erfolgt aufgrund von Wasserstoffbrückenbindungen und ionischen Wechselwirkungen, im basischen Medium werden die Nanohybride hauptsächlich durch ionische Wechselwirkungen gebildet. Je nach Ionenstärke können (i) anziehende Coulomb-Wechselwirkungen entweder ausreichend sein, um Komplexierung auch bei hohem pH zu ermöglichen, wo keine Wasserstoffbrückenbindungen vorliegen (niedrige Ionenstärke) oder (ii) sie sind abgeschirmt (hohe Ionenstärke), wodurch sich weniger bevorzugte Wechselwirkungen zwischen Mizellen und Silsesquioxan-Nanopartikel ergeben. Der Grund für die

Beibehaltung der Größe ist höchstwahrscheinlich auf den kinetisch gefrorenen Mizellkern und die Kompensierung von (i) ansteigender, sterischer Abstoßung aufgrund von Komplexierung und (ii) anziehenden Wechselwirkungen zwischen den Silsesquioxan-Nanopartikeln und der geladenen PAA zurückzuführen. Die maximale Wechselwirkung konnte bei 0.1 M NaCl im pH-Bereich von 3.5 bis 7.5 gefunden werden. Bei niedriger Salzkonzentration (0.01 M NaCl) werden mehr Nanopartikel in die Mizellen eingebaut. Weiterhin konnte gezeigt werden, dass sogar unter basischen Bedingungen (pH < 9.5) Nanohybride existieren. Die pH- und Salzempfindlichkeit des Systems als externer Stimulus wurde mit LS-Titrationen, Dialyse und FT-IR Messungen, thermogravimetrischen Analysen (TGA) und auch AFFFF-Messungen belegt.

Die Quantifizierung des in den Mizellen eingebauten Teils der Nanopartikel stellte sich als mühsame Aufgabe heraus. SLS der dialysierten und undialysierten Proben sowie AFFFF der undialysierten Proben zeigten klar erhöhte Molekulargewichte der gebildeten Nanohybride. TGA benötigte einen langwierigen Dialyseprozess vor den Messungen und lieferte Informationen über den Anteil an in den Mizellen eingebauten Nanopartikeln. Isotherme Titrationskalorimetrie (ITC) lieferte die Möglichkeit den Komplexierungsmechanismus detaillierter zu untersuchen. Neutronenkleinwinkelstreumessungen (SANS) wurden im Basischen durchgeführt und stellten Informationen über die innere Struktur der Nanohybride bereit. Ein neu entwickeltes Fit-Modell erlaubte die Quantifizierung des wechselwirkenden Anteils an Nanopartikeln unter diesen Bedingungen.

Alle unterschiedlichen benutzen Methoden zur Quantifizierung der in die Mizellen eingebauten Nanopartikel belegen die Bildung der organisch-anorganischen Nanohybride. Die absolute Anzahl der wechselwirkenden Nanopartikel pro Mizelle ist recht hoch (im Bereich von 160 bis 4300, abhängig von der benutzten Methode und Versuchsbedingungen), aber die berechnete Anzahl von Nanopartikeln pro Acrylsäureeinheit ergibt niedrige Werte im Bereich von 0.002 bis 0.053.

Die PAA-Sterne $(PAA_{100})_{21}$ und $(PAA_{200})_{24}$ zeigten ein vergleichbares Verhalten wie die sternförmigen Mizellen. Aufgrund der Ergebnisse von DLS- und SANS-Experimenten bleibt ihre Größe während der Komplexierung konstant. SANS- und LS-Titrationsmessungen zeigten die erhöhte Masse der Nanohybridsterne im Vergleich zu den puren Sternen. Cryo-TEM Aufnahmen bestätigen die Bildung der organisch-anorganischen Nanohybridsterne und weisen auf eine Morphologie mit graduell abnehmender Dichte der Nanopartikel hin. Ein adäquates Fitmodel für die SANS Daten wurde für dieses anspruchsvolle System entwickelt und zeigte die Wechselwirkung zwischen den Silsesquioxan Nanopartikeln und der PAA. Es ermöglichte die Berechnung des Anteils an in einem Stern eingebauten Silsesquioxan Nanopar-

tikeln. Die bestimmten Werte waren vergleichbar mit den für die mizellaren Nanohybride berechneten Werten.

7   List of Publications

Colombani, O.; Ruppel, M.; Burkhardt, M.; Drechsler, M.; Schumacher, M.; Gradzielski, M.; Schweins, R.; Müller, A. H. E. **Structure of Micelles of Poly(*n*-butyl acrylate)-*block*-poly(acrylic acid)**, *Macromolecules* **2007**, *40*, 4351-4362.

Schumacher, M.; Ruppel, M.; Burkhardt, M.; Drechsler, M.; Colombani, O.; Schweins, R.; Müller, A. H. E. **Novel class of organic-inorganic nanohybrids from functionalized silsesquioxane-based nanoparticles and micelles of poly(n-butyl acrylate)-block-poly(acrylic acid)**, *Polym. Mater. Sci. Eng.* **2007**, *96*, 374-375.

Yuan, J.; Xu, Y.; Schumacher, M.; Schmalz, H.; Müller, A. H. E. **Core-Shell Cylindrical Polymer Brushes with Silica Nanowire Core**, *Polym. Prepr. (Am. Chem. Soc., Div. Polym. Chem.)* **2008**, *49*, 21-22.

Yuan, J.; Xu, Y.; Walther, A.; Bolisetty, S.; Schumacher, M.; Schmalz, H.; Ballauff, M.; Müller, A. H. E. **Water-soluble organo-silica hybrid nanowires**, *Nat. Mater.* **2008**, *7*, 718-722.

Schumacher, M.; Ruppel, M.; Yuan, J.; Schmalz, H.; Colombani, O.; Drechsler, M.; Müller, A. H. E. **Smart organic-inorganic nanohybrids based on amphiphilic block copolymer micelles and functional silsesquioxane nanoparticles**, *Langmuir* **2009**, *25(6)*, 3409-3417.

Schumacher, M.; Ruppel, M.; Kohlbrecher, J.; Burkhardt, M.; Plamper, F.; Drechsler, M.; Schweins, R.; Müller, A. H. E. **Smart organic-inorganic nanohybrid stars based on star-shaped poly(acrylic acid) and functional silsesquioxane nanoparticles**, *Polymer* **2009**, *50*, 1908-1917.

Acknowledgement

Erklärung

Ich bestätige hiermit, dass ich die Arbeit selbstständig verfasst und keine anderen, als die von mir angegebenen Quellen und Hilfsmittel benutzt habe.

Zudem bestätige ich hiermit, dass ich nicht anderweitig mit oder ohne Erfolg versucht habe, eine Dissertation einzureichen oder mich einer Doktorprüfung zu unterziehen.

Bayreuth, den 25. November 2008

_____
Manuela Schumacher